Title
Monitoring underground gas storage in a fractured reservoir using time lapse vsp

Author
Daley, Thomas M.

Publication Date
2000-03-15

LBNL-44876

ERNEST ORLANDO LAWRENCE BERKELEY NATIONAL LABORATORY

Monitoring Underground Gas Storage in a Fractured Reservoir Using Time Lapse VSP

Thomas M. Daley, Mark A. Feighner, and Ernest L. Majer

Earth Sciences Division

March 2000

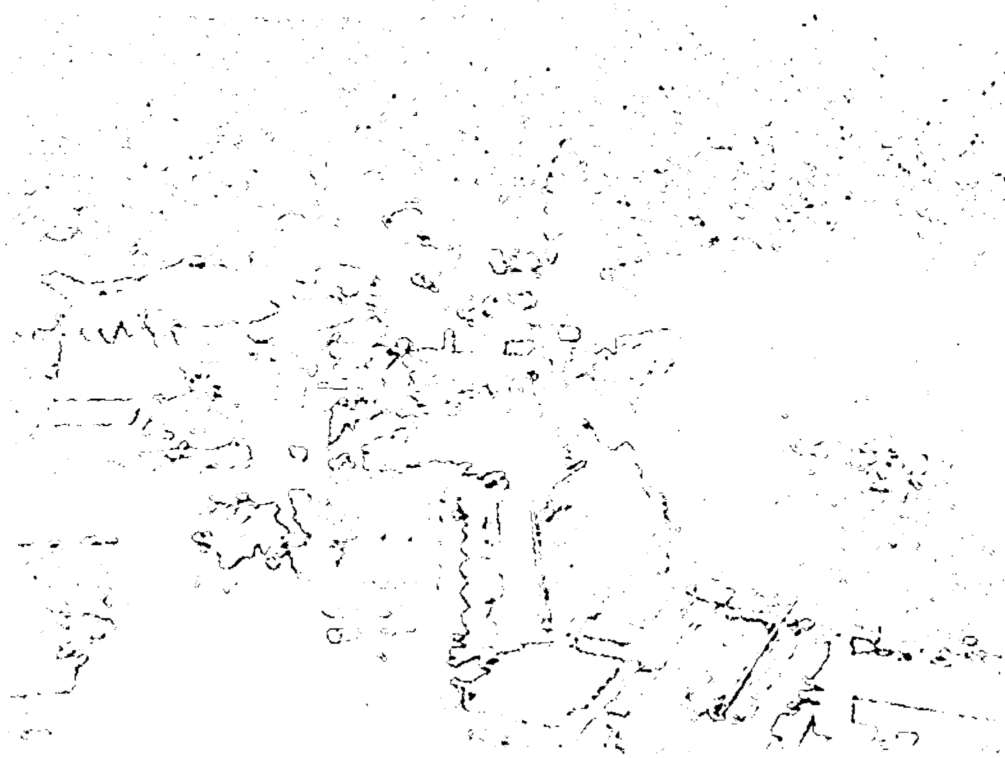

DISCLAIMER

LBNL-44876

Monitoring Underground Gas Storage in a Fractured Reservoir Using Time Lapse VSP

Thomas M. Daley,[1] Mark A. Feighner,[2] and Ernest L. Majer[1]

[1]Earth Sciences Division
Ernest Orlando Lawrence Berkeley National Laboratory
University of California
Berkeley, California 94720

[2]Department of Mathematics and Sciences
Solano Community College
Suisun, California 94585

March 2000

This work was supported by the Assistant Secretary for Fossil Energy, Federal Energy Technology Center (FETC). Processing was performed at the Center for Computational Seismology, which is supported by the Director, Office of Science, Office of Basic Energy Sciences, Division of Engineering and Geosciences, of the U.S. Department of Energy under Contract No. DE-AC03-76SF00098.

Abstract. This paper reports on time lapse VSP study in a naturally fractured reservoir used for underground gas storage. Four 9-component VSPs were acquired along with a walkaway and then repeated after the reservoir properties changed. The initial survey was conducted with the reservoir mostly gas saturated and the follow-up survey was conducted with the reservoir mostly water saturated. The near-offset 9-c VSP was investigated for indications of shear-wave splitting. No clear evidence of S-wave splitting or other anisotropic wave propagation could be attributed to the reservoir horizon. Ray trace modeling was performed using the VSP velocity results which showed that very little horizontal propagation was within the reservoir for the offset VSP sites. Because of the ray-path limitations, the offset VSP site data could not constrain time-lapse changes to the reservoir horizon. The P-wave walkaway did show a small time-lapse change within the reservoir horizon. This time-lapse change in velocity was interpreted in terms of a crack based equivalent media model to give a trade-off curve between crack density and saturation. A porous media approach was used to estimate porosity which shows time-lapse changes. Other analysis of the VSP including reflectivity and frequency vs. time analysis showed no clear time-lapse changes (plots in Appendix D). Surface seismic data near the VSP well was analyzed and modeled and we conclude that AVO analysis is not applicable to this site.

1. Introduction

The Northern Indiana Public Service Company (NIPSCO) operates naturally fractured reservoirs for seasonal storage of natural gas. The gas is injected during summer and withdrawn during winter. As part of DOE sponsored research in fractured gas production, Lawrence Berkeley National Laboratory (LBNL) designed a VSP (Vertical Seismic Profile) experiment to aid delineation of NIPSCO's dolomitic Trenton Formation reservoir, and to study the seismic effects of variable gas pressures. The reservoir is in NIPSCO's Royal Center field in Northern Indiana.

The effects of fracturing on seismic wave propagation have been widely studied (O'Connell and Budiansky, 1974 Crampin, et al., 1986, Schoenberg and Sayers, 1995, Pyrak-Nolte, et al., 1990) with one of the more significant effects being shear-wave splitting (also called shear-wave birefringence). Nine-component VSP's (3 component sources and 3 component receivers) provide an excellent method of measuring shear-wave splitting (Majer, et al., 1988 , Daley, et al., 1988, Daley and McEvilly, 1990, Winterstein and Meadows, 1991).

2. Background

The Royal Center field has limited geophysical characterization, with few well logs and only field wide monitoring of gas injection/withdrawal volumes. However, the annual displacement of water by gas within the natural fractures of the reservoir made this field a good candidate for time-lapse monitoring. There has been no hydrofracing or other intentionally induced fracturing of the reservoir.

The Trenton formation is a paleozoic ordovician dolomite which is part of the mostly shale and limestone stratigraphy of the Royal Center field (Figure 1). It is believed by the field operators that the top section of the Trenton dolomite is unfractured and forms a cap for the reservoir. The thickness of the cap section (as well as its fracture content) was assumed variable and was not well defined by the field operators. Only the distribution of wells indicated a potential dominant fracture orientation of NW-SE along the axis of an proposed anticline (see Figure E-1 in Appendix E). The dip within the Royal Center Field is only 1% - 2%.

As part of a fractured gas research program run by DOE's Federal Energy Technology Center (FETC), we designed a VSP survey which would take advantage of the reservoir's time-lapse changes to delineate spatial variations in reservoir properties as well as providing basic information for other seismic imaging proposed at Royal Center. Among the poorly defined properties of the reservoir are thickness of fracture interval, extent of fracturing above the reservoir (possible leakage), spatial distribution of fractures, and dominant orientation of reservoir fractures. We hoped to use multiple offset 9-component VSP's to monitor shear-wave splitting (and other seismic properties) at a productive storage well (implying multiple connected fractures) and at a poor storage well (implying no fracturing of poorly connected fractures). From available well sites, wells 157 (good storage) and 46 (no storage) were selected. The two major goals of this project, shown in schematic form in Figure 2, were to measure the reservoir fracture orientation from S-wave splitting and to estimate the fracture density distribution from spatial distribution of time-lapse changes in seismic travel times. A proposed optimal survey design included source locations as shown in Figure 3, however field site restrictions (including land and road access limitations) led to a less optimal distribution of source location as described in the data acquisition section below (Figure 4).

There were two phases of the time-lapse VSP data acquisition at the NIPSCO Royal Center field site. These two VSP surveys acquired data from essentially identical acquisition geometry (source/receiver locations) under distinctly different reservoir conditions. During the initial survey in December 1996 the reservoir gas pressure was near its maximum of about 400 psi; during the second survey in May 1997 the reservoir gas pressure was reduced to about 250 psi. Since the natural water pressure within the

Trenton formation is about 310 psi, the reservoir was mostly gas saturated in 12/96 and mostly water saturated in 5/97.

3. Data Acquisition

The initial data acquisition for the NIPSCO VSP experiment took place during Dec 1996. The sensors were 3-component wall-locking geophones in a 5 level string with 8 foot spacing between recording depths. Downhole digitization was used to enable multi-level recording on a 7-conductor wireline and to reduce ambient electrical noise in the data. Because the 157 well was presurized, a lubricator assembly long enough to contain the entire string was assembled on site and used for the duration of the survey (Figure 5). The source were vibroseis trucks, one Fayling P-wave truck and 2 Mertz S-wave trucks. The vibroseis sources (both P- and S-wave) used a 12 to 99 Hz sweep, 12 s long with a 3 second listen time. The sample rate was 1 ms. Each VSP data set has over 600 Mbytes of data, with about 10,000 seismograms. The S-wave trucks were positioned at each source site such that they generated an in-line and a cross-line polarized shear-wave (relative to the line connecting the source location and the well). Source site access was a problem because we could not obtain county permission to use the paved roads for source points and we could not use farm land at the well 46 site. Farm land surrounding the 157 well was made available by the land owners, however the soil proved too unconsolidated to support the 40,000+ pound vibroseis trucks. We were left to locate our source sites on dirt roads, which are in a strict North-South/East-West grid. The available roads determined the source locations used in the survey. The following VSP data was therefore acquired at Royal Center field in Dec. 1996 (where S1 is an S-wave polarized parallel to the line connecting source and well and S2 is an S-wave source polarized tangential to the line connecting source and well):

Well 46

- Run 1: 970 ft. to 578 ft. at 8ft. intervals, P, S1 and S2 sources at zero offset (well pad)

Well 157

- Run 1 : 1088 ft. to 296 ft. at 8 ft. sensor intervals for P, S1 and S2 sources at well pad (site 1), and P2 source at site 2.
- Run 2 : 1088 ft. to 696 ft. at 8 ft. sensor intervals for P source at site 7, and S1 and S2 sources at site 2.
- Run 3 : 1088 ft. to 696 ft. at 8 ft. sensor intervals for P, S1 and S2 sources at site 3.
- Run 4 : 1088 ft. to 696 ft. at 8 ft. sensor intervals for P, S1 and S2 sources at site 4.
- Run 5: 1016 ft. to 984 ft. at 8 ft. sensor intervals for P and S2 sources on East walkaway at 50 ft. source intervals from about 200 ft. to 1550 ft.
- Run 6: 1088 ft. to 696 ft. at 8 ft. sensor intervals for P source at site 6 (2740 ft. offset).

Figure 4 shows a schematic location map of the source sites. The second phase VSP survey (May 1997) was identical except that

1) Well 46 was not used (because the lack of access permission away from the well pad eliminated our ability to perform spatial imaging and therefore compromised the survey),

2) Run 1 data (site 1) at well 157 was acquired up to 96 feet at 8 ft intervals to give better shallow velocity control,

3) Run 6 data at site 6 was acquired with both P and S-Wave sources because of better off-road access conditions.

3.1. Data Processing

The data processing was mainly performed using the FOCUS-3D seismic processing package produced by COGNI-SEIS (versions 4.0 and 4.1). The coordinate rotation and particle motion analysis was done using LBNL software.

The processing flow for each data set is as follows:

1) Convert data from field formatted data tapes.

2) Edit and stack uncorrelated traces (in May 1997, stacking was done in the field).

3) Correlate traces and sort by source type.

4) Use P-wave arrival to calculate 3 component geophone rotation angles.

5) Use the calculated rotation angles to rotate each source type data set into vertical, horizontal in-line, and horizontal cross-line geophone orientations.

6) For zero offset, use S-wave arrivals to measure s-wave splitting and calculate anisotropy axis of symmetry to estimate fracture orientation.

7) Pick arrival times, calculate P and S-wave velocities and Poisson's ratio.

The phase 1 well 46 data set had problems because of background noise and rotation analysis error from near vertical P-wave propagation (in-field restrictions discussed above prohibited using an offset P-wave source location). Without reliable orientation information, the shear-wave data could not be analyzed. The well 46 data set has not been analyzed beyond step 5, and was not repeated in phase 2 because of these problems.

The phase 1 well 157 data sets have fair to good data quality, limited by noise bursts in the well which required hand editing. These noise bursts were probably caused by gas release into the well. The phase 2 data sets appeared to have more noise bursts, probably because the reservoir was now mostly water saturated, allowing more gas bubbling. After performing extensive hand edits in the phase-1 processing, effort was spent on developing automated noise burst editing routines in the phase 2 data sets (Figure 6). By editing the noise bursts in the uncorrelated recordings, the impact on the correlated data was minimized. A 40 Hz, 60 dB/octave low pass filter was applied to the data before the zero-offset time picking. The rotation angle analysis was done using P-wave particle motion eigenvalue analysis (Daley, et al., 1988). The resulting edited, correlated, rotated seismograms are shown in Appendix A.

The calculation of anisotropy axis of symmetry was done with a 4-component orientation analysis (Alford, 1986 Thomsen, 1988). However, close inspection of field data has shown a source amplitude variation between the two S-wave vibroseis trucks which invalidates the assumptions of this analysis. Inspection of vibroseis baseplate accelerometers found a 25% amplitude difference between the two shear-wave vibroseis. However, correction for this difference still leaves a peak amplitude difference of a factor of 4 between the data from each shear-wave truck. Additionally, there is noticeable difference between the two shear-wave wavelets, despite wavelet analysis which was performed to chose a consistent vibroseis reference sweep for both s-wave sources (see Figures 7a-b). If the two shear-wave sources were not generating identical wavelets into the subsurface, this is another violation of the underlying assumptions of the 4-component anisotropy axis-of-symmetry orientation analysis. Therefor we are not using the results from this analysis of the axis of symmetry of anisotropy. The lack of significant S-wave splitting for the zero offset at well 157 (which is unaffected by the amplitude variations) indicates that the 4-component orientation analysis would have been inconclusive even if the S-wave amplitude variation was not present in the data because S-wave splitting is the attribute used for 4-component analysis. The s-wave splitting analysis, like the velocity analysis utilized travel time information obtained from the rotated data. Travel time picking was tested using cross-correlation of first arrival wavelets, and hand picking of peaks or zero crossings, with results in agreement for all methods. The results shown in Figures 8a-d and Appendix B are for picks of the maximum of the correlated wavelet.

4. Results

4.1. Site 1 - Vertical Propagation Results

Initial results from the Dec 1996 VSP indicated minimal shear-wave splitting effects and strong reflections (an example is shown in Figure 7a-d). Analysis of velocity structure obtained from the zero offset VSP showed large velocity variations in the Royal Center Field ranging from 9000 ft/s to nearly 20,000 ft/s in the Trenton Dolomite. A large velocity inversion was measured related to the low velocity Eden shale formation which overlies the high velocity Trenton dolomite. This velocity inversion has significant impact on the offset VSP raypaths and on our ability to measure properties within the reservoir which will be discussed below. With the 9-component VSP, P- and S-wave velocities and their ratio and Poisson's ratio can be calculated. These data plots are in Appendix B.

The May 1997 survey successfully repeated the Dec 1996 survey. The two time-lapse data sets have been analyzed for spatial or temporal variations in P- and S-wave travel time, shear-wave polarization, and shear-wave splitting. The phase 1 and phase 2 zero-offset data analysis both indicated essentially isotropic propagation. When we compared the measured travel times between phase 1 and phase 2, we found no change in S-wave or P-wave time within the 3-4 ms scatter of the data points and allowing for a static time shift which is attributable to near-surface conditions (Figure 8a-d). This means that the measured velocity from the zero offset VSP data set was not affected by the change in reservoir gas saturation. A comparison of shear-wave particle motion (Figure 9) indicates the polarizations stayed predominantly aligned with the sources (isotropic propagation), with some indication splitting which can not be attributed to the reservoir zone.

Our hypothesis for the apparent inability of the zero-offset survey to detect either fracture-induced anisotropy or velocity changes caused by variable gas pressure/saturation is that the zone of fracturing associated with the Trenton Formation reservoir around well 157 is too thin to be seen by the relatively long wavelengths of our VSP survey. With dominant frequency of 40 Hz and fast velocities of about 10,000 ft/s for S-waves, our S wavelength was about 250 ft The relatively thin reservoir (probably about 30 to 50 ft) was not "visible" to the waves propagating vertically through the

Trenton Formation. Additionally, the shallow velocity structure and available well depth appears to limit the ability of offset VSP geometry to sample a wide range of incident angles for the Trenton reservoir, thereby limiting the use of amplitude vs offset analysis.

However, there are small, 1 to 3 ms, time changes observed at depth (after allowing for the larger time changes due to the near surface material changes). The two most compelling examples are the P-wave walkaway data and the shear-wave data from sites 3 and 4.

Analysis focused on interpreting these small, 2-3 ms travel time changes seen at depth as time-lapse velocity changes confined to the reservoir (presumably due to varying gas pressure and saturation). Before analysis of the walkaway and offset data could begin, we needed to understand the propagation paths in the subsurface; this need led to development of ray traced models for the VSP.

4.2. Modeling

The effects of the subsurface velocities on wave propagation can be estimated by seismic modeling. We performed ray trace modeling, based on velocities measured by the zero-offset VSP in phase 1 (in Appendix B), to investigate the ability of the offset source locations to "see" more of the reservoir than the zero offset. Our initial modeling used the following velocity structure:

Layer Depth (ft)	P Velocity (ft/s)	S Velocity (ft/s)
0-300	6,100	2720
300-500	15,000	9200
550-670	13,000	6200
670-930	9,500	4800
930-1100	18,000	9500

Unfortunately, the results from this model indicated that the velocity structure at Royal Center significantly limits the propagation within the reservoir. More detailed modeling with subdivisions of each layer (Figure 10a-b) shows that only a small percentage of the offset VSP raypath is within the Trenton formation, and less is within the reservoir (using a high velocity, unfractured cap at the top of the Trenton overlying a lower velocity fractured reservoir). The highly variable velocity layers (9000 to 18000 ft/s P-wave velocities) with a strong velocity inversion constrains most of the wave propagation to shallow high velocity layers. The high velocity Silurian limestone bedrock above the slow velocity Maysville formation caused most of the energy to be propagated in the bedrock formation. Only a small percentage of the ray paths are in the Trenton formation reservoir zone (below approximately 950 to 1000 feet). We believe this effect is the limit on the ability of far offset VSP sites to detect spatial changes in reservoir properties.

4.3. Time Lapse Analysis

Given that the reservoir fractures were not directly detected with shear-wave anisotropy measurements, we looked to time lapse changes in reservoir properties to detect and estimate the extent of fractures. We believe that the displacement of gas by water within the fractures should cause changes in seismic velocity which can be modeled via theoretical relationships between fractures and seismic propagation such as equivalent media velocity variations or fracture stiffness variations. In both cases the presence of gas as a fracture filling should create lower velocities than the presence of water as a fracture filling material. Lower velocities will lead to increased travel times as measured by a VSP survey. As described above, the Dec 1996 (phase 1) survey had gas saturation in the reservoir, while the May 1997 (phase 2) survey had water saturated reservoir conditions with an associated decrease in reservoir pressure. Our basic tool for VSP time lapse analysis is travel time differencing. We expect little change in travel time above the reservoir (except for the near surface which has velocity changes caused by seasonal water saturation changes) and an increase in travel time difference at and below the reservoir. For each source site we have three independent measures of time lapse change in travel time; the P-wave, the in-line S-wave (S1), and the cross-line S-wave (S2). Appendix C has the plots of travel time change for these three sources for all source points. Additionally, the walkaway survey provides well sampled spatial measurement of the time lapse changes along one azimuth. As mentioned above, the time lapse data sets with the most compelling evidence for seismic velocity variations were the P-wave walkaway and the site 3 and 4 S-wave data.

4.4. Time-Lapse P-wave Walkaway Data

The P-wave walkaway data was analyzed by comparing the time lapse changes at the shallowest sensor (984 ft.) with the changes at the deepest sensor (1016 ft.). Without knowing the actual reservoir interval (production is over a large perforated casing interval), these sensors straddle the "best guess" of the reservoir available from field engineers (984 to 1016 feet). We hypothesize that the deeper sensor will record a larger time lapse change due to velocity changes within the reservoir induced by changing from gas to water saturation. Figure 11 shows there is a consistent 0.1 to 0.5 ms difference in the time lapse delay between the two walkaway sensor depths. The mean value for the 27 walkaway source locations is 0.2 ms with a standard deviation of 0.1 ms. The consistency of the time-lapse difference gives us confidence that this observation is caused by physical property changes within the reservoir zone. We are thus using a volumetric average over the reservoir region probed by the walkaway, rather than trying to delineate spatial variability in the reservoir, as was our original plan.

Knowing the time-lapse change in P-wave propagation time, we need to determine the actual propagation distance in the reservoir to determine the change in seismic velocity. The propagation distance is modeled in via raytracing described previously to determine the P-wave propagation distance (raylength) in the reservoir for the walkaway survey. The propagation distance is dependent on the depth chosen for the interface between Trenton cap rock (high velocity, presumably unfractured) and Trenton reservoir (lower velocity, fractured). Figure 10 shows raypaths in the reservoir horizon. The reservoir ray lengths were determined by differencing the lengths for top and bottom sensors. We found values for the differenced ray lengths in the reservoir ranging between 20 feet (near offsets) and 60 feet (far offsets). When the 0.2 ms time-lapse travel-time variation is attributed to these propagation distances, we calculate 5% to 15% velocity changes in the reservoir relative to the velocity measured in the near offset survey at site 1. Additionally, inspection of the interval velocities from site 1 finds the interval centered near the reservoir (1016') has a 10% velocity change, so we have confidence in using 10% as our estimate of velocity change in the Trenton reservoir due to changing gas saturation. With an estimate of time-lapse reservoir velocity change, we can estimate the material property variation necessary to cause the velocity change.

5. Estimates of Fracture Density and Saturation in the Reservoir

Without being able to resolve the anisotropic properties of the reservoir, we decided to estimate reservoir properties using an equivalent media description of fractures (O'Connell and Budiansky, 1974). This model is appropriate for our situation of long wavelengths (about 100 m) compared to fracture size (presumably 0.1 to 1 m) and isotropic wave propagation. In this model, the effect of thin randomly oriented ellipsoidal cracks with variable saturation on material properties is calculated as though there is a media having equivalent properties to the fractured solid. The crack density, ϵ, is defined by $\epsilon = (2N/\pi)(A^2/P)$, where N = cracks per unit volume, A is the area of a crack, and P is the perimeter. This relationship for a partially saturated cracked rock is given by

$$\epsilon = \frac{45}{16}\frac{(\nu - \bar{\nu})}{(1-\bar{\nu}^2)}\frac{(2-\bar{\nu})}{[(1-\xi)(1+3\nu)(2-\bar{\nu}) - 2(1-2\nu)]} \qquad (1)$$

where ϵ = the crack density,

ν = Poisson's ratio for the uncracked matrix,

$\bar{\nu}$ = Poisson's ratio for the cracked rock, and

ξ = saturated fraction of cracks.

In the NIPSCO data, we used

Vp = 15,700 ft/s and Vs = 9600 ft/s for gas saturated conditions, and

Vp = 17,200 and Vs = 9,700 ft/s for water saturated conditions.

These velocities come from the 72 ft interval velocity centered at 1016 ft. Poisson's ratio for an uncracked dolomite ($\nu = 0.33$) was taken from Carmichael, 1982.

For our analysis of the NIPSCO data, this analysis leads to a trade off between the crack density and the crack saturation (the fraction of cracks water saturated). Figure 12 shows the trade off curve of crack density and saturation for the Trenton reservoir calculated for the velocity variations seen in the walkaway survey. These two curves represent the changes in reservoir properties at well 157. For any given crack density, the difference between the two curves represents the percentage of fractures whose water is displaced by gas. For a reservoir with higher fracture density, fewer cracks need to be gas saturated to give the velocity changes observed in the VSP. If other information about crack density becomes available (for instance from core measurements) the curves in Figure 12 can be used. To provide a more physical interpretation of crack density, we can assume a circular fracture of 1 m^2 area. We then get the curves shown in Figure 13 which has fractures per unit volume instead of dimensionless crack density.

5.1. Equivalent Porosity Estimate

Because there is not strong evidence of fracture induced wave propagation effects within the reservoir for Site 1 data (near vertical propagation), we believed it would be instructive to use a matrix porosity model of the time-lapse changes observed in the walkaway VSP. We used an approximation to Gassmann's relations (Gassmann, 1951) proposed by Mavko, et al., 1998 for data with P-wave velocity (V_p). They use the modulus $M = \rho V_p$. For a system with two fluids saturating a matrix, we use:

M_o = matrix rock modulus,

M_{fl1} = fluid 1 modulus,

M_{fl2} = fluid 2 modulus,

M_{sat1} = modulus of rock saturated with fluid 1,

M_{sat2} = modulus of rock saturated with fluid 2.

For the case of two fluids displacing the same porosity, such as the gas displacing water in the Trenton reservoir, we can state the porosity ϕ as follows:

$$\phi = \frac{\frac{M_{fl1}}{(M_o - M_{fl1})} - \frac{M_{fl2}}{(M_o - M_{fl2})}}{\frac{M_{sat1}}{(M_o - M_{sat1})} - \frac{M_{sat2}}{(M_o - M_{sat2})}} \tag{2}$$

We use water for fluid 1 ($\rho = 1.0$, $V_p = 1531$ m/s), and methane gas for fluid 2 ($\rho = 0.34$, $V_p = 430$ m/s). Evaluation of this equation gives a porosity of 0.32.

It is interesting to note that evaluation of the crack density plots in Figure 12 for a differential saturated fraction of 32% gives a crack density of $\epsilon = 0.27$. However, this should not be considered a true estimate fracture density, because Gassmann's relations and the O'Connel and Budiansky relationships have different conceptual models of rocks and can not in theory be combined. It would be much preferable to maintain a crack based model of the reservoir and use other information to estimate the fracture density or the partial saturation change.

6. Offset Site Data - Possible Anisotropy

The site 3 and 4 S-wave data were analyzed by comparing the S1 and S2 source polarizations at each site. Since sites 3 and 4 are essentially 90 degrees apart in azimuth, the S1 and S2 sources have opposite azimuthal polarization at each site. That is, the S1 source at site 3 has the same azimuthal polarization as the S2 source at site 4, while the S2 source at site 3 has the same azimuthal polarization as the S1 source at site 4. We therefore expect reversed relative time lapse change when comparing S1 and S2 for sites 3 and 4, if the reservoir has an aligned fracture set which is not on a North-South or East-West azimuth. Figure 14 shows that we do observe such reversed time lapse changes, and both sites have approximately the same magnitude of change. For site 3, S2 (North/South polarized) data has about 1.5 ms more time lapse change. For site 4, S1 (North/South polarized) has about 1.5 ms more time lapse change. Since the North/South polarized source shows the largest change at both sites, we can propose a conceptual model of a reservoir with vertical fractures having a predominantly East/West azimuth. This is because shear waves polarized normal to the fracture strike azimuth will be slowed compared to shear waves polarized parallel to the fracture azimuth. Unfortunately, the data do not have a spatially constrained time-lapse change. We can not resolve a change in the reservoir zone (975 to 1025 ft.). The increasing time-lapse change seen below 850 ft. may be related to vertical fracturing extending above the reservoir, however this is not consistent with the vertical propagating waves at site 1.

7. Other Analysis

There is remaining analysis beyond the scope of this report which holds promise for fracture and gas detection using reflection and mode-conversion properties. In the phase 1 data we observed a strong reflection from the Trenton formation and a strong mode conversion (Figure 7). The mode conversion seems associated with the Maysville and Eden formation contact, while the S-wave reflection seems associated with the Trenton formation and may be affected by reservoir gas saturation. Initial investigation of zero-offset (site 1) P-wave reflectivity, using F-K separation of upgoing and downgoing energy, did not yield any clear time-lapse changes (see plots in Appendix D). Frequency vs time analysis of the walkaway P-wave also yielded no clear time-lapse changes (plots in Appendix D).

8. Surface Seismic Analysis

As part of the FETC fractured gas research program, LBNL was asked to study 2-D surface seismic data which had been interpreted using Trenton formation reflection amplitude anomalies as representative of gas saturation. We also thought it would be instructive to compare two crossing surface lines which intersect near the location of well 157. Figure E-1 shows the location of lines RC-1 and RC-5 along with many of the wells in the Royal Center field. The VSP well, S-157-T, is at the intersection of these two lines. Figure E-2 shows CDP gathers from these two lines in the vicinity of well 157. The Trenton formation reflection (top of Trenton) is at about 0.17 s time. Figure E-3 shows the CDP stacked sections from lines RC-1 and RC-5 with the VSP stacked upgoing reflections inserted in the middle. Again the Trenton reflection is at about 0.17 s. We see that the reflection wavelet for the VSP is quite different with earlier energy. The two surface lines are similar with RC-1 having reduced side lobes (red) compared to the main peak (blue). The bottom of Trenton reflection (0.2 s) is quite similar on both surface lines and the VSP, indicating little effect from the reservoir which presumably varies laterally away from the VSP well. Our reprocessing of these two seismic lines did not show the strong lateral variation in the Trenton reflection wavelet which had been interpreted as lateral variation in fracturing.

The possibility of using AVO techniques in the surface seismic was investigated, however the velocity structure is a strong limit on the actual incident angles which can be obtained. Figure E-4 shows modeling of the surface seismic cdp gathers for the top of Trenton reflection, and we can see that there is very limited angular coverage. Therefor we have concluded that the Trenton is not a good candidate for AVO studies.

9. Summary and Conclusions

Underground storage of natural gas with seasonal injection and withdrawal provides an excellent opportunity to study time-lapse changes in reservoir properties. In particular, the NIPSCO site is attractive because water displaces gas within the reservoir, thus maximizing the changes in material properties and elastic wave propagation. We designed and acquired a time-lapse VSP study aimed at characterizing the reservoir properties using the spatial and temporal variations in seismic wave propagation. Unfortunately, the study was initially compromised by surface access restrictions which limited the scope of data acquisition, and by questions about the amplitude equivalence of two shear-wave sources. Nonetheless, multiple 9-C VSPs were collected while the reservoir was gas saturated and repeated with the reservoir water saturated. The velocity structure of the Royal Center site included a strong velocity inversion which greatly limited the volume of the reservoir which could be probed with the VSP method. The near offset VSP (site 1) was analyzed for shear-wave splitting (under the assumption of vertical fracturing with a dominant orientation), but no definitive result could be obtained. This is partially due to problems with shear source amplitudes, but the travel time analysis also found no splitting within the reservoir horizon (and within the resolution of the data). We believe the reservoir is too thin for the wavelengths obtainable with the VSP method in this fast velocity material (dolomite). The far offset source sites did show some shear wave splitting, and a time-lapse change in velocity was observed in the P-wave walkaway. The P-wave walkaway data could be constrained to time-lapse change in velocity within the reservoir horizon. This result was analyzed in terms of fracture density and partial crack saturation using the long wavelength, equivalent media approach. Tradeoff curves between crack density and saturation were generated for the gas saturated and water saturated conditions. The difference between these two curves represents the percentage of the fracture space utilized for gas storage for a given fracture density.

Other studies included variation in near-offset P-wave reflections (no changes observed) and frequency vs time analysis of the walkaway data (no clear time-lapse change). We also conducted an analysis of surface seismic data acquired near the VSP well. We found no difference in the Trenton reservoir between north-south and east-west reflection lines. We also used our ray tracing model based on VSP velocities to study the CMP reflection gathers. We found that, like the offset VSP surveys, the CMP gathers had very little variation in angle of incidence of rays. This means the AVO analysis would not be useful for the Trenton reservoir. Again like the VSP surveys, the shallow velocity inversion with large contrasts is preventing lateral sampling of the Trenton at any reflection point.

In conclusion, the Trenton reservoir has good potential for assessing the effects of varying gas and water saturation. However, surface seismic sources will be limited in their ability to image the effects because of the velocity structure and the relative thinness of the reservoir. We believe that borehole source methods, such as crosswell or singlewell imaging, provide the best opportunity to study the seismic response by avoiding the shallow velocity inversions and providing higher frequency data.

10. Acknowledgements

This work was supported by the Assistant Secretary for Fossil Energy, Federal Energy Technology Center (FETC). Processing was performed at the Center for Computational Seismology, which is supported by the Director, Office of Science, Office of Basic Energy Sciences, Division of Engineering and Geosciences, of the U.S. Department of Energy under Contract No. DE-AC03-76SF00098. We would like to thank FETC project manager Thomas Mroz for his support, and Jim Crispman of NIPSCO for his help with field information and access. We would like to thank the LBNL field crews for both data acquisition sessions, especially Don Lippert, Cecil Hoffpaiur, Ken Williams, Jim Galvin and John Beck.

Figure 1. Geologic column for the Royal Center field. The approximate depths of major units at the VSP well 157 are: Glacial Till 0-150 ft., Silurian limestone and shale 150-675 ft., Eden shale 675 - 930 ft., Trenton dolomite 930 - 1100 ft.

Figure 2. Schematic objectives of NIPSCO VSP.

Figure 3. Original design concept for NIPSCO VSP.

Figure 4. Seismic source locations for NIPSCO VSP data acquisition. Field conditions and local access laws prevented locations as in original concept (Figure 2).

Figure 5. Sixty ft. lubricator pipe used to introduce multi-level sensor string in the presurized VSP well.

Figure 6. Uncorrelated vibroseis data showing effects of automatic noise burst editor before (left) and after (right) edits.

Figure 7a. Seismograms from orthogonal S-wave experiment at site 1. The left side data set is in-line horizontal oriented sensors recording an in-line oriented S-wave source over the depth range 296 ft. to 1088 ft. The right side data set is cross-line horizontal oriented sensors recording a cross-line oriented S-wave source over the same depth range. These data sets are used for estimating shear wave anisotropy which can be controlled by subsurface fracturing.

Figure 7b. Four orthogonal S-wave recordings for depths 936 to 1088 ft (the approximate reservoir zone). Top-left is in-line source and in-line sensor (XX), top-right is in-line source and cross-line sensor (XY), bottom-left is cross-line source and in-line sensor (YX), bottom-right is cross-line source and cross-line sensor (YY). The seismograms are normalized to the maximum of each source.

Figure 8a. Time lapse change in P-wave travel time for site 1. Times are 1996 data (gas saturated reservoir) minus the 1997 times (water saturated reservoir).

Figure 8b. S-wave splitting in terms of travel time difference (S1 (in-line, east-west) source minus S2 (cross-line, north-south) source for site 1 in 1996 (gas saturated reservoir).

Figure 8c. S-wave splitting in terms of travel time difference (S1 (in-line, east-west) source minus S2 (cross-line, north-south) source for site 1 in 1997 (water saturated reservoir).

Figure 8d. Time lapse change in S-wave travel time for site 1. Times are 1996 data (gas saturated reservoir) minus the 1997 times (water saturated reservoir) for S1 (in-line, east-west) source and S2 (cross-line, north-south) source.

Figure 9. Comparison of S-wave hodograms (particle motion) for in-line (east-west) source polarization (left) and cross-line (north-south) source polarization (right) for three depths within or below the reservoir. The S-wave polarization is dominantly isotropic with some ellipticity and a moderate east-west component on the cross-line (north-south) source data (right).

Figure 10a. Ray tracing for P-wave walkaway survey. Note that very little propagation occurs in the Trenton formation. Velocities are from the 1997 site 1 VSP modified to better match the walkaway travel times.

Figure 10b. Close-up view of raypaths within the reservoir zone of the Trenton. A conceptual model of an unfractured Trenton cap with minimal fracturing above a highly fractured Trenton reservoir was applied to estimate the raylengths within the reservoir. These raylengths were used in the fracture density and saturation estimates for the reservoir. The five sensor locations are the walkaway sensor depths.

Figure 11. Time lapse changes in P-wave travel time for top and bottom walkaway sensors. The sensors were not moved between each station recording. Times were picked on the unrotated vertical component. The station spacing was 50 ft. The difference between these two curves provides the estimate of time-lapse velocity changes between gas filled and water filled reservoir conditions using the raylengths estimated raytracing (Figure 10). The average difference for all stations between the 1016 and 984 ft sensors is 0.2 ms with a standard deviation of 0.1 ms.

Figure 12. Trade off curves for dimensionless crack density ϵ and saturation ϕ for the two VSP surveys. The difference between the curves for a given ϵ represents the partial saturation used for gas storage.

Figure 13. Trade off curves for volumetric crack density and saturation ϕ for the two VSP surveys using a 1 m^2 circular fracture. The difference between the curves for a given crack volume represents the partial saturation used for gas storage.

Figure 14. Time-lapse changes in S-wave travel time between 1996 (gas saturated reservoir) and 1997 (water saturated reservoir) VSP surveys. The north-south polarized S sources have larger time changes than the east-west polarized sources.

Appendix A: VSP Data Plots

Figure A1. Cross correlation of two Pelton generated sweeps showing 85 ms delay due to varying trigger time shift in 1996 data set.

Figure A2. Cross correlation of two data traces with a 100 ms time shift added to show full wavelet. 85 ms delay from figure A1 has been removed.

Figure A3a - A3c. Seismograms from Well 46, 1996. The three panels are geophone components horizontal in-line (left), horizontal cross-line (center), and vertical (right). The traces have been rotated (using P-wave particle motion) and are scaled using the maximum of all three panels. A3a is P-wave source, A3b is S-wave in-line source, A3c is S-wave cross-line source.

Figure A4a - A4d. Seismograms from Well 157, site 1, 1996 survey. The three panels are geophone components horizontal in-line (left), horizontal cross-line (center), and vertical (right). The traces have been rotated (using P-wave particle motion) and are scaled using the maximum of each trace. A3a is P-wave source at site 1, A3b is S-wave in-line source, A3c is S-wave cross-line. A4d is P-wave source at site 2 (used for rotation analysis of site 1 data).

Figure A5a - A5c. Seismograms from Well 157, site 2, 1996 survey. The three panels are geophone components horizontal in-line (left), horizontal cross-line (center), and vertical (right). The traces have been rotated (using P-wave particle motion) and are scaled using the maximum of each trace. 5a - A5c are the P-wave, S-wave in-line, and S-wave cross-line, respectively.

Figure A6. Seismograms from Well 157, site 3, 1996 survey. The three panels are geophone components horizontal in-line (left), horizontal cross-line (center), and vertical (right). The traces have been rotated (using P-wave particle motion). Left panels are S-wave cross-line source, right panels are S-wave cross-line (each scaled to maximum of three components).

Figure A7a - A7c. Seismograms from Well 157, site 4, 1996 survey. The three panels are geophone components horizontal in-line (left), horizontal cross-line (center), and vertical (right). The traces have been rotated (using P-wave particle motion) and are scaled using the maximum of each trace. A7a - A7c are the P-wave, S-wave in-line, and S-wave cross-line, respectively.

Figure A8a - A8f. Seismograms from Well 157, walkaway, 1996 survey. The 5 panels are geophone depths 984, 992, 1000, 1008 and 1016 ft. left to right. The 27 traces per panel are the 27 offset locations (50 ft. spacint). The traces are scaled to the maximum of each section except where noted. A8a-A8c are P-wave source, geophone components vertical (trace scaling), unrotated horizontal 1 (trace scaling), and unrotated horizontal 2. A8d-A8f are S-wave cross-line source, vertical, unrotated horizontal 1, and unrotated horizontal 2.

Figure A9. Seismograms from Well 157, site 6 P-wave source, 1996 survey. The three panels are horizontal in-line (left), horizontal cross-line (center) and vertical (right). The traces are normalized to their maximum.

Appendix B: Travel Time, Velocity and Rotation Angle Tables and Plots

Figure B1. Rotation angles for 1996 site 1.

Figure B2. Travel times for 1996 site 1 without low pass filter.

Figure B3. Travel times for 1996 site 1 with low pass filter.

Figure B4. Average velocities for 1996 site 1.

Figure B5. Interval velocities for 1996 site 1, with an 80 interval.

Figure B6. Travel times for 1996 site 3. The columns are depth (ft.), P time, S1 (in-line) time and S2 (cross-line) time.

Figure B7. Travel times for 1996 site 4. The columns are depth (ft.), P time, S1 (in-line) time and S2 (cross-line) time.

Figure B8. Travel times for 1996 site 6. The columns are depth (ft.), P time.

Figure B9. Plot of P-wave interval velocities for 1996 site 1 using a 40 ft. interval.

Figure B10. Plot of S-wave (in-line source) interval velocities for 1996 site 1 using a 40 ft. interval.

Figure B11. Plot of S-wave (cross-line source) interval velocities for 1996 site 1 using a 40 ft. interval.

Appendix C: Time Lapse and Travel Time Difference Plots

Figure C1a. Time-lapse change in P-wave travel time at site 1.

Figure C1b. Time-lapse change in S-wave (in-line source) travel time at site 1.

Figure C1c. Time-lapse change in S-wave (cross-line source) travel time at site 1.

Figure C1d. Travel time difference between S1 (in-line, E-W) and S2 (cross-line, N-S) at site 1 for 1996 and 1997 surveys.

Figure C2a. Time-lapse change in P-wave travel time at site 2.

Figure C2b. Time-lapse change in S-wave travel time at site 2 for S1 (in-line, E-W) and S2 (cross-line, N-S) for 1996 minus 1997.

Figure C2c. Travel time difference between S1 (in-line, E-W) and S2 (cross-line, N-S) at site 2 for 1996 and 1997 surveys.

Figure C3a. Time-lapse change in P-wave travel time at site 3.

Figure C3b. Time-lapse change in travel time at site 3 for S1 (in-line, E-W) and S2 (cross-line, N-S).

Figure C3c. Travel time difference between S2 (cross-line) and S1(in-line) for 1996 and 1997 surveys.

Figure C3d. Time-lapse travel time difference for site 3, S2 minus S1 and 1996 minus 1997.

Figure C4a. Time-lapse change in P-wave travel time at site 4.

Figure C4b. Time-lapse change in travel time at site 4 for S1 (in-line, E-W) and S2 (cross-line, N-S).

Figure C4c. Travel time difference between S2 (cross-line) and S1(in-line) for 1996 and 1997 surveys at site 4.

Figure C4d. Time-lapse travel time difference for site 4, S2 minus S1 and 1996 minus 1997.

Figure C5a. Time lapse P-wave time change for walkaway survey for two sensors (984 and 1016').

Figure C5b. Time lapse and spatial change for P-wave walkaway.

Figure C5c. Time lapse S-wave (cross-line source) time change for walkaway survey for two sensors (984 and 1016').

Figure C5d. Time lapse and spatial change for S-wave (cross-line source) time change for walkaway survey for two sensors (984 and 1016').

Figure C6. Time lapse P-wave time change for site 6 (1996 - 1997).

Appendix D: Other Studies and Analysis

Figure D1a. Particle motion for comparison for 1997 site 1 S-waves. S1 (in-line, E-W) source (left side) and S2 (cross-line, N-S) source (right side). Level number is sequential from shallowest (96 ft.).

Figure D1b. Particle motion for comparison for 1997 site 1 S-waves. S1 (in-line, E-W) source (left side) and S2 (cross-line, N-S) source (right side). Level number is sequential from shallowest (96 ft.).

Figure D2a. Upgoing data from 1996 site 1 P-wave source after F-K filter.

Figure D2b. Upgoing data from 1997 site 1 P-wave source after F-K filter.

Figure D3a. Frequency vs time (top) and spectra (bottom) plot for average of two farthest 1996 walkaway P-wave sites for sensor at 984 ft.

Figure D3b. Frequency vs time (top) and spectra (bottom) plot for average of two farthest 1996 walkaway P-wave sites for sensor at 1016 ft.

Figure D3c. Frequency vs time (top) and spectra (bottom) plot for average of two farthest 1997 walkaway P-wave sites for sensor at 984 ft.

Figure D3b. Frequency vs time (top) and spectra (bottom) plot for average of two farthest 1997 walkaway P-wave sites for sensor at 1016 ft.

Appendix E - Surface Seismic Analysis

Figure E1. Location map of some surface seismic lines and wells in the Royal Center field. The surface lines analyzed are RC-1 and RC-5 which intersect near VSP well 157.

Figure E-2. Example CDP gathers from surface line RC-5 (left) and RC-1 (right) near the intersection of the lines. The reflector at about 0.17 s is the top of the Trenton reservoir formation.

Figure E-3. CDP stacked sections for surface lines RC-1 (left, CDPs 576 - 596) and RD-5 (right, CDPs 618- 638) with the well 157 site 1 VSP P-wave upgoing stack displayed in the middle (labeled as CDP 1). The top of the Trenton reservoir formation is at about 0.18 s.

Figure E-4. Ray trace modeling of surface seismic CDP gather at Royal Center field using the velocity model derived from the well 157 VSP. The lack of variation in reflection angle of incidence at the Trenton reservoir formation (about 970 ft.) shows the limitations on any AVO analysis.

References

Alford, R.M., 1986. Shear data in the presence of azimuthal anisotropy, 56th Ann. Internat. Mtg., Soc. Explor. Geophys., Expanded Abstracts.

Carmichael, R.S., Handbook of Physical Properties of Rocks, Volume II, CRC Press, Inc., 1982.

Crampin, S., Bush, I., Naville, C and Taylor, D., 1986. Estimating the internal structure of reservoirs with shear-wave VSPs, *Leading Edge*, 5, 35-39.

Daley, T.M., T.V. McEvilly, and E.L. Majer, 1988. Analysis of P and S Wave Vertical Seismic Profile Data From the Salton Sea Scientific Drilling Project, *J. Geophys. Res.*, .R 93, B11, p13025-13036.

Daley, T.M. and T.V. McEvilly, Shear wave anisotropy in the Parkfield Varian Well VSP, *Bull. Seism. Soc. Am.*, 80, 857-869, 1990.

Gassmann, F., 1951. Uber die Elastizitat poroser Medien. *Vier. der Natur. Gesllschaft in Zurich.*, 96, p1-23.

Jech, J., and Psencik, I., 1992. Kinematic inversion for qP- and qS-waves in homogeneous hexagonally symmetric structures, *Geophys. J. Int.*, 108, 604-612.

Liu, E., Crampin,S. and Queen, J.H. and Rizer, W.D., 1993, Velocity and attenuation anisotropy caused by microcracks and macrofractures from multi-azimuthal reverse VSPs, *Canadian Journal of Exploration Geophysicists*, 29, 177-188.

Majer, E. L., McEvilly T. V., Eastwood F., and Myer L., 1988, Fracture detection using P-wave and S-wave vertical seismic profiling at the Geysers, *Geophysics*, 53, 76-84.

Mavko, G., Mukerji, T., Dvorkin, J., 1998, The rock physics handbook: Tools for seismic analysis in porous media, Cambridge University Press.

O'Connell, R.J., and Budiansky, B., Seismic Velocities in Dry and Saturated Cracked Solids, *Journal of Geophysical Research*, 79, n35, p5412-5426.

Pyrak-Nolte, L.J., Myer, L.R., and Cook, N.G.W, 1990. Anisotropy in Seismic Velocities and Amplitudes from Multiple Parallel Fractures, *Journal of Geophysical Research*, 95, nB7, p11345-11358.

Schoenberg, M., and Sayers, C.M., Seismic Anisotropy of fractured rock, *Geophysics*, 60, n1, p204-211.

Thomsen, L., 1988. Reflection seismology over azimuthally anisotropic media, *Geophysics*, 53, 304-313.

Winterstein, D.F., and Meadows, M.A., 1991. Shear-wave polarizations and subsur face stress directions at Lost Hills field, *Geophysics*, 56, 1331-1348.

This manuscript was prepared with the AGU LaTeX macros v3.0.

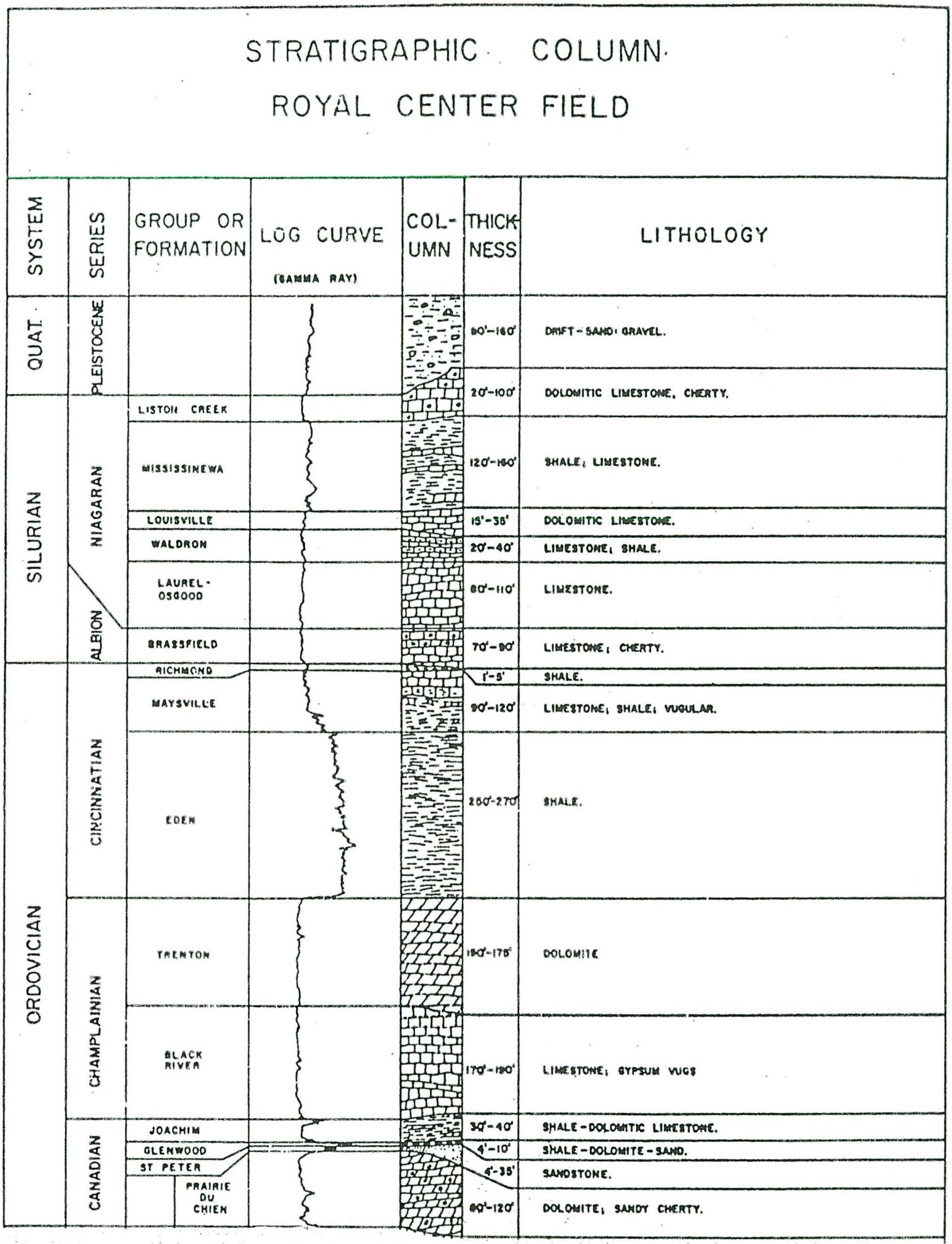

Figure 1. Geologic column for the Royal Center field. The approximate depths of major units at the VSP well 157 are: Glacial Till 0-150 ft., Silurian limestone and shale 150-675 ft., Eden shale 675 - 930 ft., Trenton dolomite 930 - 1100 ft.

NIPSCO VSP Experiment Objectives

Objective 1: Determine fracture orientation from s-wave splitting.

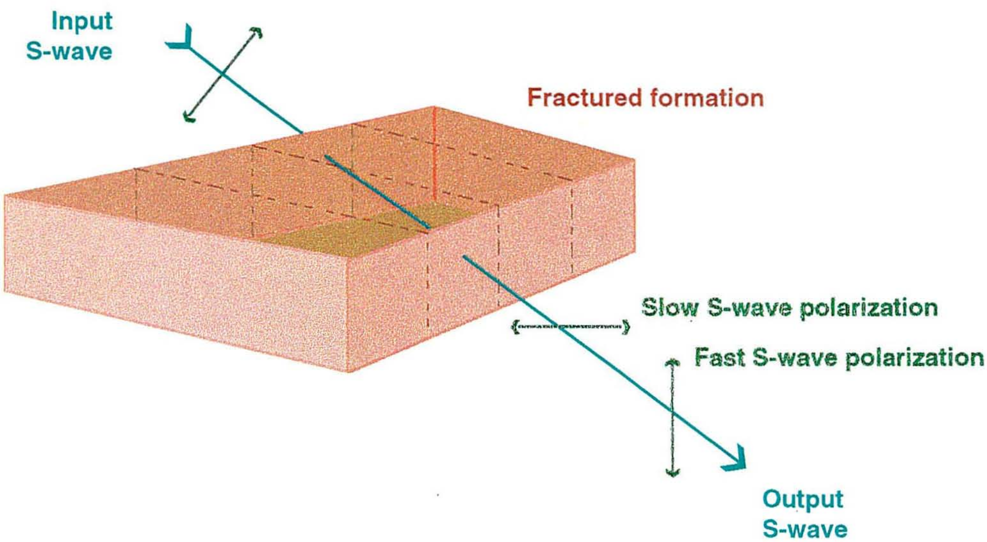

Objective 2: Estimate fracture location from winter/summer changes in P & S wave attributes

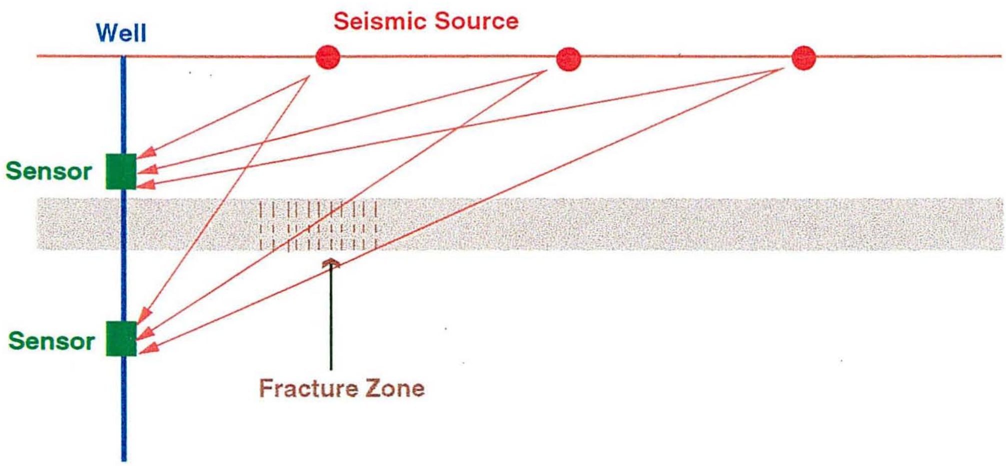

Figure 2. Schematic objectives of NIPSCO VSP.

NIPSCO VSP DESIGN

Concept - Equal Offset Distance, Multiple Azimuths
Acquire at Productive and Non-Productive Wells
Acquire at Maximum and Minimum Gas Pressures

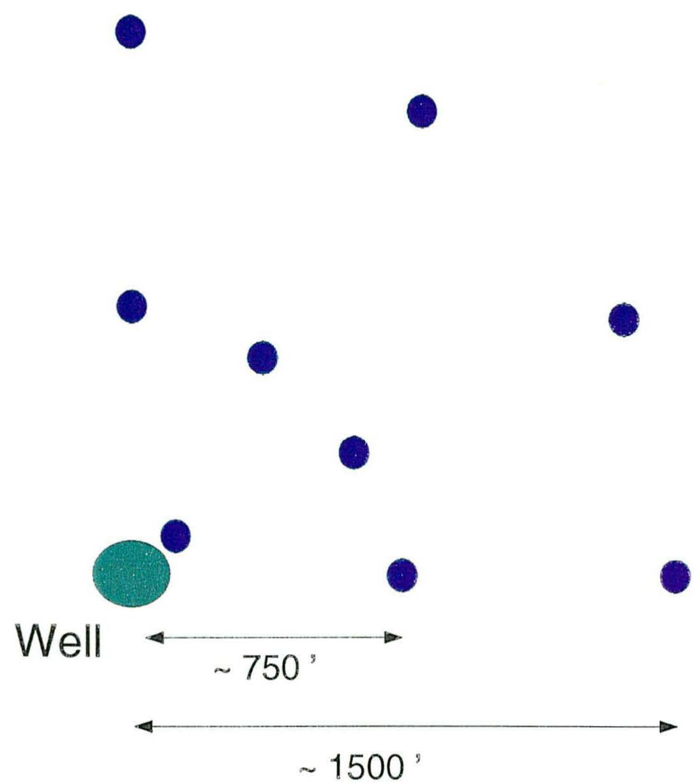

● = 9-Component VSP Source Location

Figure 3. Original design concept for NIPSCO VSP.

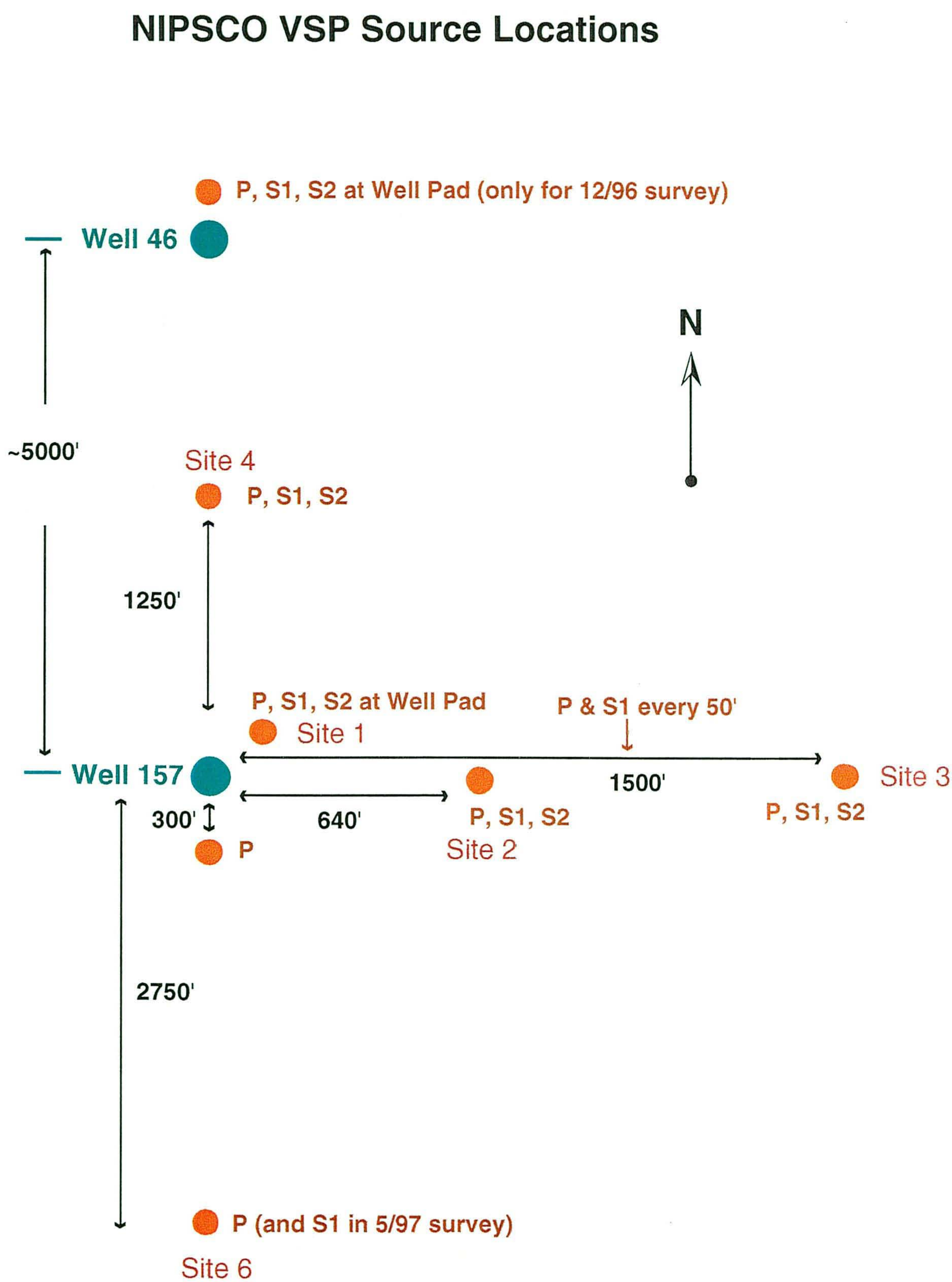

Figure 4. Seismic source locations for NIPSCO VSP data acquisition. Field conditions and local access laws prevented locations as in original concept (Figure 2).

Figure 5. Sixty ft. lubricator pipe used to introduce multi-level sensor string in the presurized VSP well.

Example of noise bursts in uncorrelated data (left) and after automatic editing (right)

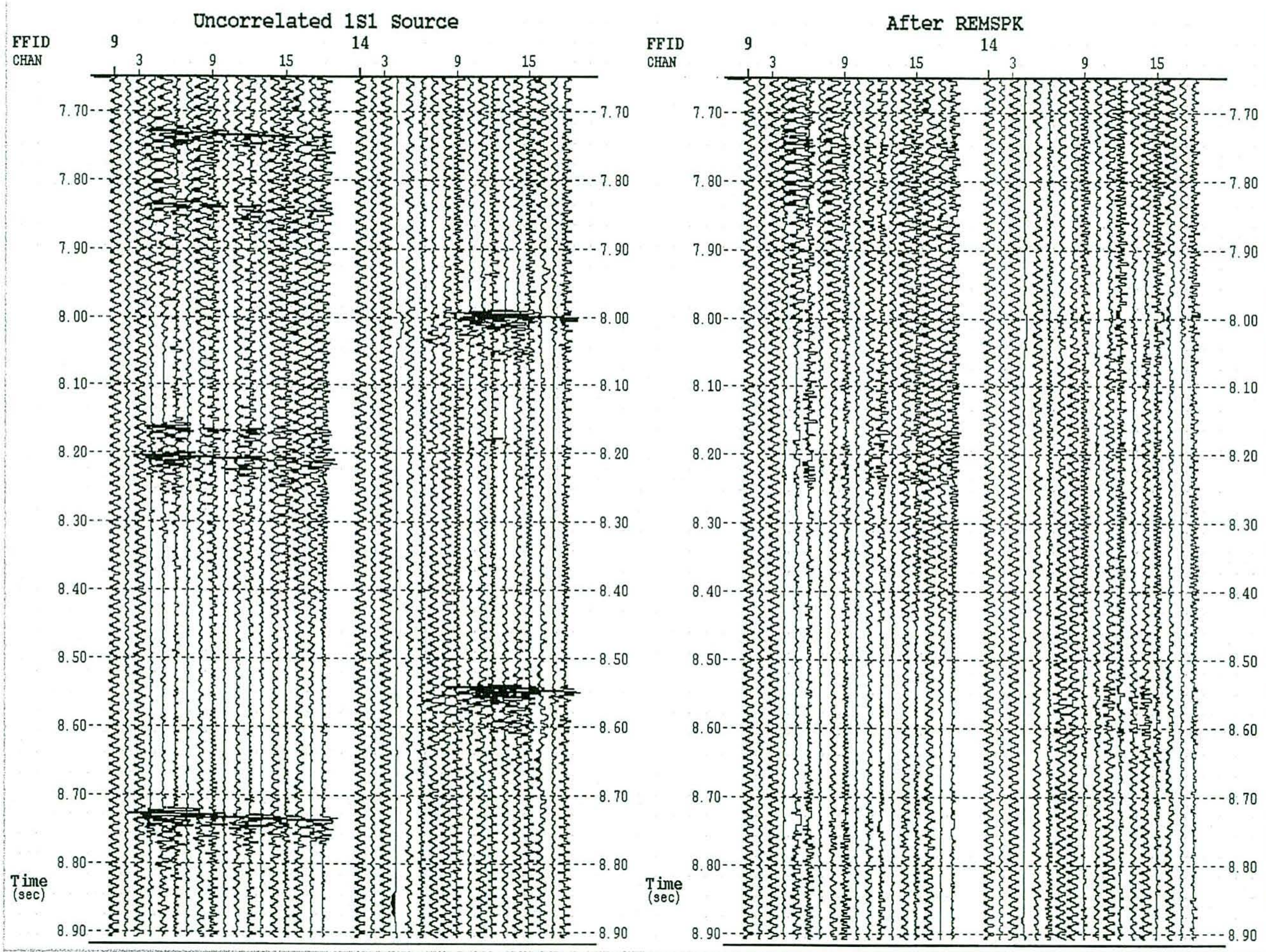

Figure 6. Uncorrelated vibroseis data showing effects of automatic noise burst editor before (left) and after (right) edits.

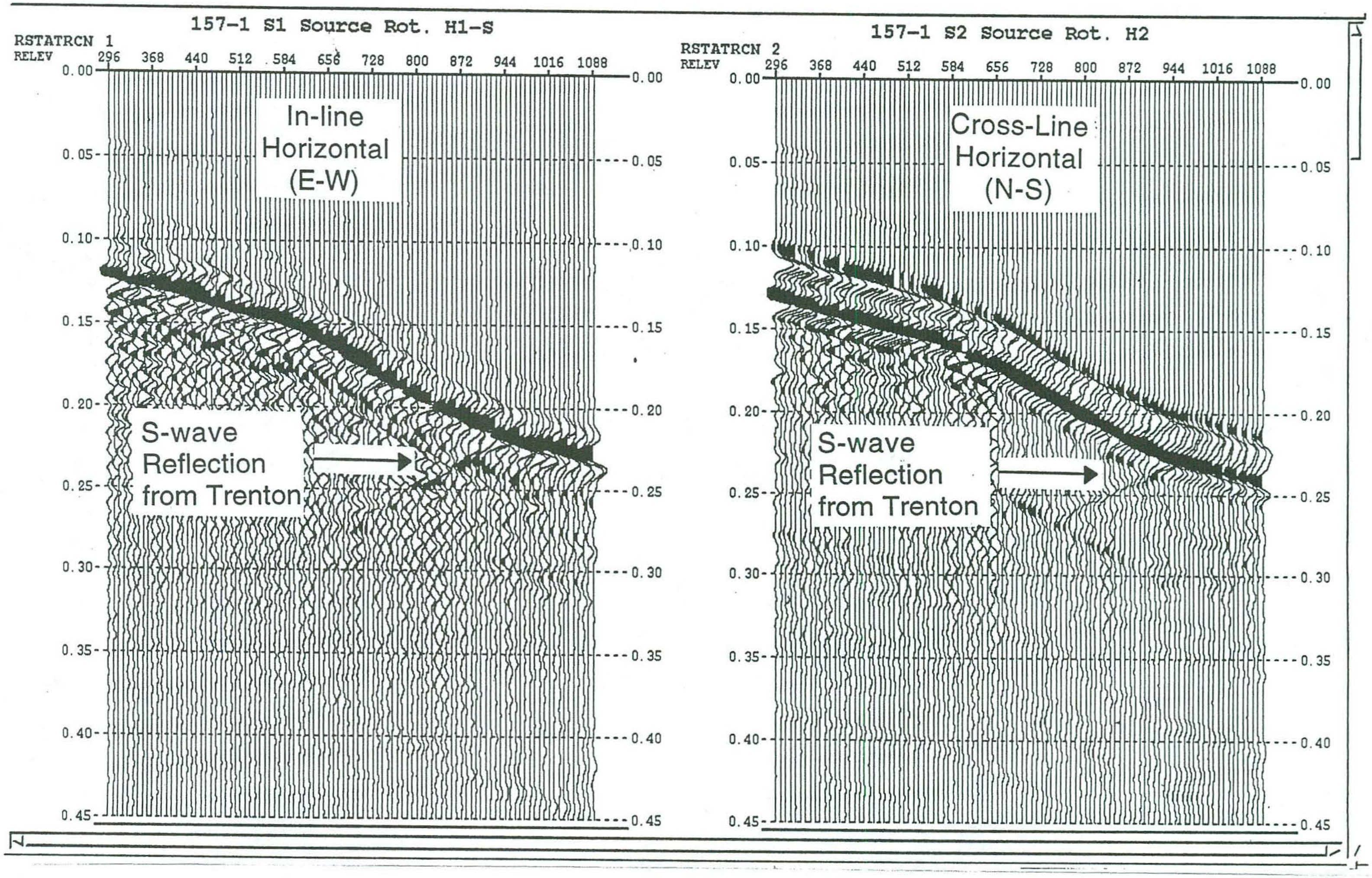

Figure 7a. Seismograms from orthogonal S-wave experiment at site 1. The left side data set is in-line horizontal oriented sensors recording an in-line oriented S-wave source over the depth range 296 ft. to 1088 ft. The right side data set is cross-line horizontal oriented sensors recording a cross-line oriented S-wave source over the same depth range. These data sets are used for estimating shear wave anisotropy which can be controlled by subsurface fracturing.

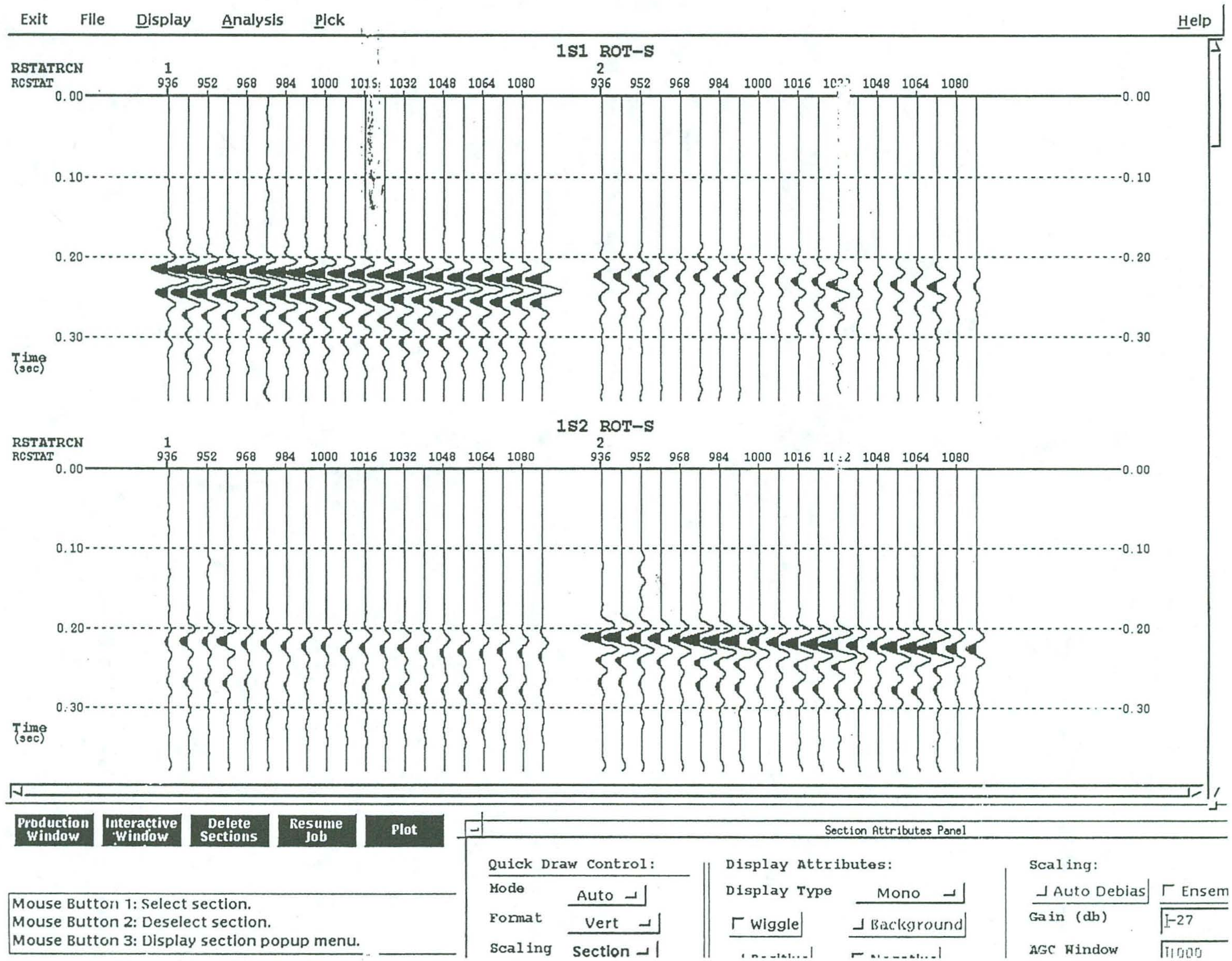

Figure 7b. Four orthogonal S-wave recordings for depths 936 to 1088 ft (the approximate reservoir zone). Top-left is in-line source and in-line sensor (XX), top-right is in-line source and cross-line sensor (XY), bottom-left is cross-line source and in-line sensor (YX), bottom-right is cross-line source and cross-line sensor (YY). The seismograms are no[illegible]ized [illegible]he [illegible]mu[illegible] [illegible]eac[illegible] [illegible]urc[illegible]

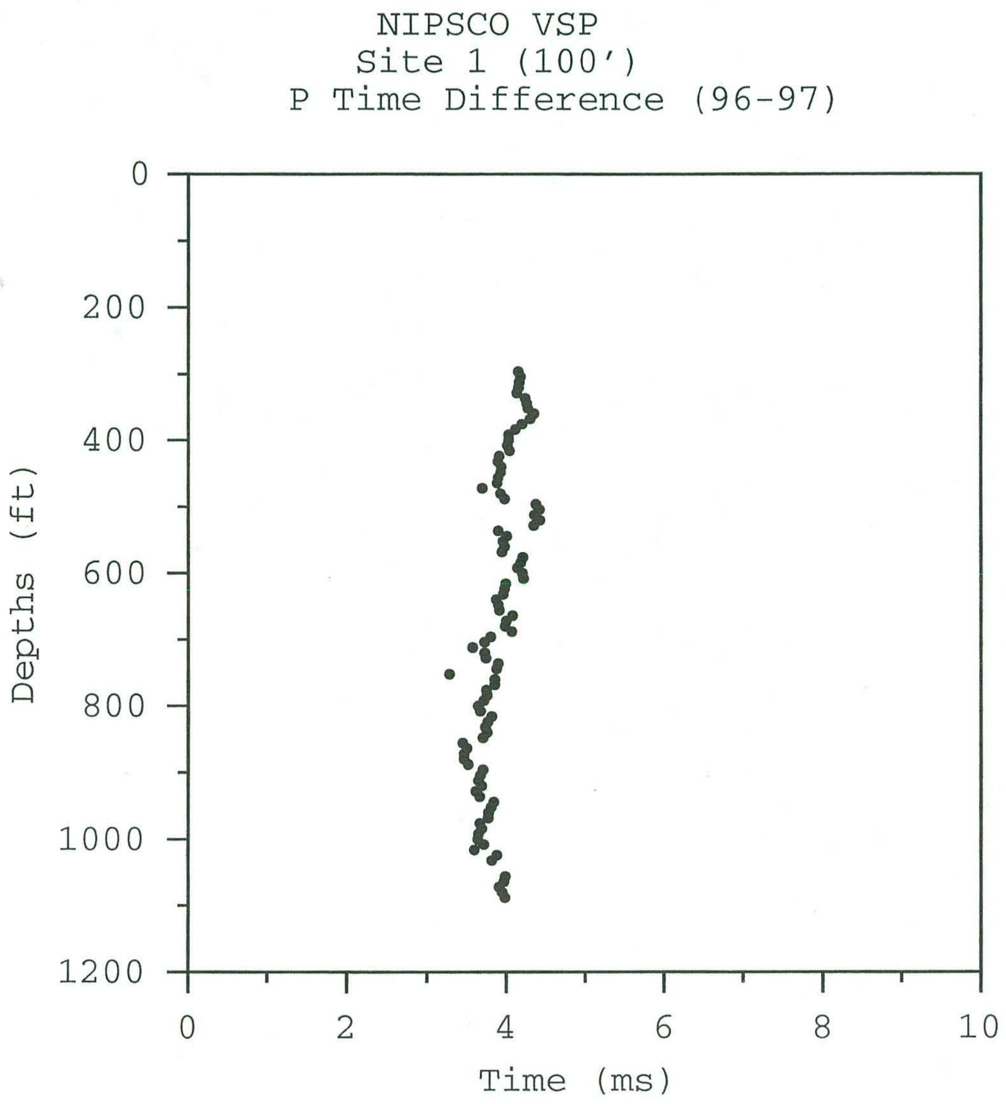

Figure 8a. Time lapse change in P-wave travel time for site 1. Times are 1996 data (gas saturated reservoir) minus the 1997 times (water saturated reservoir).

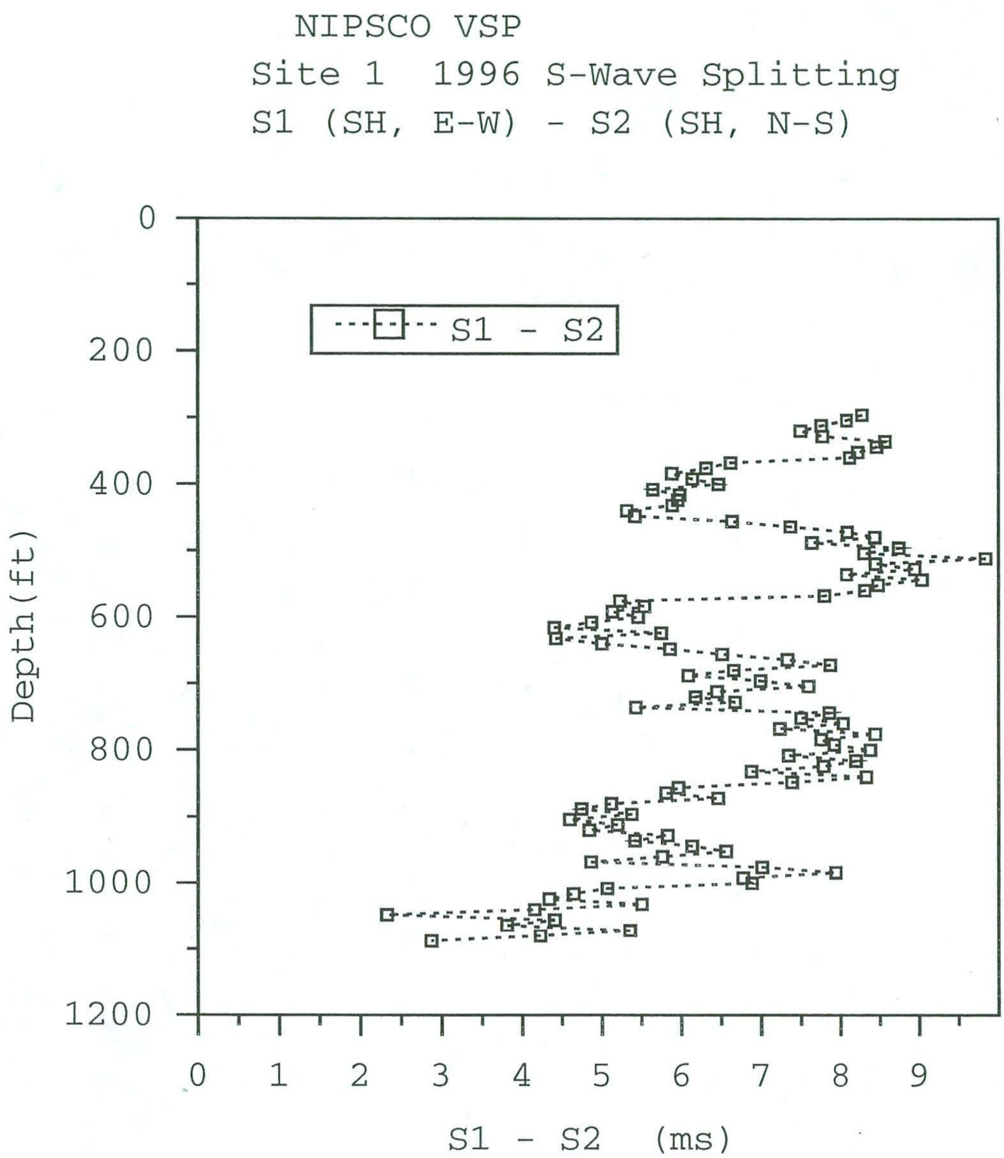

Figure 8b. S-wave splitting in terms of travel time difference (S1 (in-line, east-west) source minus S2 (cross-line, north-south) source for site 1 in 1996 (gas saturated reservoir).

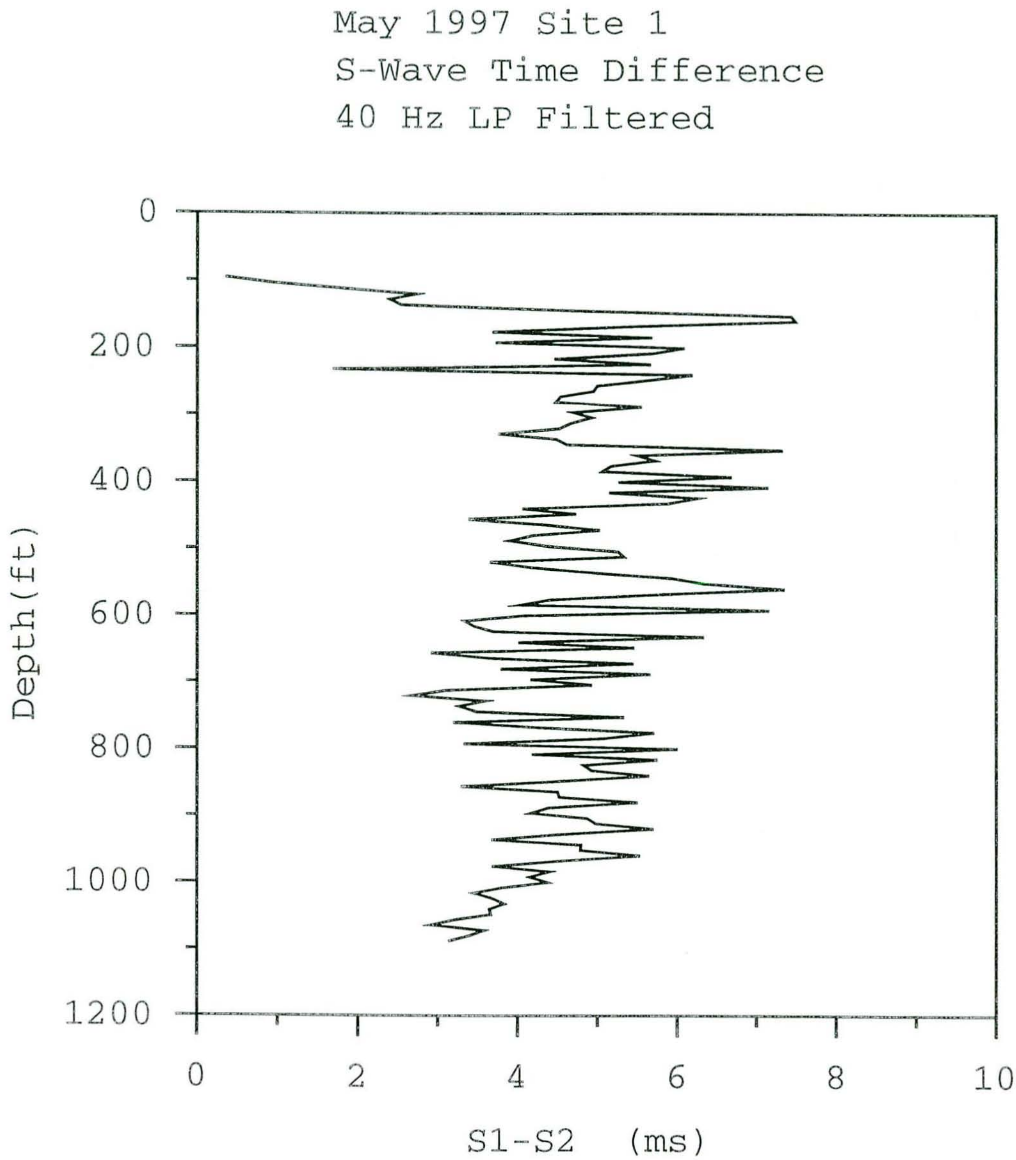

Figure 8c. S-wave splitting in terms of travel time difference (S1 (in-line, east-west) source minus S2 (cross-line, north-south) source for site 1 in 1997 (water saturated reservoir).

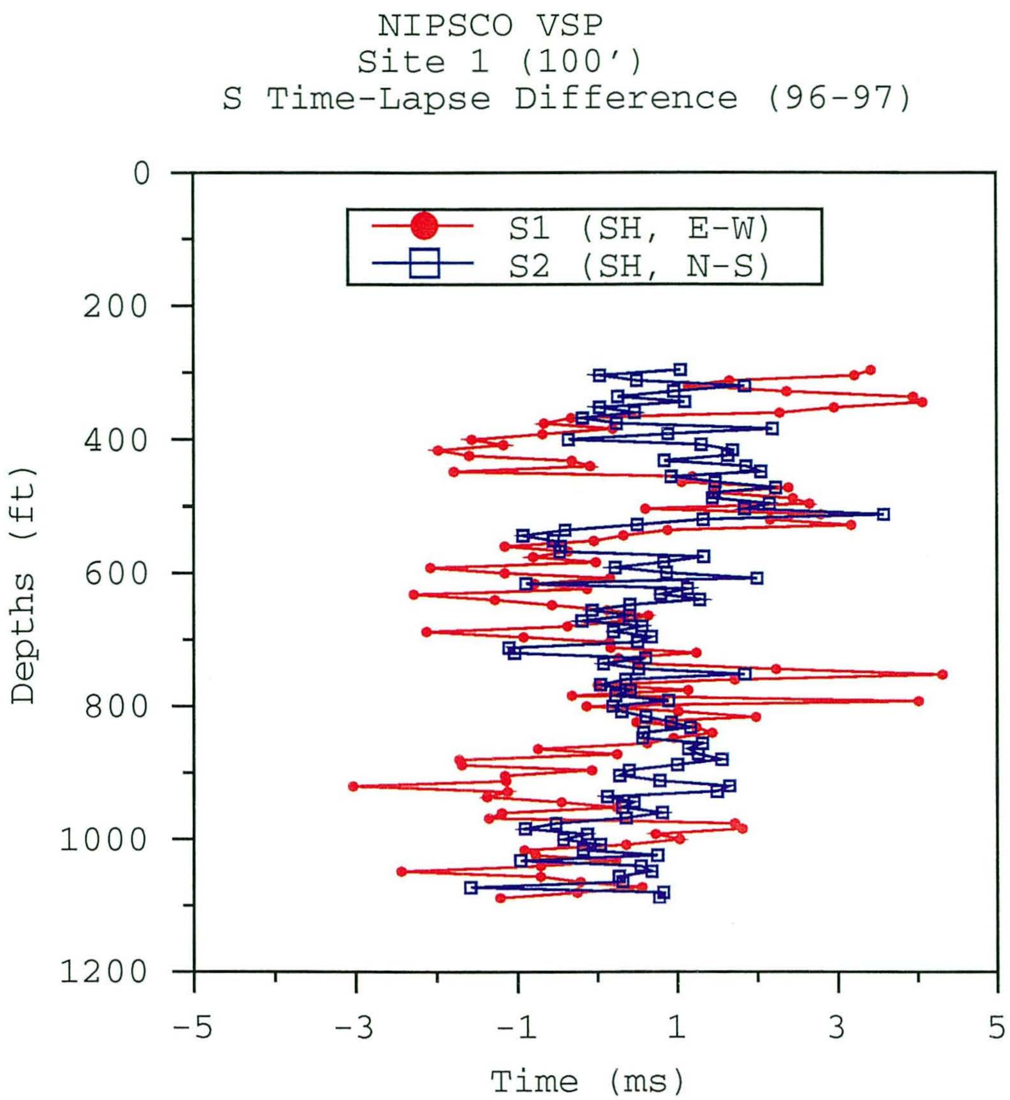

Figure 8d. Time lapse change in S-wave travel time for site 1. Times are 1996 data (gas saturated reservoir) minus the 1997 times (water saturated reservoir) for S1 (in-line, east-west) source and S2 (cross-line, north-south) source.

NIPSCO VSP Site 1 1997

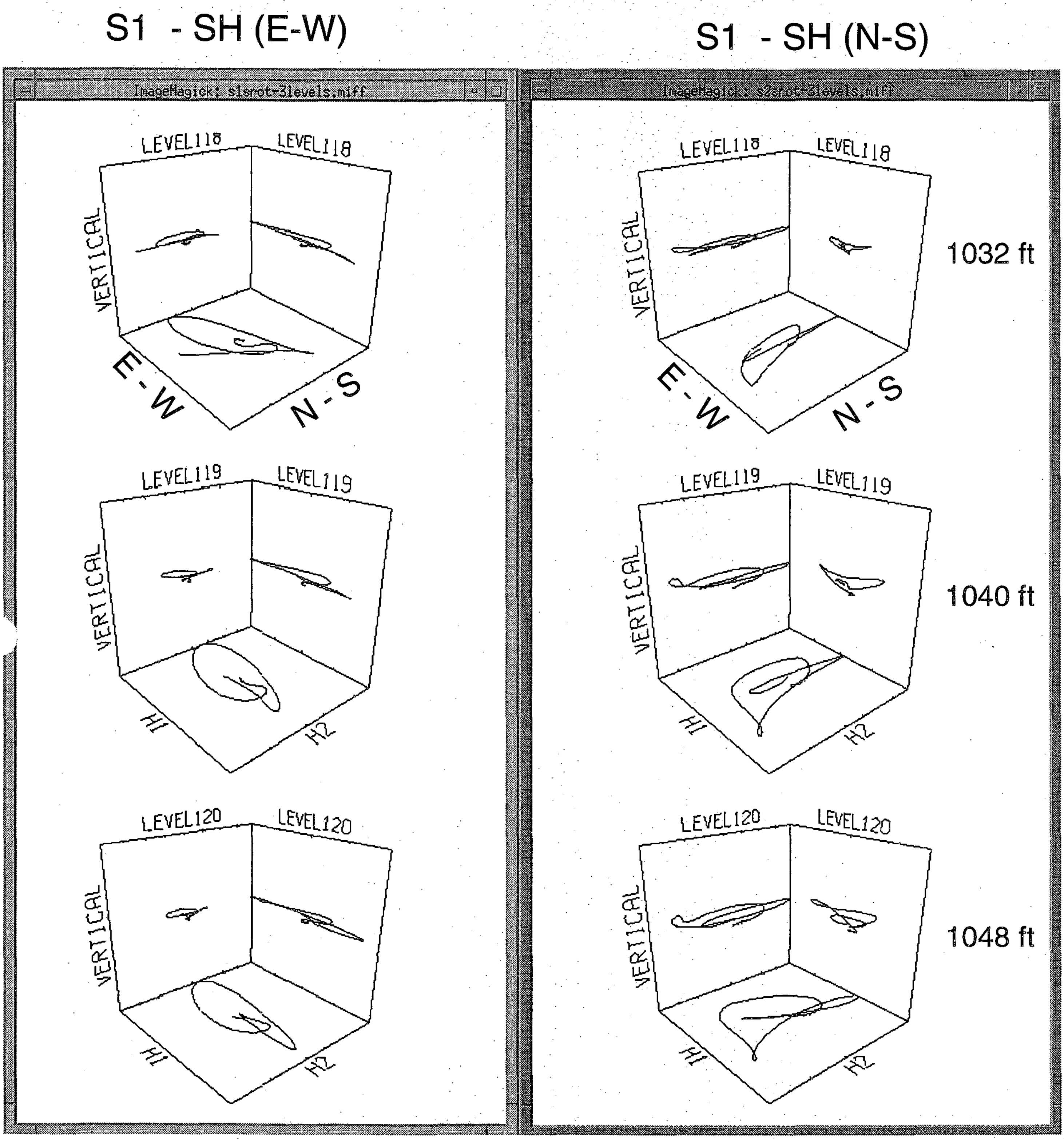

Figure 9. Comparison of S-wave hodograms (particle motion) for in-line (east-west) source polarization (left) and cross-line (north-south) source polarization (right) for three depths within or below the reservoir. The S-wave polarization is dominantly isotropic with some ellipticity and a moderate east-west component on the cross-line (north-south) source data (right).

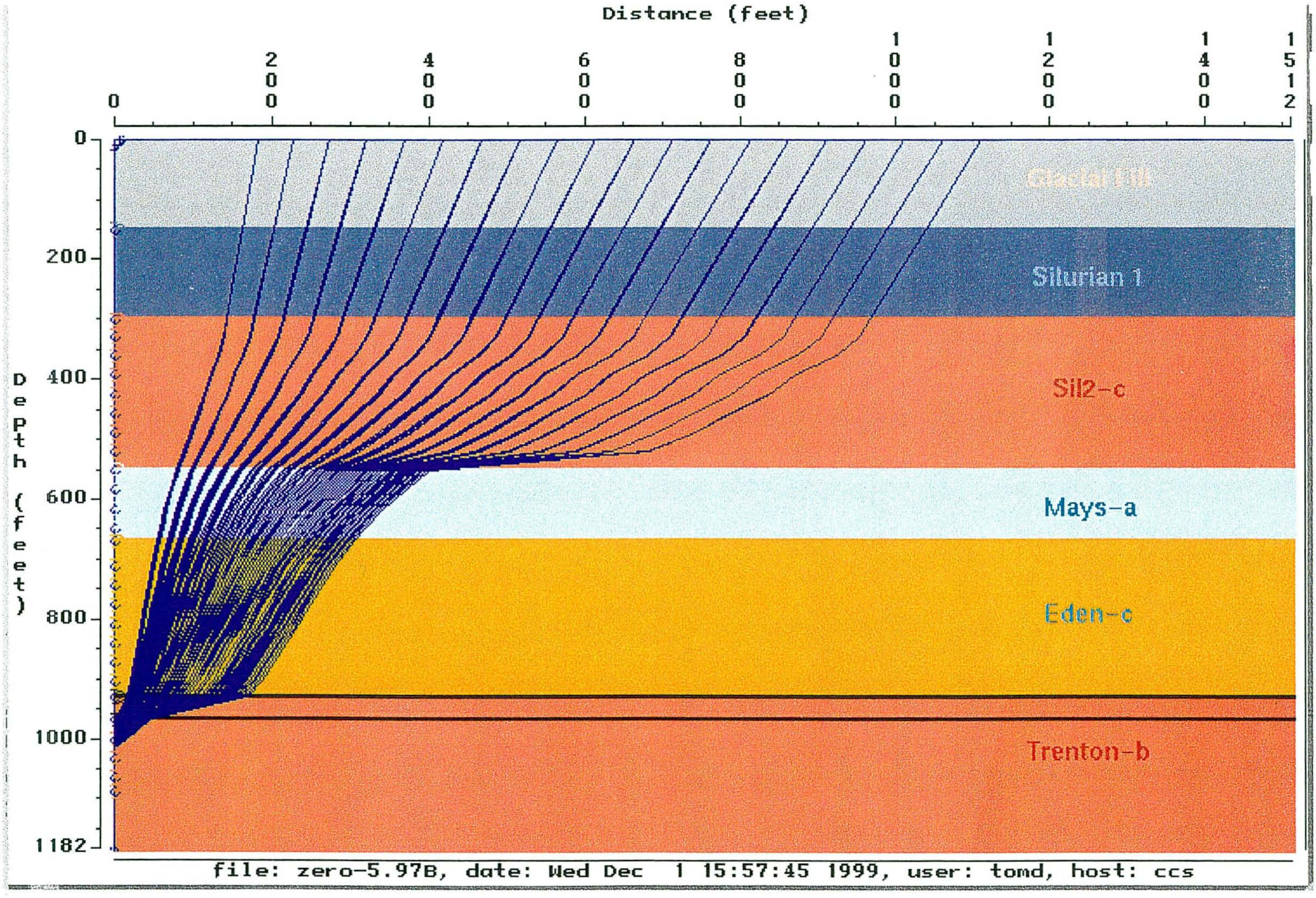

Figure 10a. Ray tracing for P-wave walkaway survey. Note that very little propagation occurs in the Trenton formation. Velocities are from the 1997 site 1 VSP modified to better match the walkaway travel times.

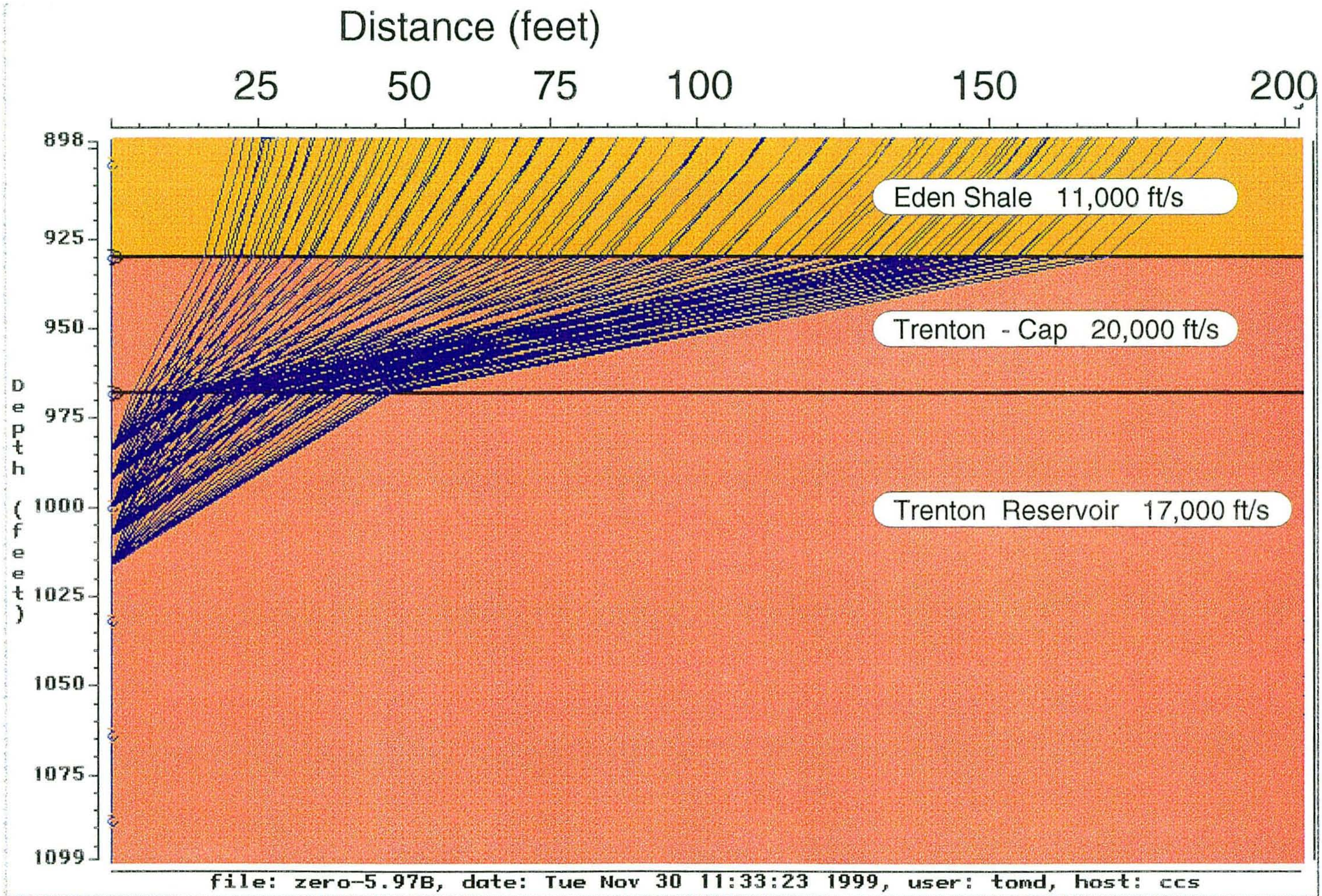

Figure 10b. Close-up view of raypaths within the reservoir zone of the Trenton. A conceptual model of an unfractured Trenton cap with minimal fracturing above a highly fractured Trenton reservoir was applied to estimate the raylengths within the reservoir. These raylengths were used in the fracture density and saturation estimates for the reservoir. The five sensor locations are the walkaway sensor depths.

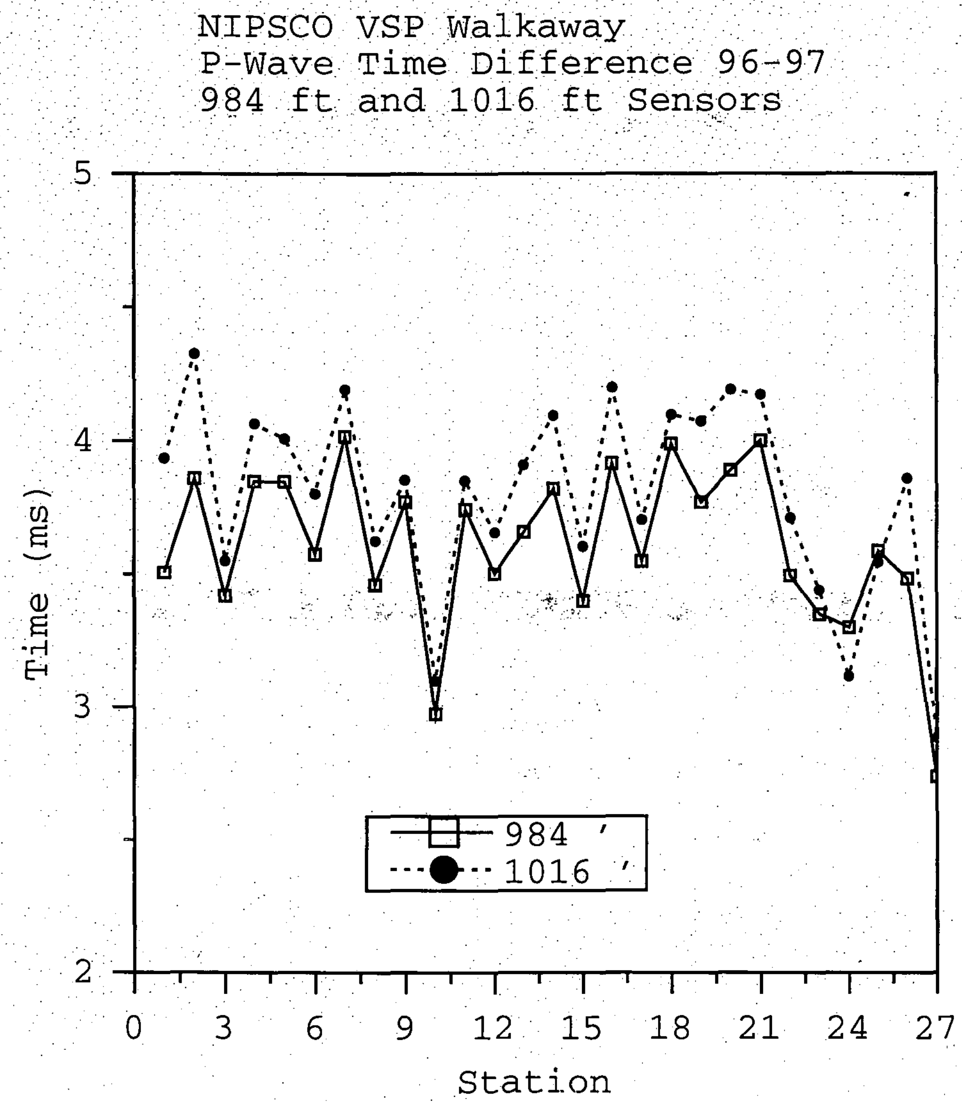

Figure 11. Time lapse changes in P-wave travel time for top and bottom walkaway sensors. The sensors were not moved between each station recording. Times were picked on the unrotated vertical component. The station spacing was 50 ft. The difference between these two curves provides the estimate of time-lapse velocity changes between gas filled and water filled reservoir conditions using the raylengths estimated raytracing (Figure 10). The average difference for all stations between the 1016 and 984 ft sensors is 0.2 ms with a standard deviation of 0.1 ms.

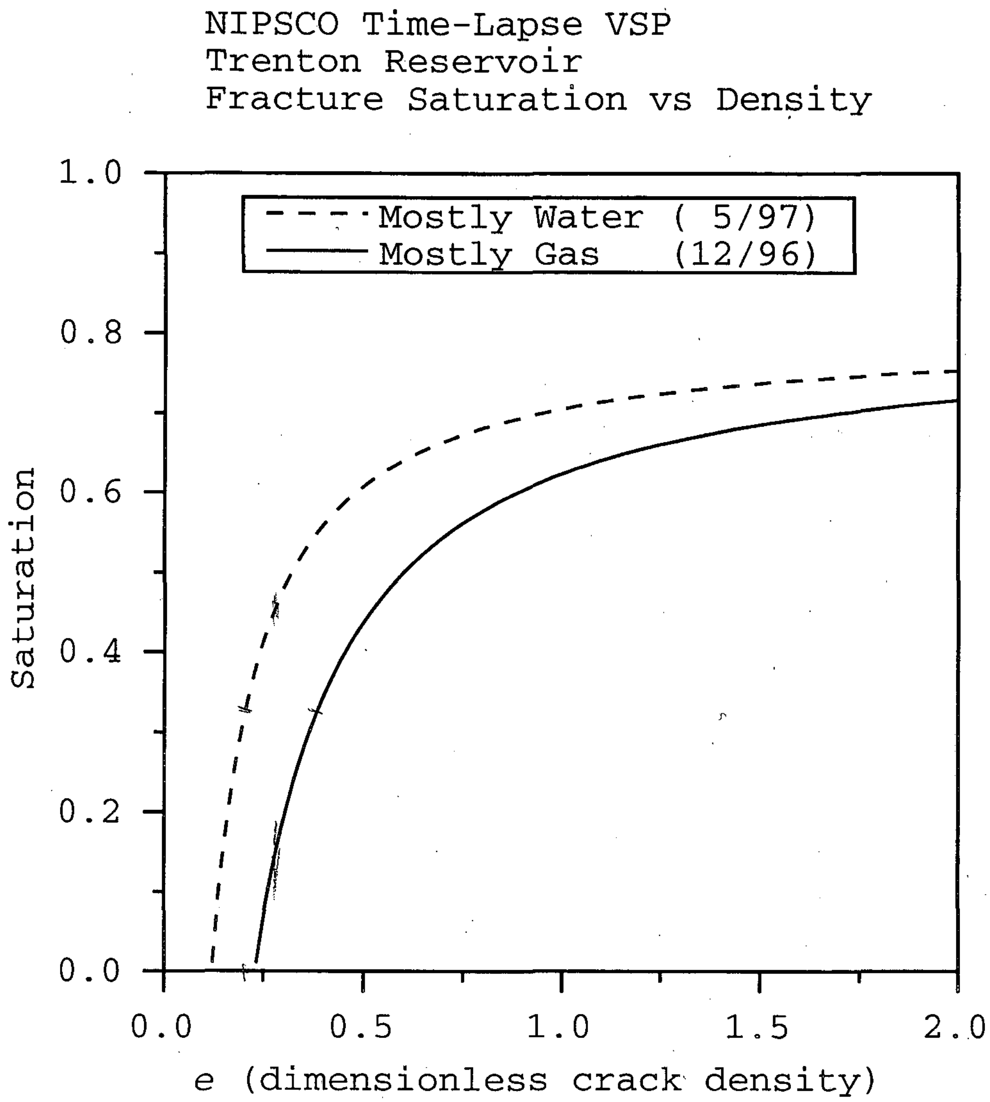

Figure 12. Trade off curves for dimensionless crack density ϵ and saturation ϕ for the two VSP surveys. The difference between the curves for a given ϵ represents the partial saturation used for gas storage.

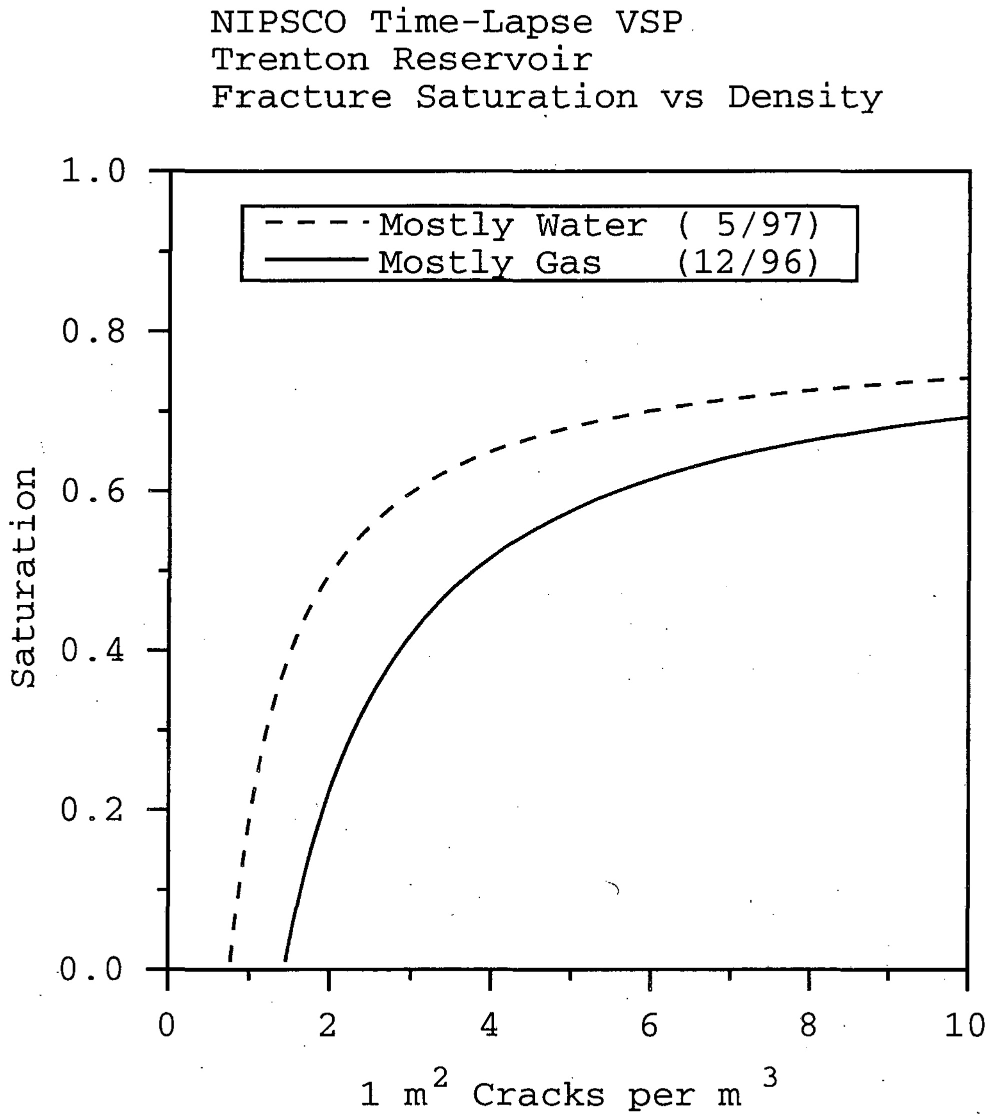

Figure 13. Trade off curves for volumetric crack density and saturation ϕ for the two VSP surveys using a 1 m^2 circular fracture. The difference between the curves for a given crack volume represents the partial saturation used for gas storage.

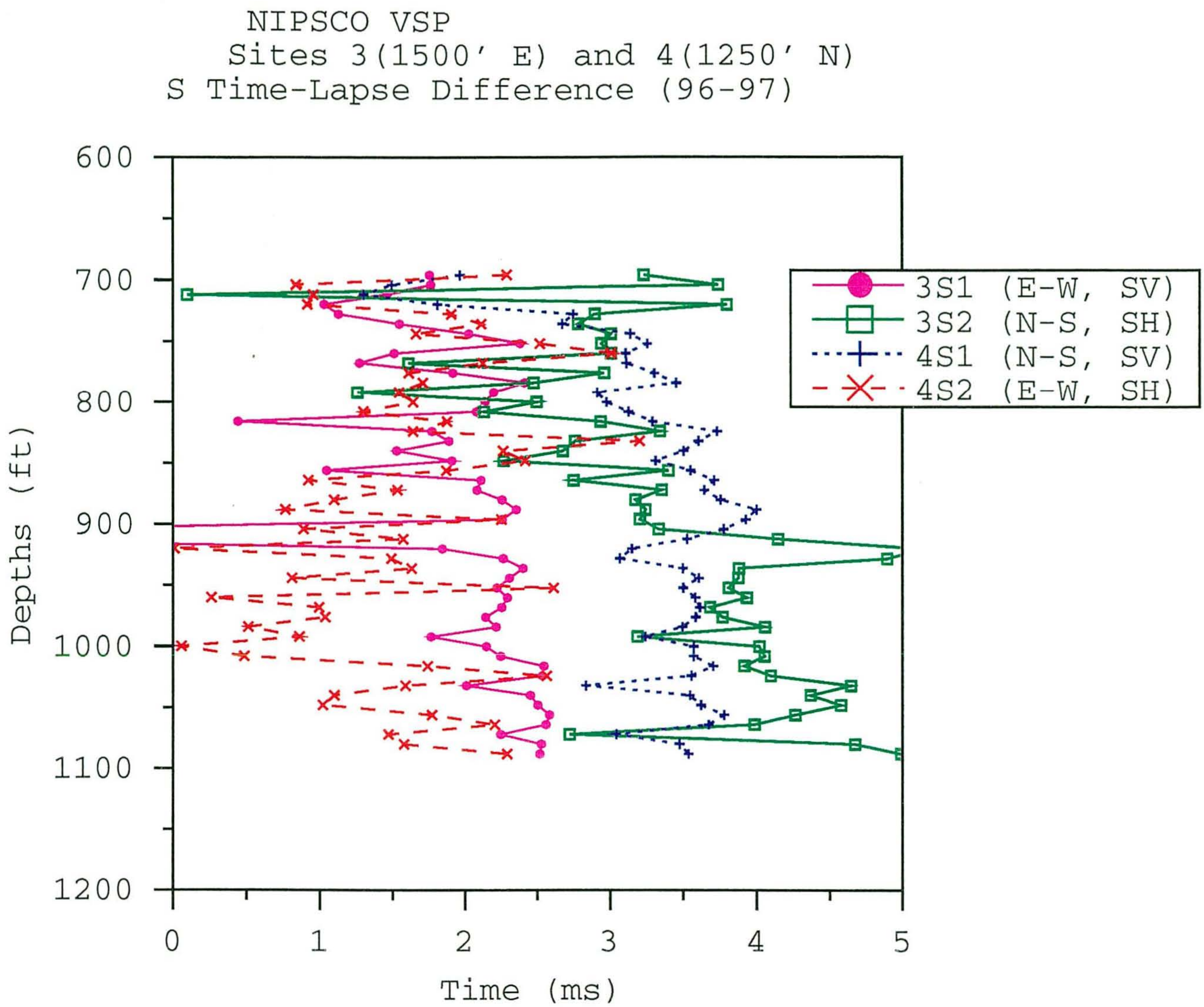

Figure 14. Time-lapse changes in S-wave travel time between 1996 (gas saturated reservoir) and 1997 (water saturated reservoir) VSP surveys. The north-south polarized S sources have larger time changes than the east-west polarized sources.

Appendix A: VSP Data Plots

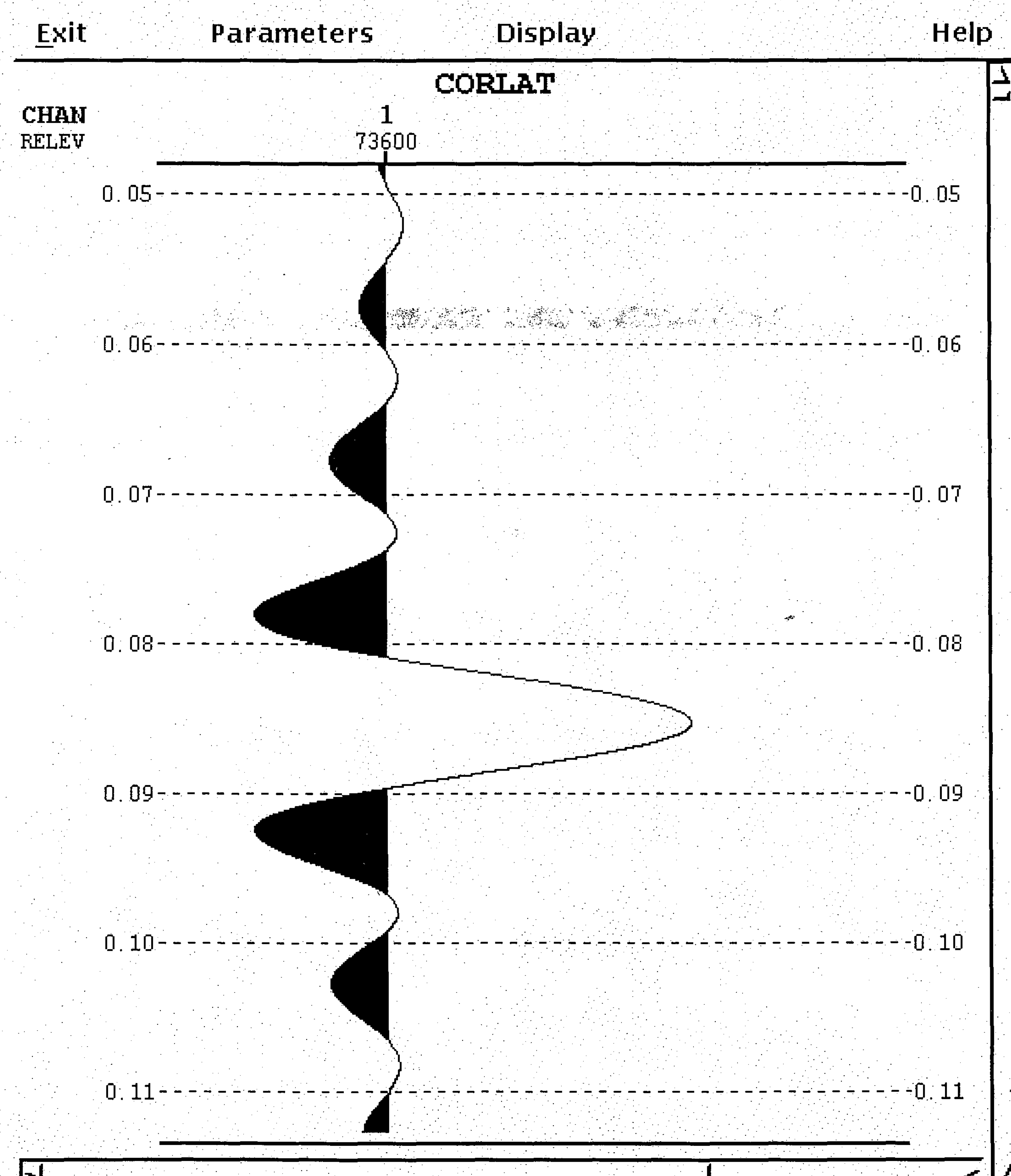

Figure A1. Cross correlation of two Pelton generated sweeps showing 85 ms delay due to varying trigger time shift in 1996 data set.

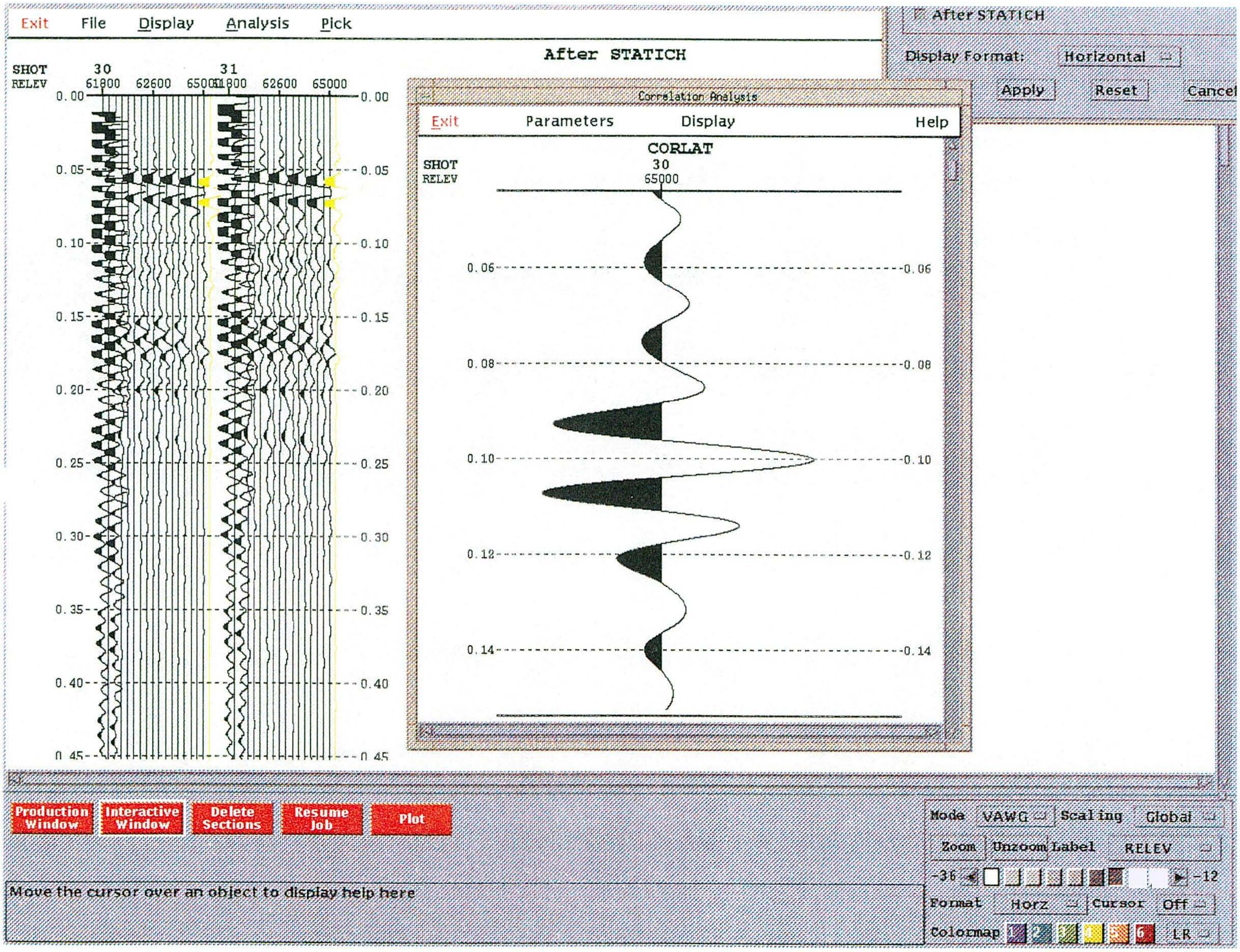

Figure A2. Cross correlation of two data traces with a 100 ms time shift added to show full wavelet. 85 ms delay from figure A1 has been removed.

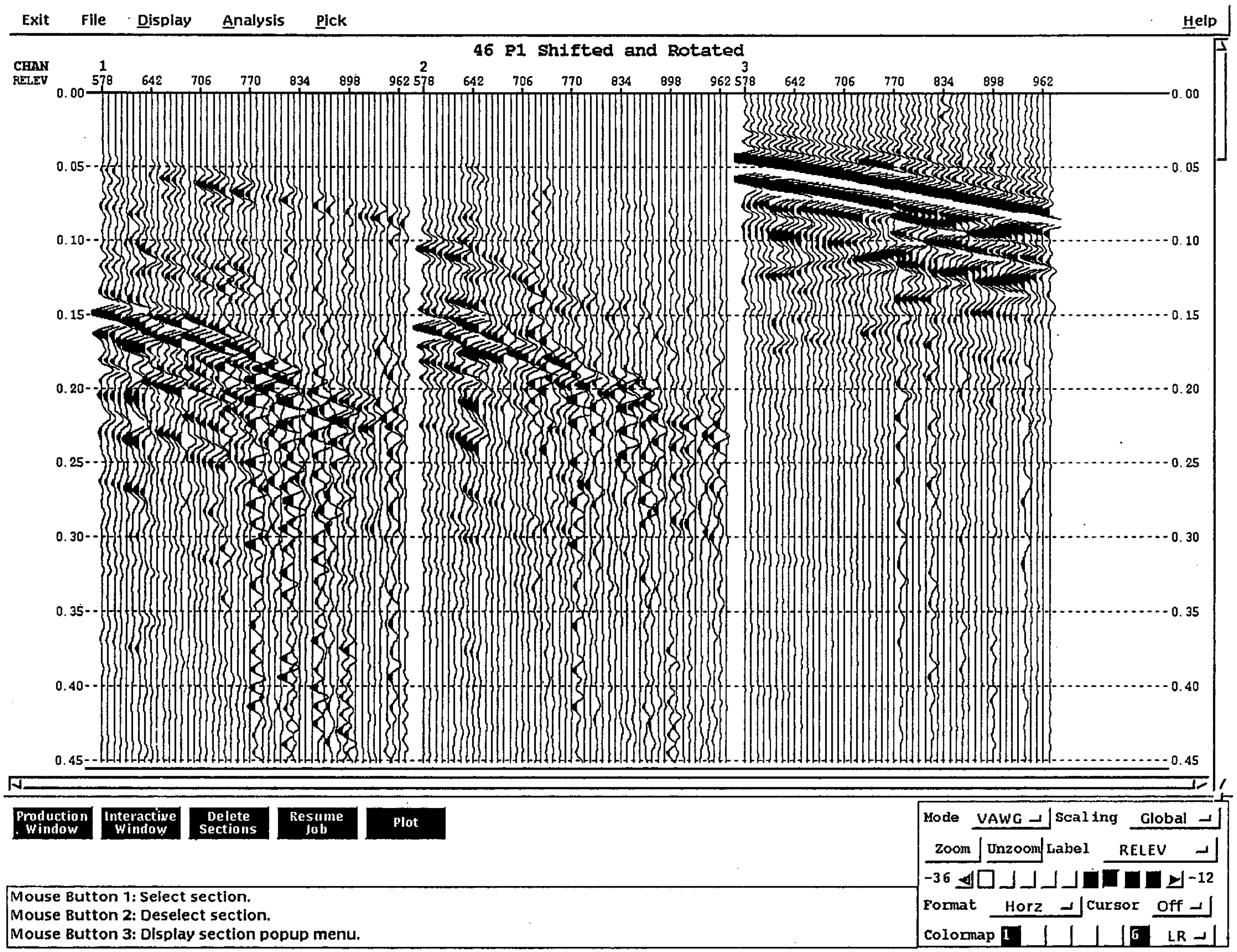

Figure A3a - A3c. Seismograms from Well 46, 1996. The three panels are geophone components horizontal in-line (left), horizontal cross-line (center), and vertical (right). The traces have been rotated (using P-wave particle motion) and are scaled using the maximum of all three panels. A3a is P-wave source, A3b is S-wave in-line source, A3c is S-wave cross-line source.

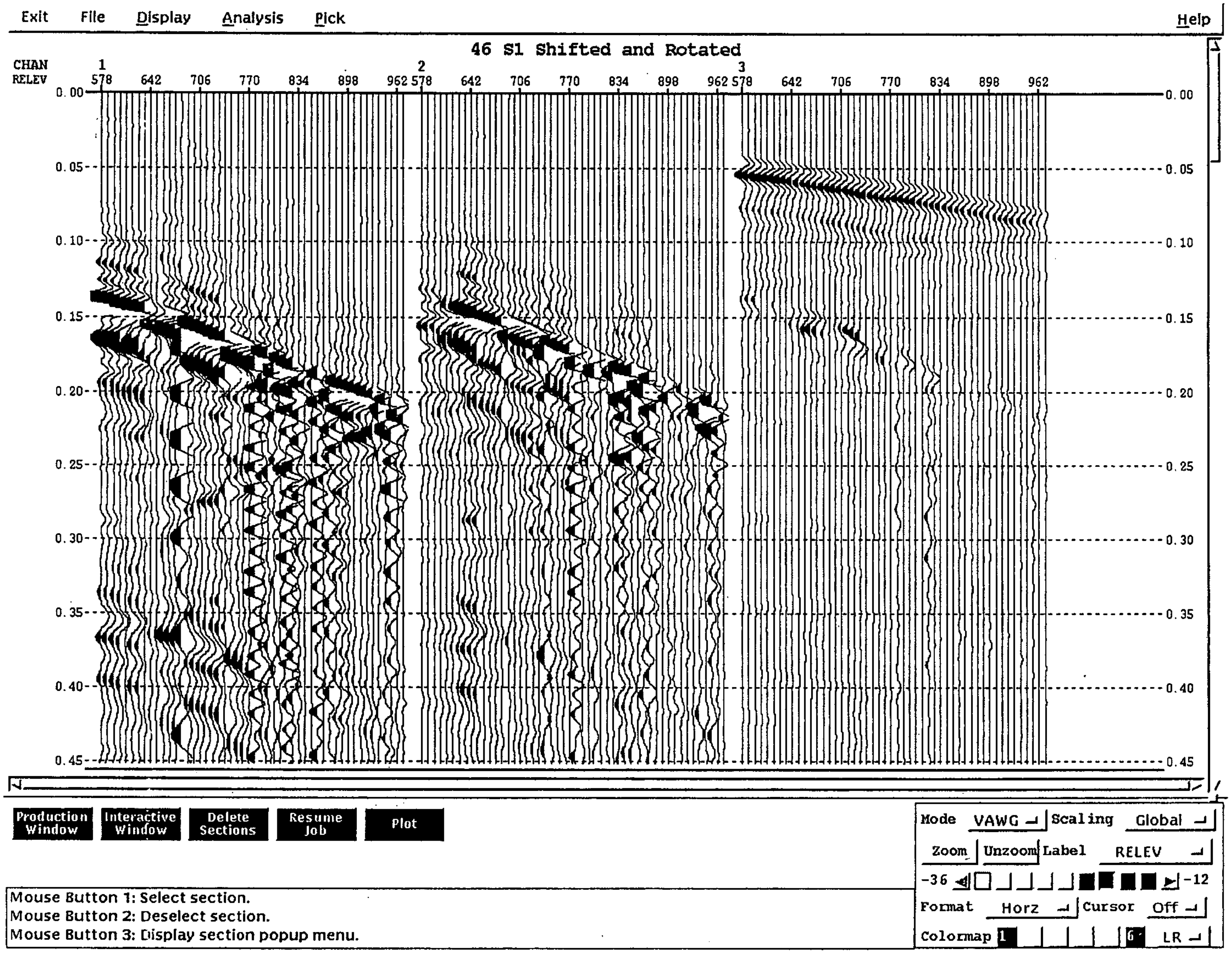
Exit File Display Analysis Pick
Help
46 S1 Shifted and Rotated
CHAN
RELEV
1 2 3
578 642 706 770 834 898 962
0.00 0.05 0.10 0.15 0.20 0.25 0.30 0.35 0.40 0.45
Production Window
Interactive Window
Delete Sections
Resume Job
Plot
Mouse Button 1: Select section.
Mouse Button 2: Deselect section.
Mouse Button 3: Display section popup menu.
Mode VAWG
Scaling Global
Zoom Unzoom Label RELEV
-36 -12
Format Horz Cursor Off
Colormap LR

Figure A3b

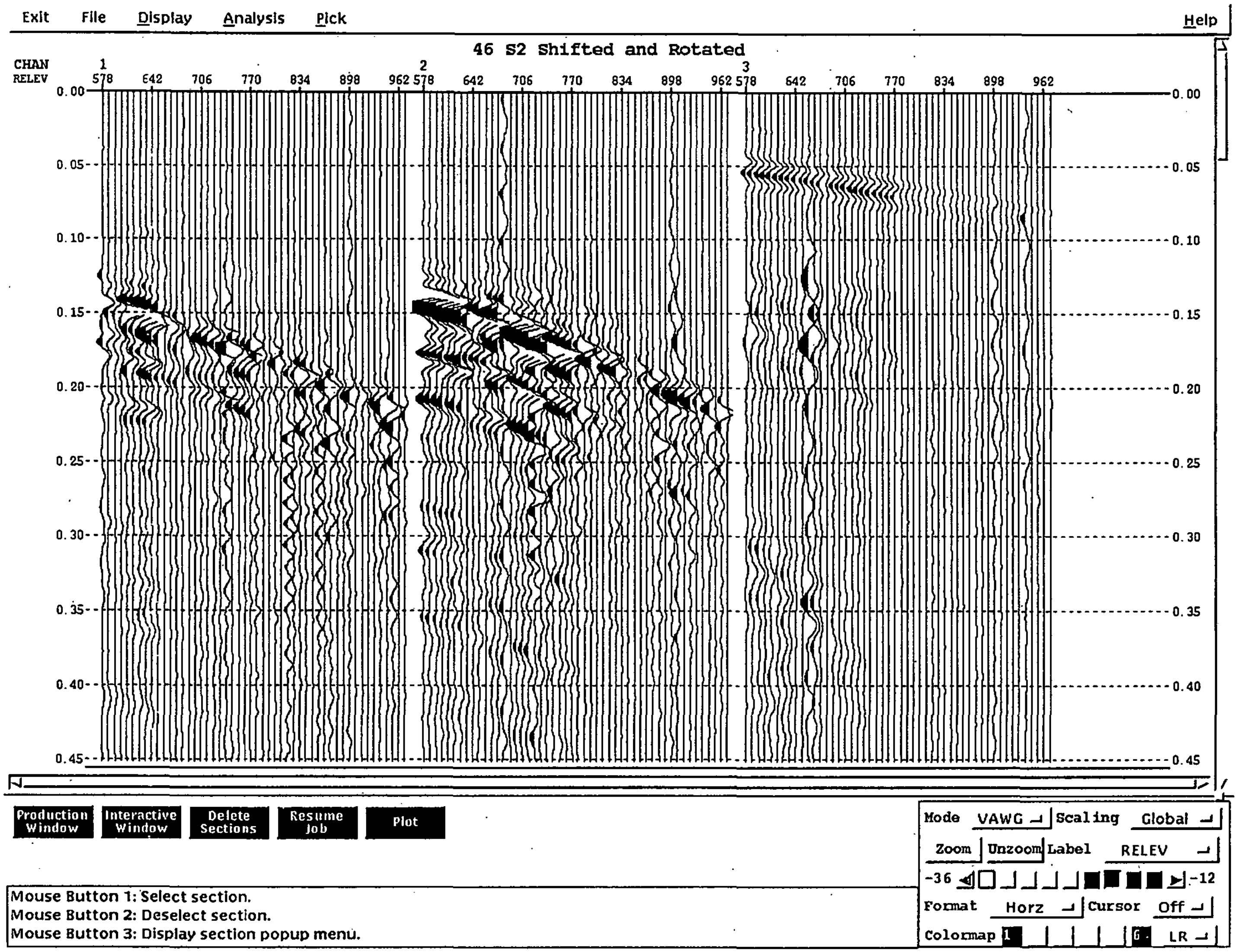
Exit
File
Display
Analysis
Pick
Help
46 S2 Shifted and Rotated
CHAN
RELEV
1
2
3
578
642
706
770
834
898
962
0.00
0.05
0.10
0.15
0.20
0.25
0.30
0.35
0.40
0.45
Production Window
Interactive Window
Delete Sections
Resume Job
Plot
Mouse Button 1: Select section.
Mouse Button 2: Deselect section.
Mouse Button 3: Display section popup menu.
Mode
VAWG
Scaling
Global
Zoom
Unzoom
Label
RELEV
-36
-12
Format
Horz
Cursor
Off
Colormap
LR

Figure A3c.

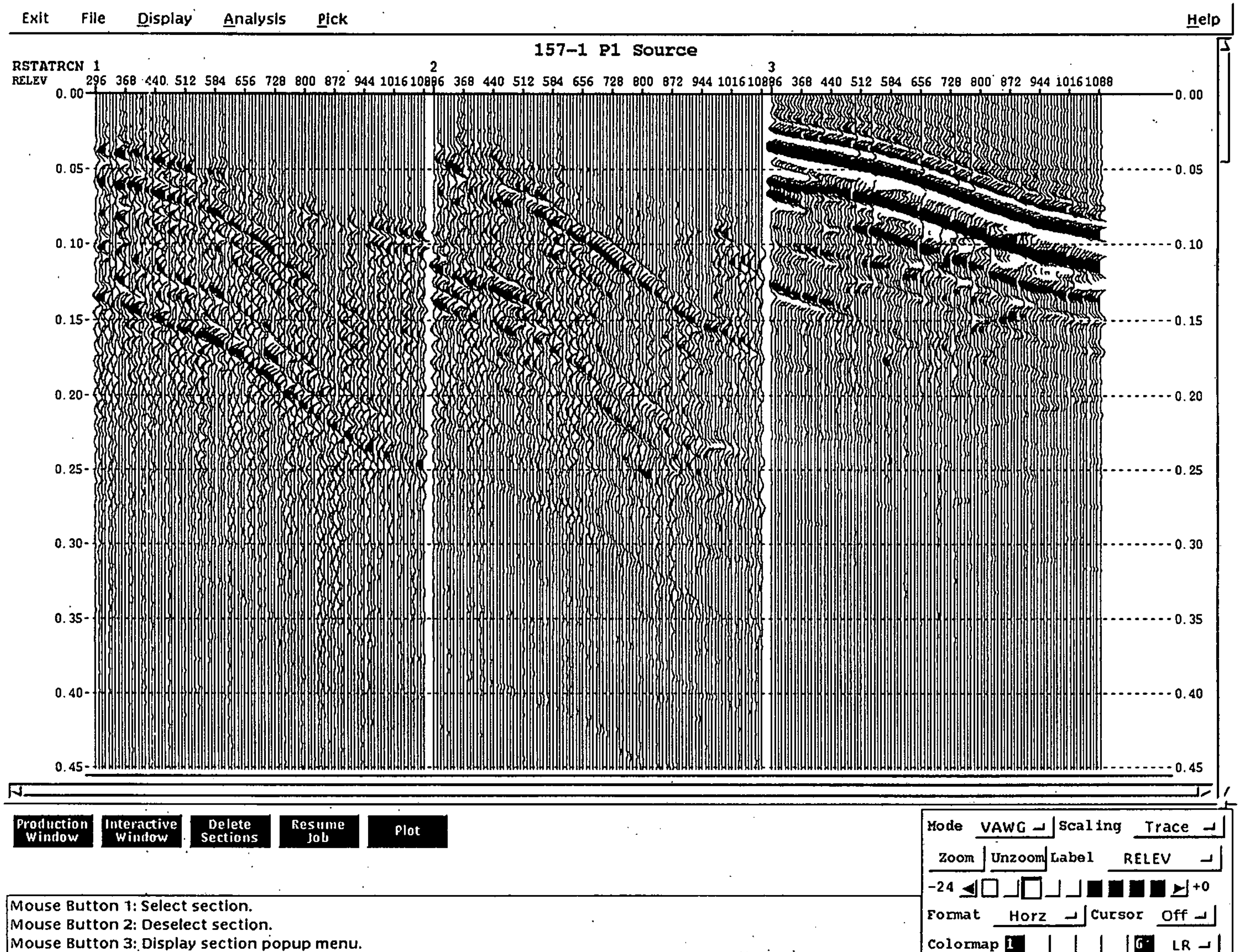

Figure A4a - A4d. Seismograms from Well 157, site 1, 1996 survey. The three panels are geophone components horizontal in-line (left), horizontal cross-line (center), and vertical (right). The traces have been rotated (using P-wave particle motion) and are scaled using the maximum of each trace. A3a is P-wave source at site 1, A3b is S-wave in-line source, A3c is S-wave cross-line. A4d is P-wave source at site 2 (used for rotation …sis … te 1 … a)

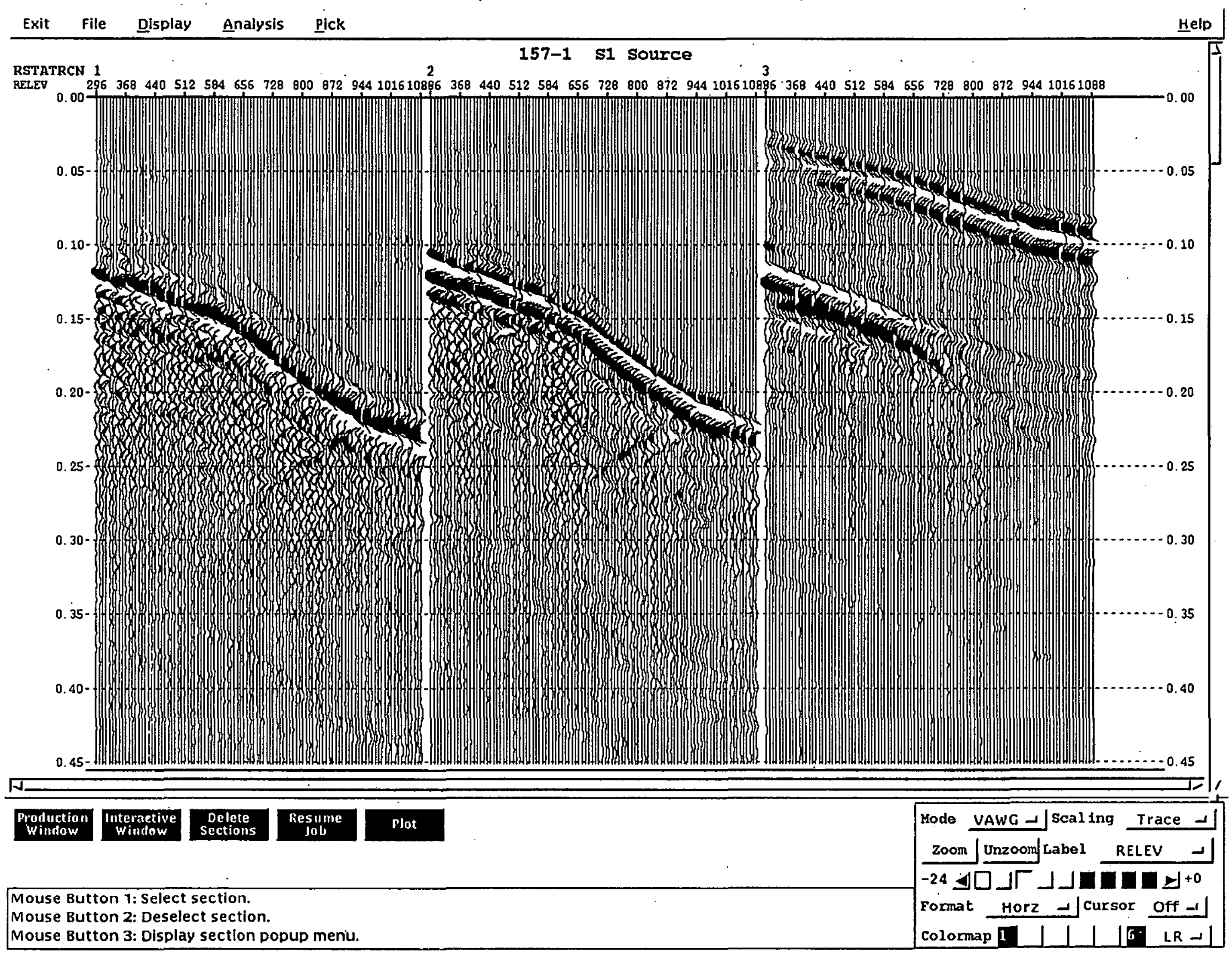
Exit
File
Display
Analysis
Pick
Help
157-1 S1 Source
RSTATRCN
RELEV
Production Window
Interactive Window
Delete Sections
Resume Job
Plot
Mouse Button 1: Select section.
Mouse Button 2: Deselect section.
Mouse Button 3: Display section popup menu.
Mode VAWG
Scaling Trace
Zoom
Unzoom
Label RELEV
Format Horz
Cursor Off
Colormap
LR

Figure A4b

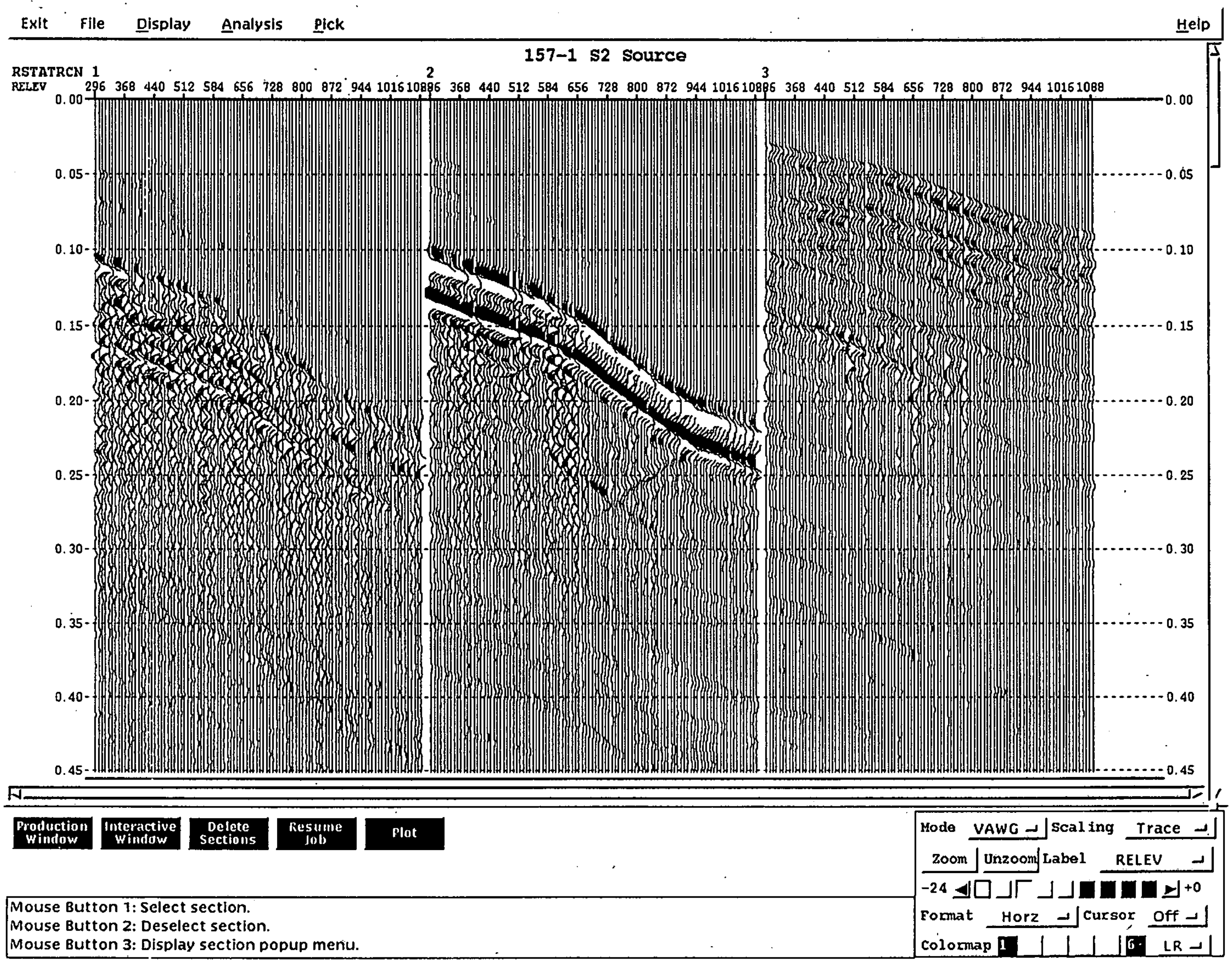
Exit
File
Display
Analysis
Pick
Help
157-1 S2 Source
RSTATRCN 1
2
3
RELEV
296 368 440 512 584 656 728 800 872 944 1016 1088
0.00
0.05
0.10
0.15
0.20
0.25
0.30
0.35
0.40
0.45
Production Window
Interactive Window
Delete Sections
Resume Job
Plot
Mouse Button 1: Select section.
Mouse Button 2: Deselect section.
Mouse Button 3: Display section popup menu.
Mode
VAWG
Scaling
Trace
Zoom
Unzoom
Label
RELEV
-24
+0
Format
Horz
Cursor
Off
Colormap
LR

Figure A4c

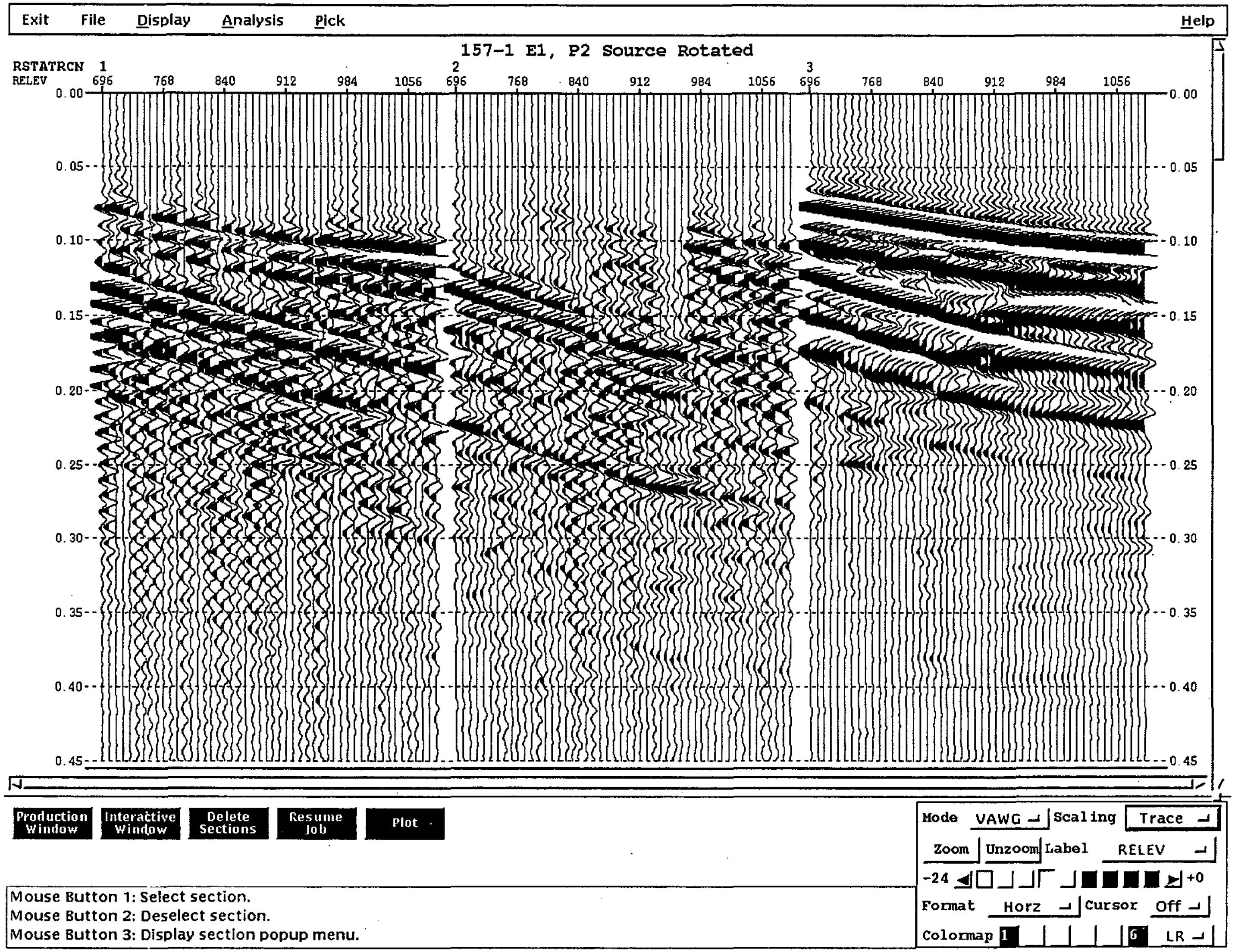
Exit File Display Analysis Pick Help
157-1 E1, P2 Source Rotated
RSTATRCN
RELEV
696 768 840 912 984 1056
0.00 0.05 0.10 0.15 0.20 0.25 0.30 0.35 0.40 0.45
Production Window
Interactive Window
Delete Sections
Resume Job
Plot
Mouse Button 1: Select section.
Mouse Button 2: Deselect section.
Mouse Button 3: Display section popup menu.
Mode VAWG
Scaling Trace
Zoom Unzoom Label RELEV
-24 +0
Format Horz Cursor Off
Colormap LR

Figure A4d

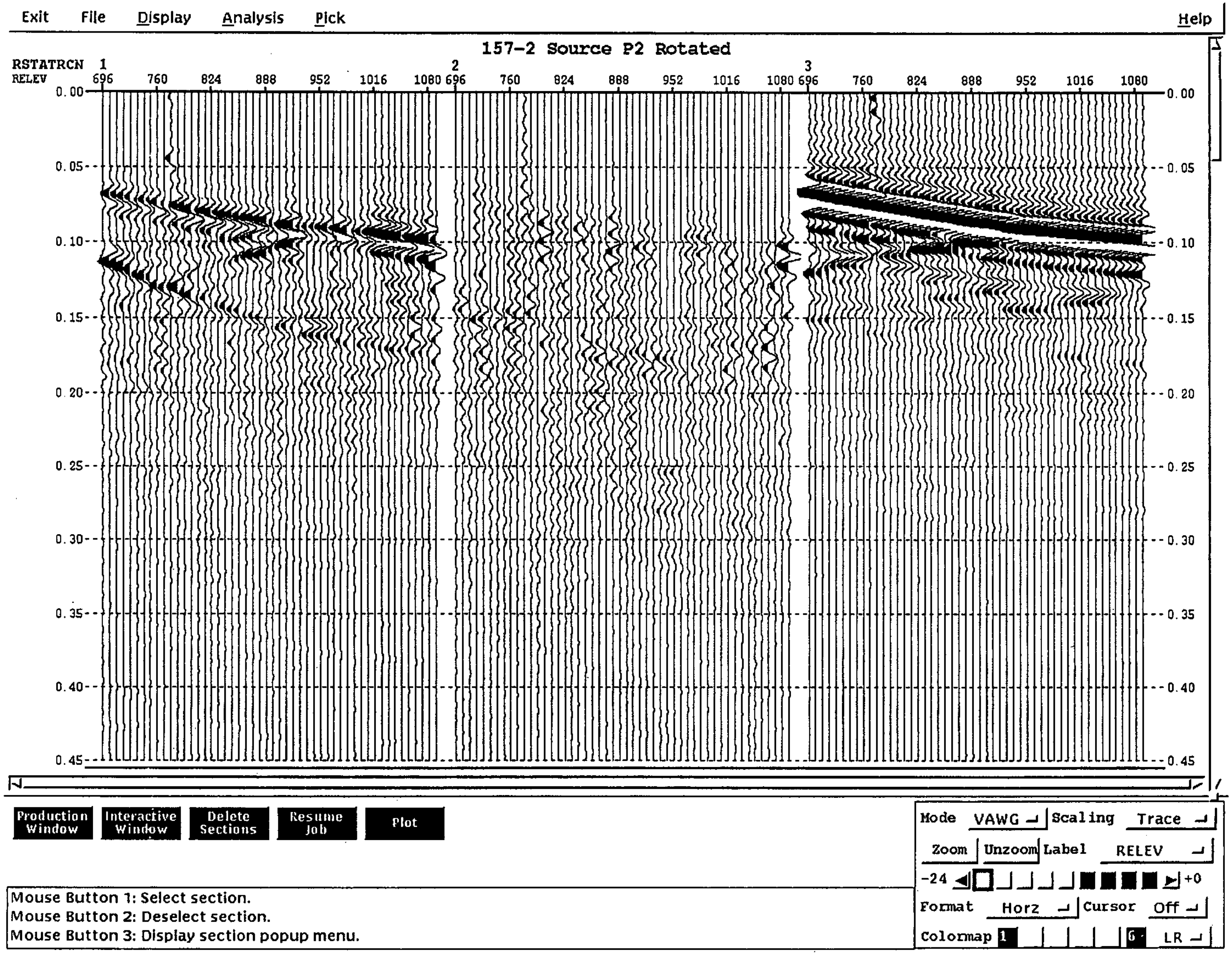

Figure A5a - A5c. Seismograms from Well 157, site 2, 1996 survey. The three panels are geophone components horizontal in-line (left), horizontal cross-line (center), and vertical (right). The traces have been rotated (using P-wave particle motion) and are scaled using the maximum of each trace. 5a - A5c are the P-wave, S-wave in-line, and S-wave cross line respectively.

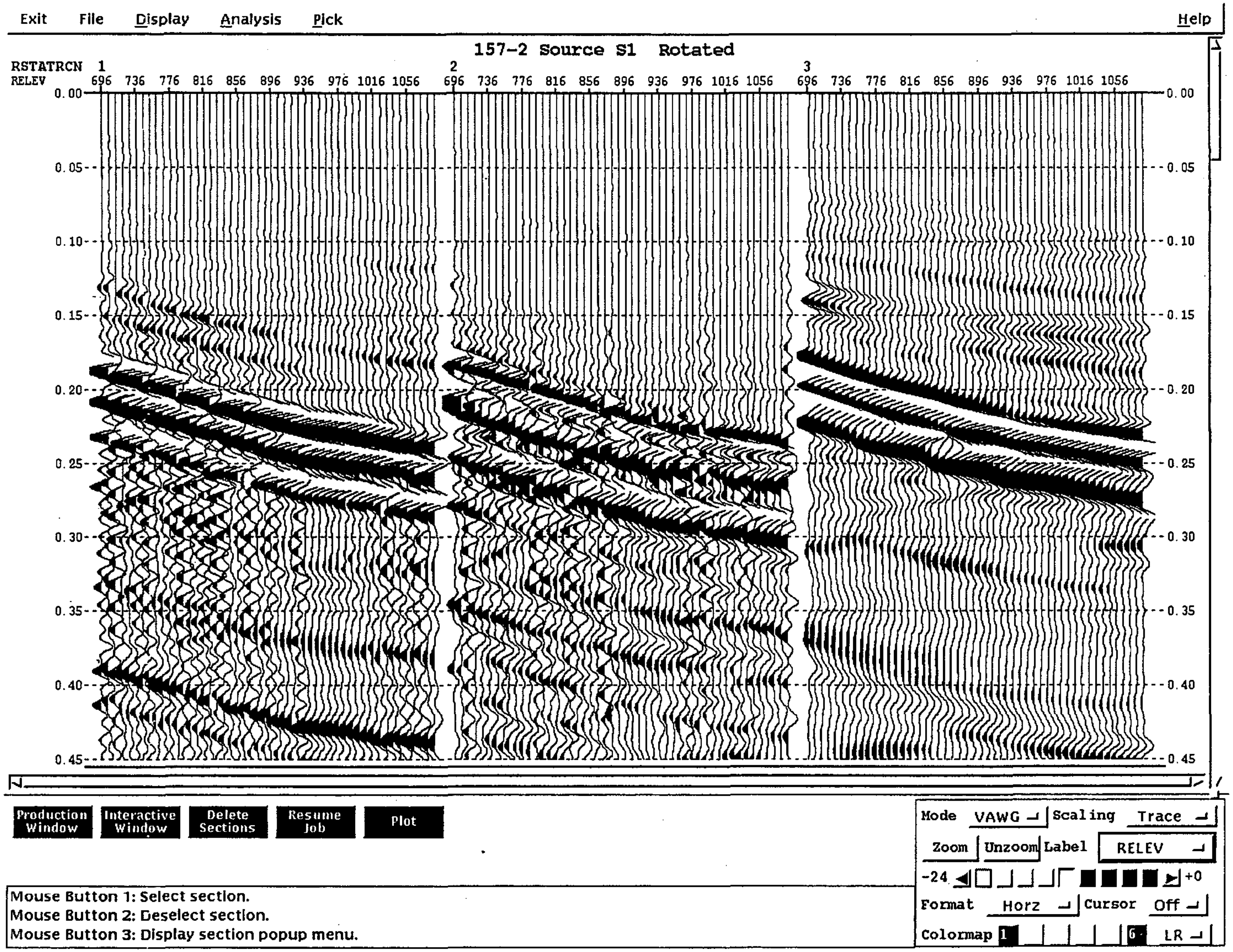
Exit
File
Display
Analysis
Pick
Help
157-2 Source S1 Rotated
RSTATRCN
RELEV
1
2
3
696 736 776 816 856 896 936 976 1016 1056
0.00
0.05
0.10
0.15
0.20
0.25
0.30
0.35
0.40
0.45
Production Window
Interactive Window
Delete Sections
Resume Job
Plot
Mouse Button 1: Select section.
Mouse Button 2: Deselect section.
Mouse Button 3: Display section popup menu.
Mode
VAWG
Scaling
Trace
Zoom
Unzoom
Label
RELEV
-24
+0
Format
Horz
Cursor
Off
Colormap
LR

Figure A5b

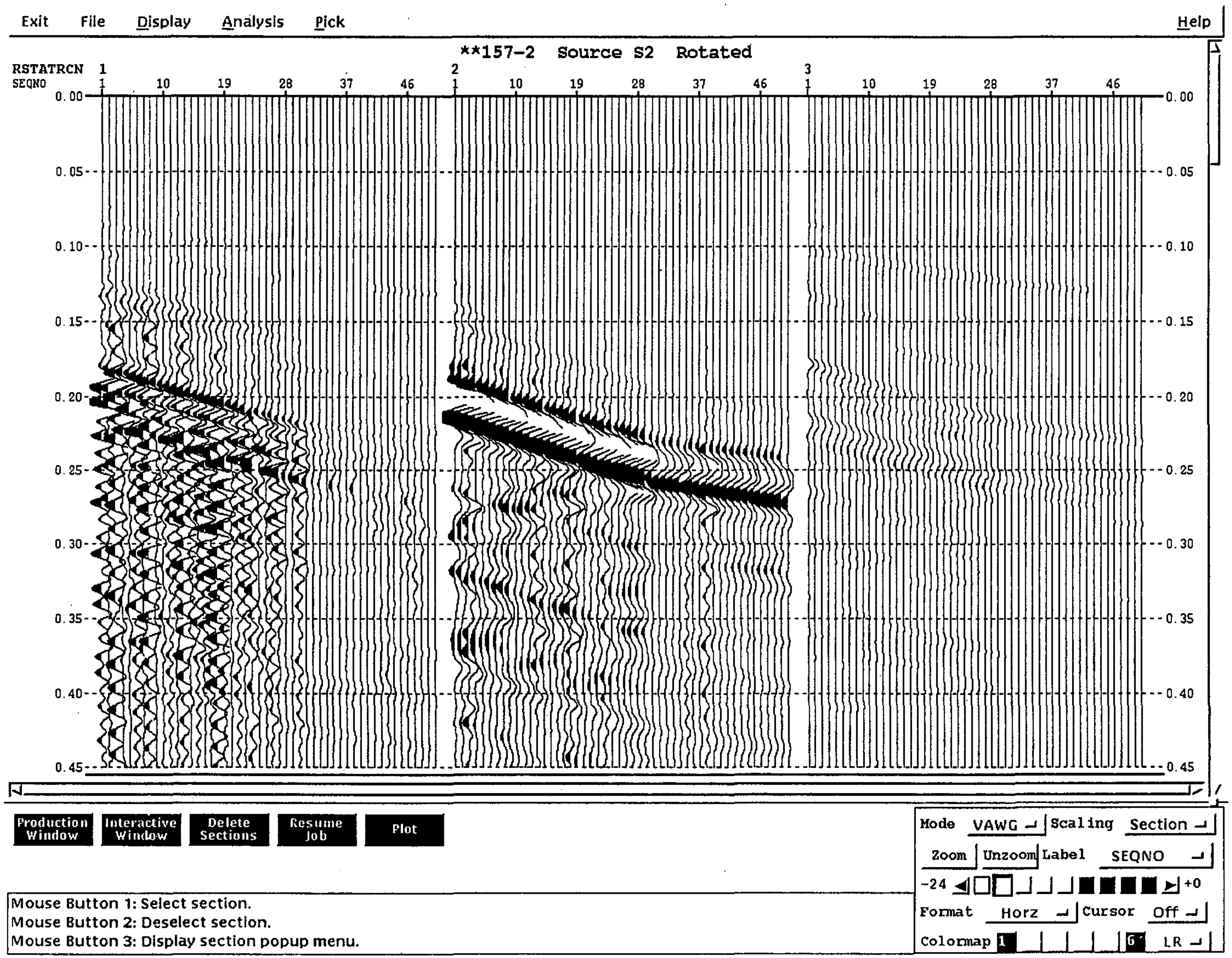

Exit
File
Display
Analysis
Pick
Help
**157-2 Source S2 Rotated
RSTATRCN
SEQNO
0.00
0.05
0.10
0.15
0.20
0.25
0.30
0.35
0.40
0.45
Production Window
Interactive Window
Delete Sections
Resume Job
Plot
Mouse Button 1: Select section.
Mouse Button 2: Deselect section.
Mouse Button 3: Display section popup menu.
Mode VAWG
Scaling Section
Zoom
Unzoom
Label SEQNO
-24
+0
Format Horz
Cursor Off
Colormap
LR

Figure A5c

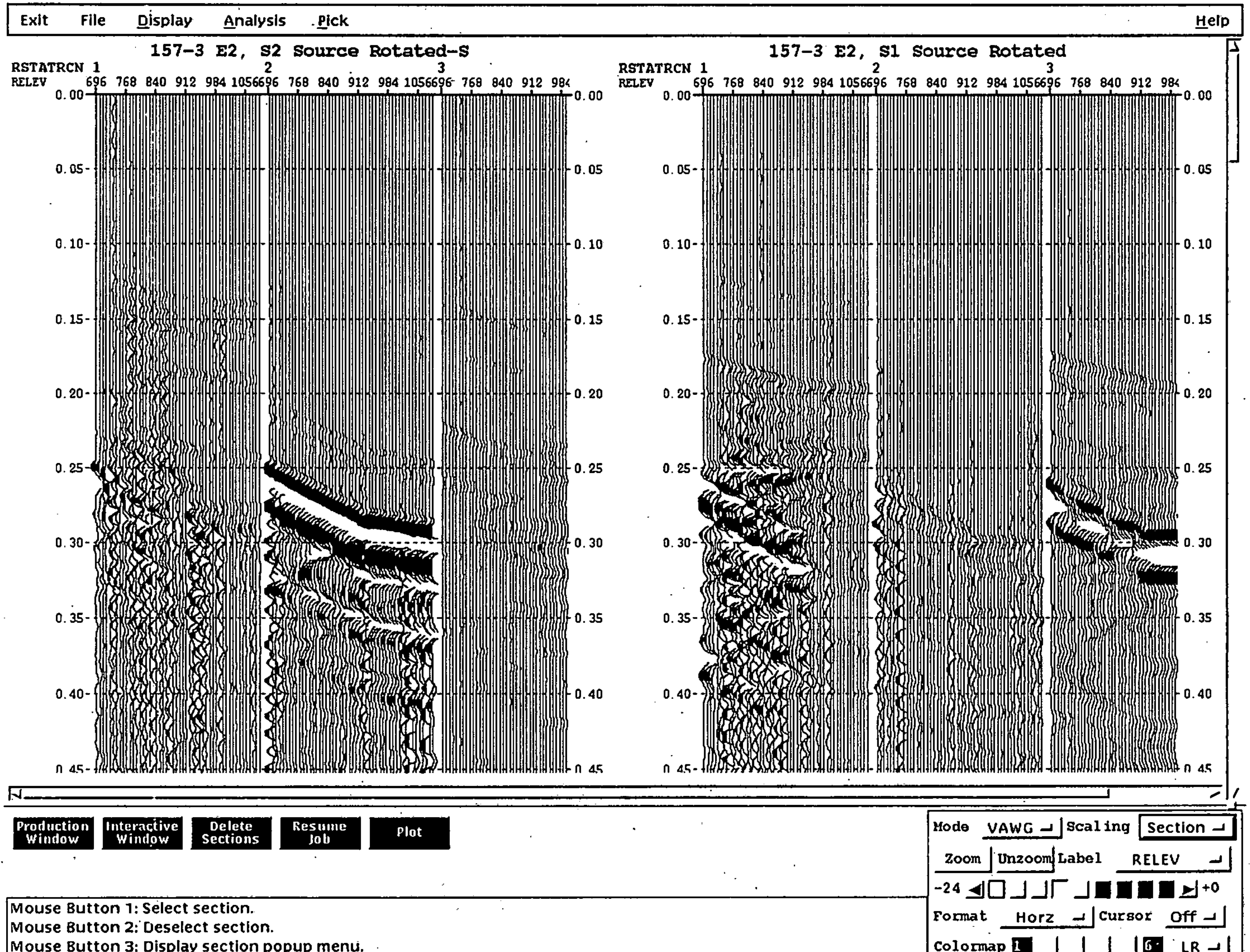

Figure A6. Seismograms from Well 157, site 3, 1996 survey. The three panels are geophone components horizontal in-line (left), horizontal cross-line (center), and vertical (right). The traces have been rotated (using P-wave particle motion). Left panels are S-wave cross-line source, right panels are S-wave cross-line (each scaled to maximum of three components).

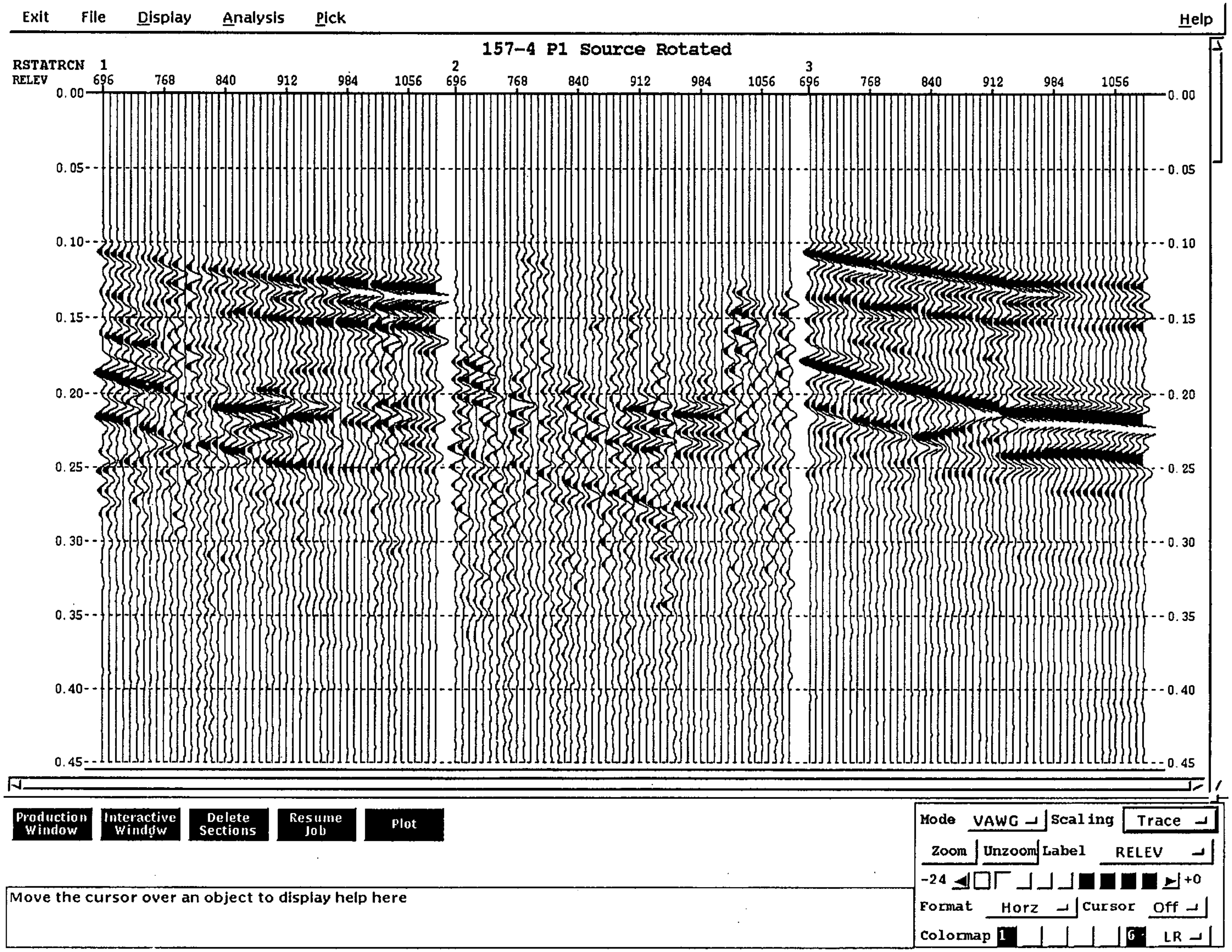

Figure A7a - A7c. Seismograms from Well 157, site 4, 1996 survey. The three panels are geophone components horizontal in-line (left), horizontal cross-line (center), and vertical (right). The traces have been rotated (using P-wave particle motion) and are scaled using the maximum of each trace. A7a - A7c are the P-wave, S-wave in-line, and S-wave c lin pec y.

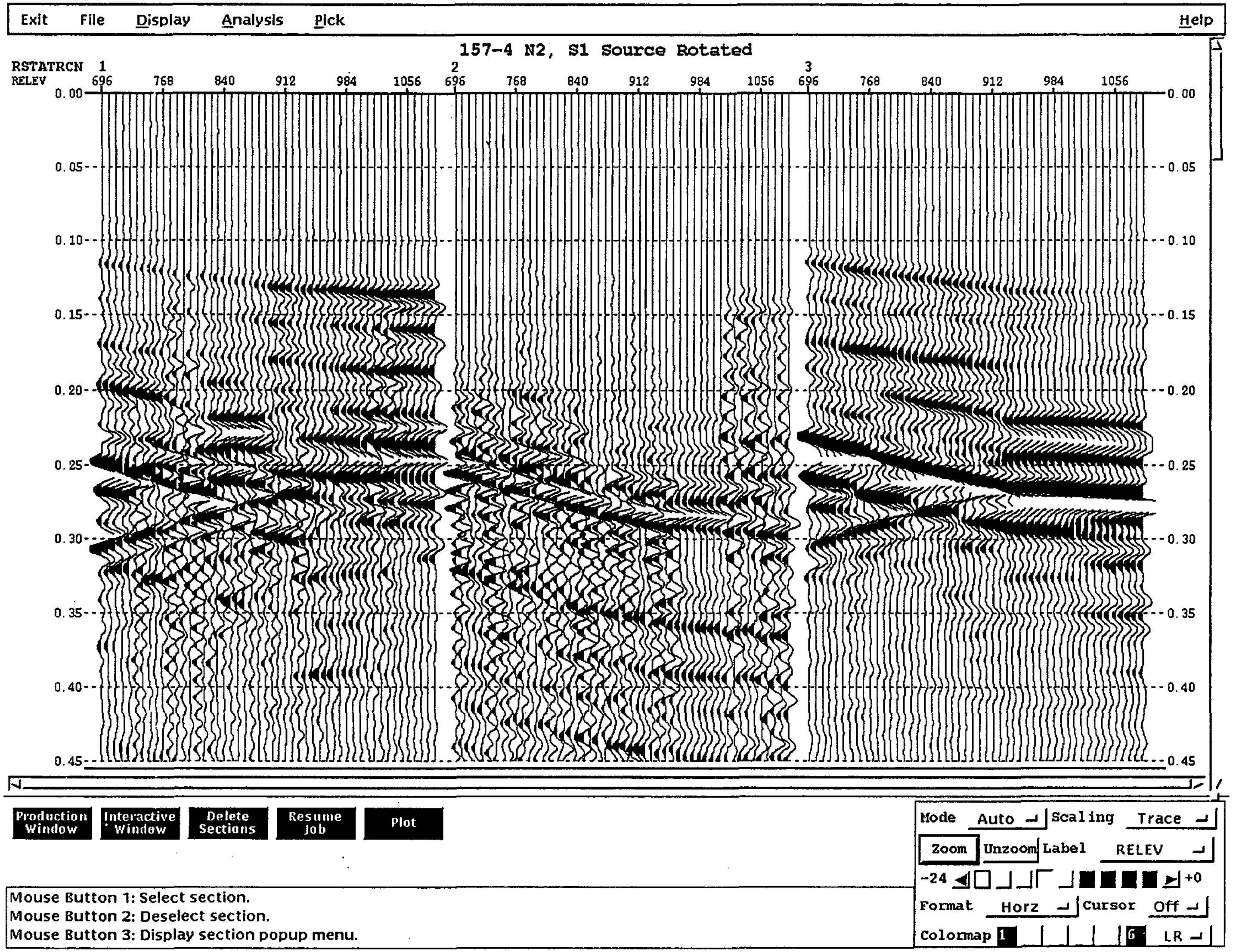

Exit
File
Display
Analysis
Pick
Help
157-4 N2, S1 Source Rotated
RSTATRCN
RELEV
1
2
3
696
768
840
912
984
1056
0.00
0.05
0.10
0.15
0.20
0.25
0.30
0.35
0.40
0.45
Production Window
Interactive Window
Delete Sections
Resume Job
Plot
Mouse Button 1: Select section.
Mouse Button 2: Deselect section.
Mouse Button 3: Display section popup menu.
Mode
Auto
Scaling
Trace
Zoom
Unzoom
Label
RELEV
-24
+0
Format
Horz
Cursor
Off
Colormap
LR

Figure A7b

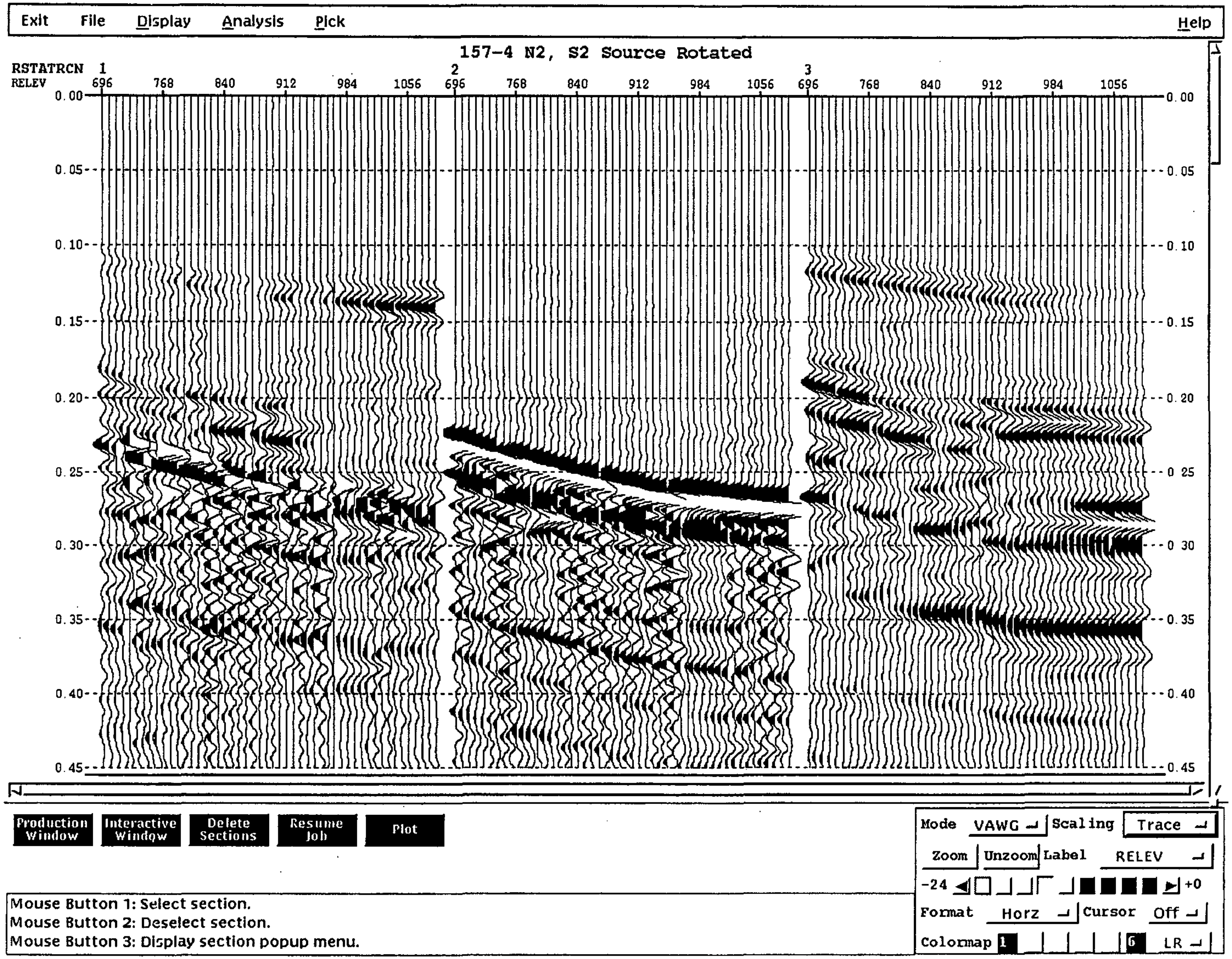
Exit
File
Display
Analysis
Pick
Help
157-4 N2, S2 Source Rotated
RSTATRCN
RELEV
Production Window
Interactive Window
Delete Sections
Resume Job
Plot
Mouse Button 1: Select section.
Mouse Button 2: Deselect section.
Mouse Button 3: Display section popup menu.
Mode VAWG
Scaling Trace
Zoom
Unzoom
Label RELEV
Format Horz
Cursor Off
Colormap
LR

Figure A7c

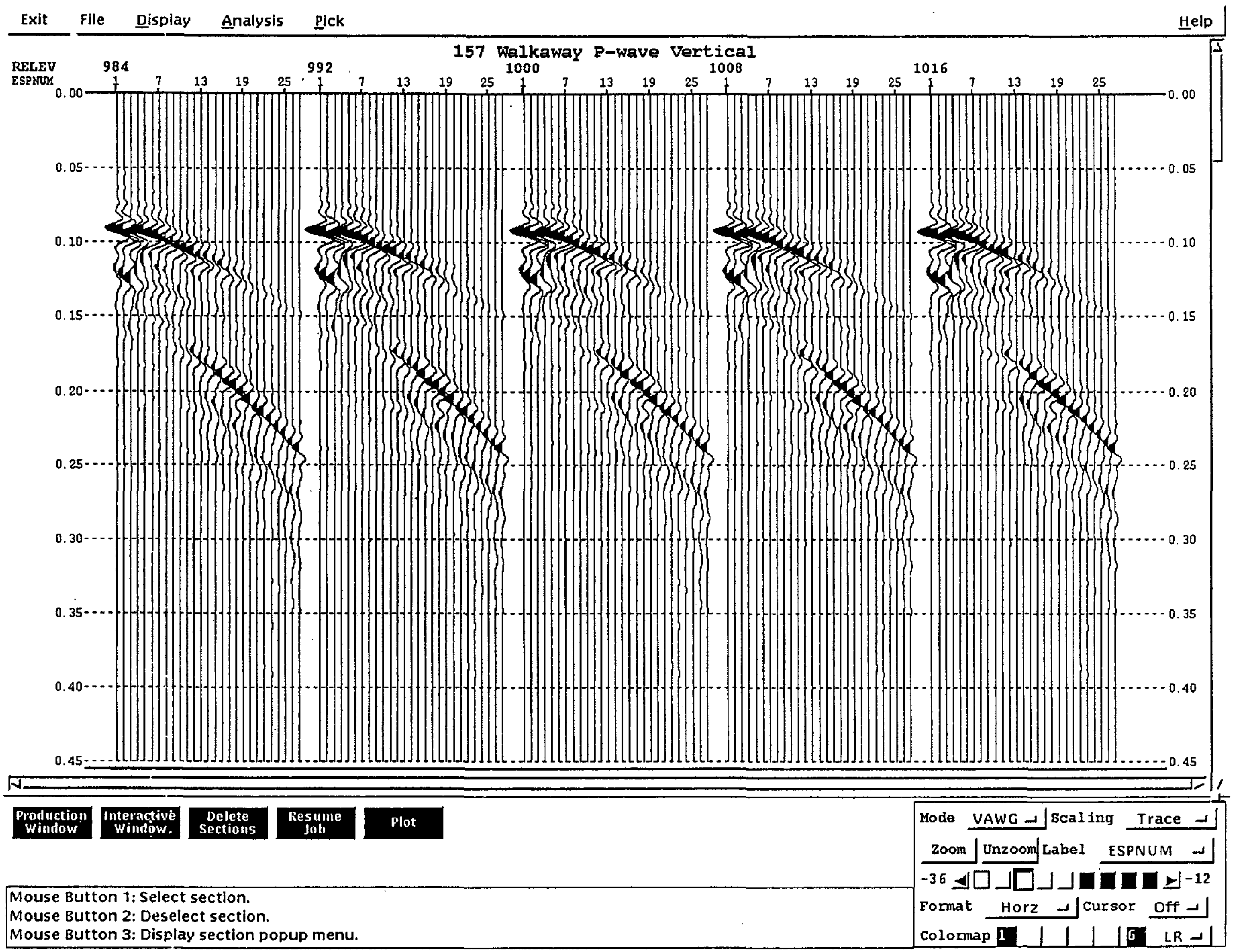

Figure A8a - A8f. Seismograms from Well 157, walkaway, 1996 survey. The 5 panels are geophone depths 984, 992, 1000, 1008 and 1016 ft. left to right. The 27 traces per panel are the 27 offset locations (50 ft. spacint). The traces are scaled to the maximum of each section except where noted. A8a-A8c are P-wave source, geophone components vertical (trace scaling), unrotated horizontal 1 (trace scaling), and unrotated horizontal 2. A8d-A8f are S-wave cross-line source, vertical, unrotated horizontal 1, and unrotated horizontal 2.

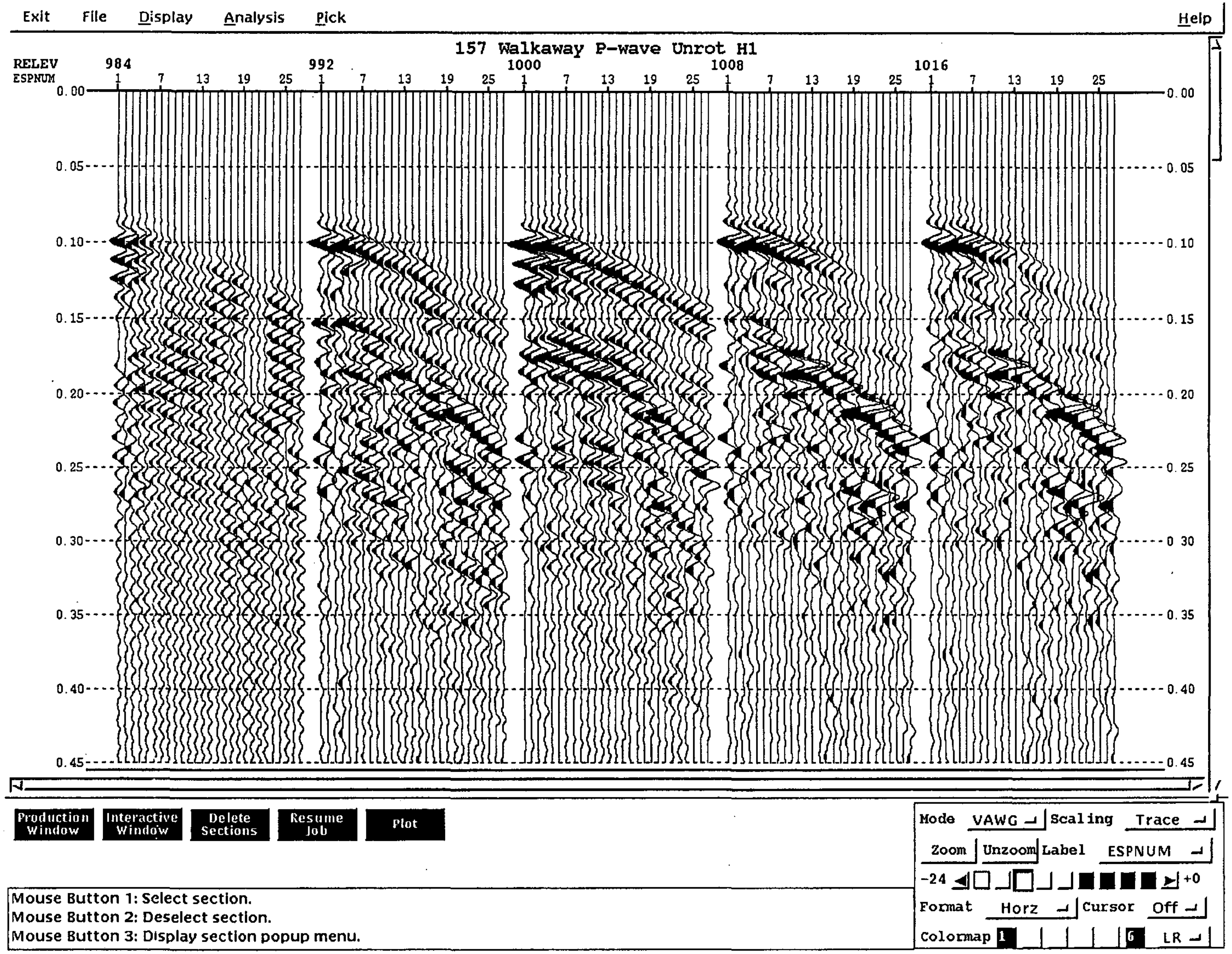

Exit File Display Analysis Pick
Help
157 Walkaway P-wave Unrot H1
RELEV 984 992 1000 1008 1016
ESPNUM 1 7 13 19 25
0.00 0.05 0.10 0.15 0.20 0.25 0.30 0.35 0.40 0.45
Production Window
Interactive Window
Delete Sections
Resume Job
Plot
Mouse Button 1: Select section.
Mouse Button 2: Deselect section.
Mouse Button 3: Display section popup menu.
Mode VAWG
Scaling Trace
Zoom
Unzoom
Label ESPNUM
-24
+0
Format Horz
Cursor Off
Colormap
LR

Figure A8b

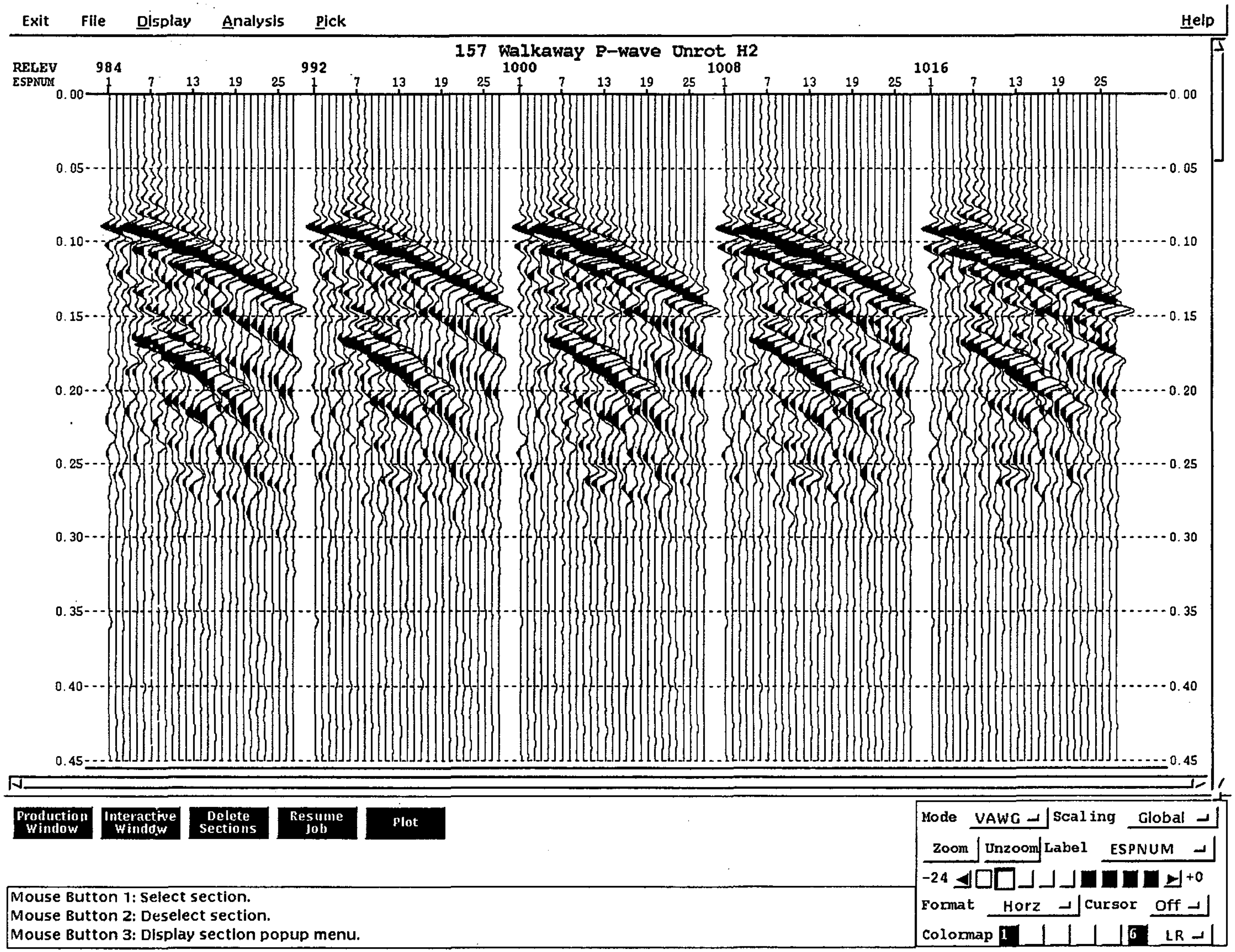
Exit
File
Display
Analysis
Pick
Help
157 Walkaway P-wave Unrot H2
RELEV
ESPNUM
Production Window
Interactive Window
Delete Sections
Resume Job
Plot
Mouse Button 1: Select section.
Mouse Button 2: Deselect section.
Mouse Button 3: Display section popup menu.
Mode VAWG
Scaling Global
Zoom
Unzoom
Label ESPNUM
Format Horz
Cursor Off
Colormap
LR

Figure A8c

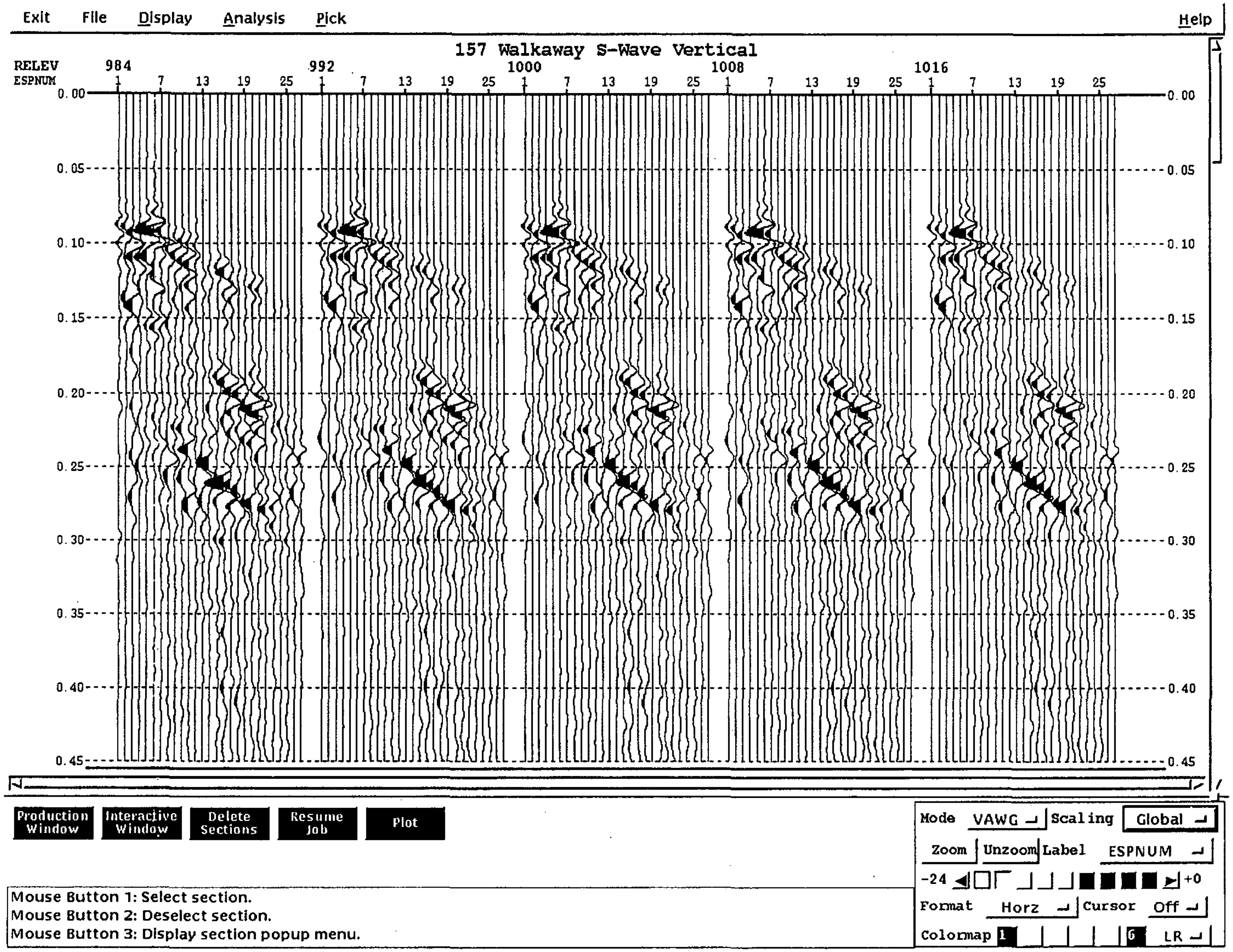

Exit
File
Display
Analysis
Pick
Help
157 Walkaway S-Wave Vertical
RELEV
ESPNUM
984
992
1000
1008
1016
Production Window
Interactive Window
Delete Sections
Resume Job
Plot
Mouse Button 1: Select section.
Mouse Button 2: Deselect section.
Mouse Button 3: Display section popup menu.
Mode VAWG
Scaling Global
Zoom
Unzoom
Label ESPNUM
Format Horz
Cursor Off
Colormap

Figure A8d

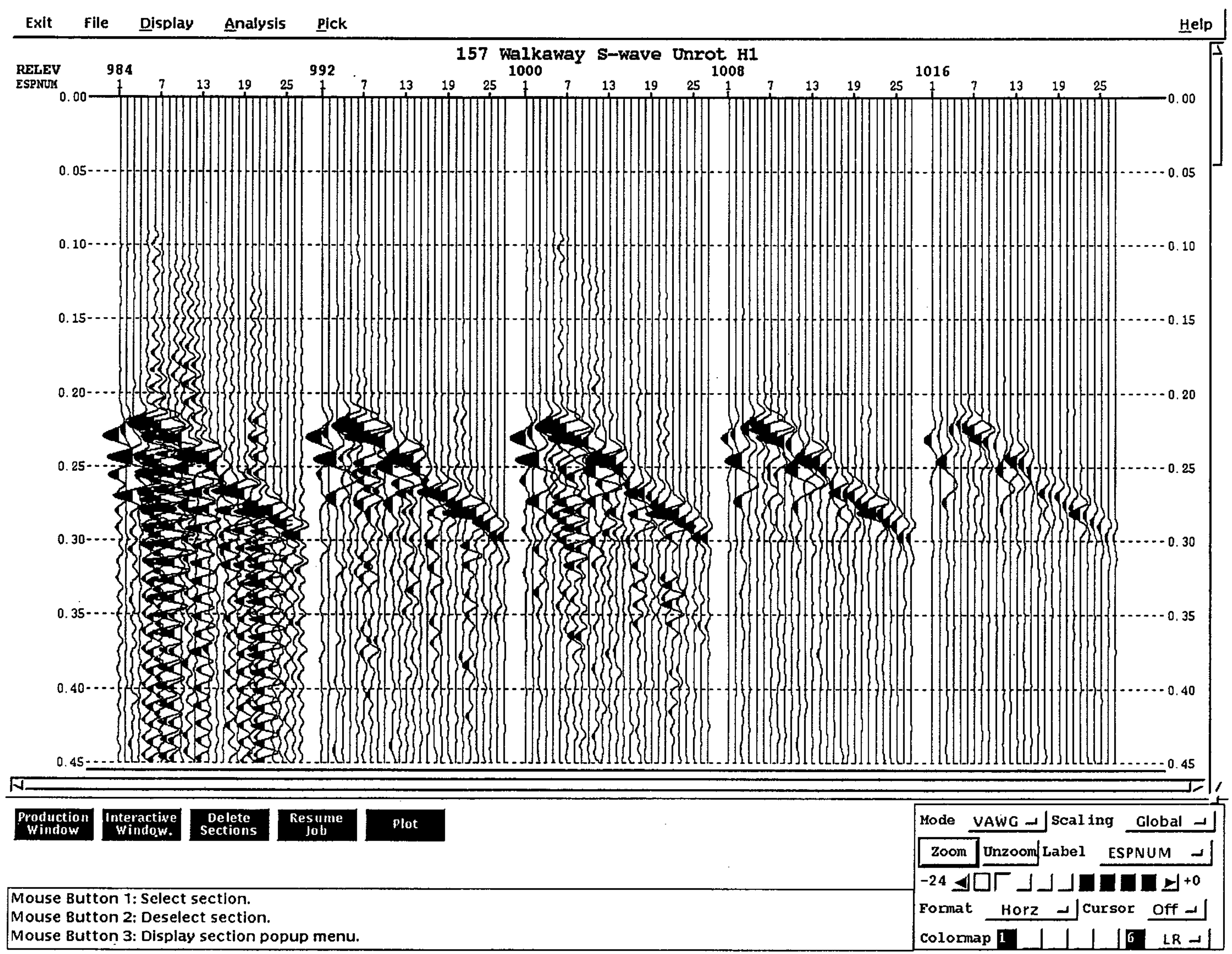

Exit
File
Display
Analysis
Pick
Help
157 Walkaway S-wave Unrot H1
RELEV
ESPNUM
984
992
1000
1008
1016
Production Window
Interactive Window
Delete Sections
Resume Job
Plot
Mouse Button 1: Select section.
Mouse Button 2: Deselect section.
Mouse Button 3: Display section popup menu.
Mode
VAWG
Scaling
Global
Zoom
Unzoom
Label
ESPNUM
-24
+0
Format
Horz
Cursor
Off
Colormap
LR

Figure A8e

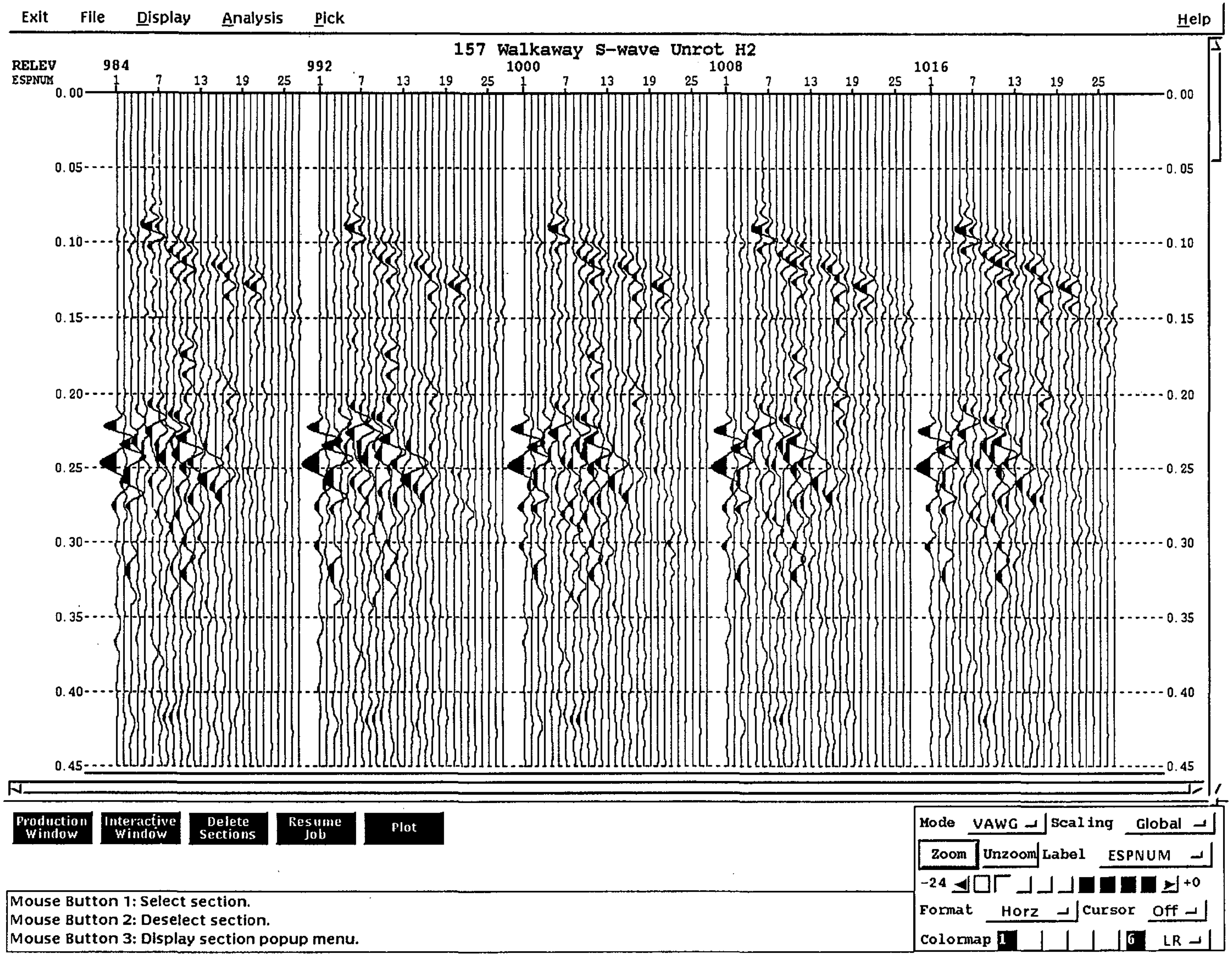

Exit File Display Analysis Pick Help
157 Walkaway S-wave Unrot H2
RELEV
ESPNUM
984 992 1000 1008 1016
Production Window
Interactive Window
Delete Sections
Resume Job
Plot
Mouse Button 1: Select section.
Mouse Button 2: Deselect section.
Mouse Button 3: Display section popup menu.
Mode VAWG Scaling Global
Zoom Unzoom Label ESPNUM
Format Horz Cursor Off
Colormap LR

Figure A8f

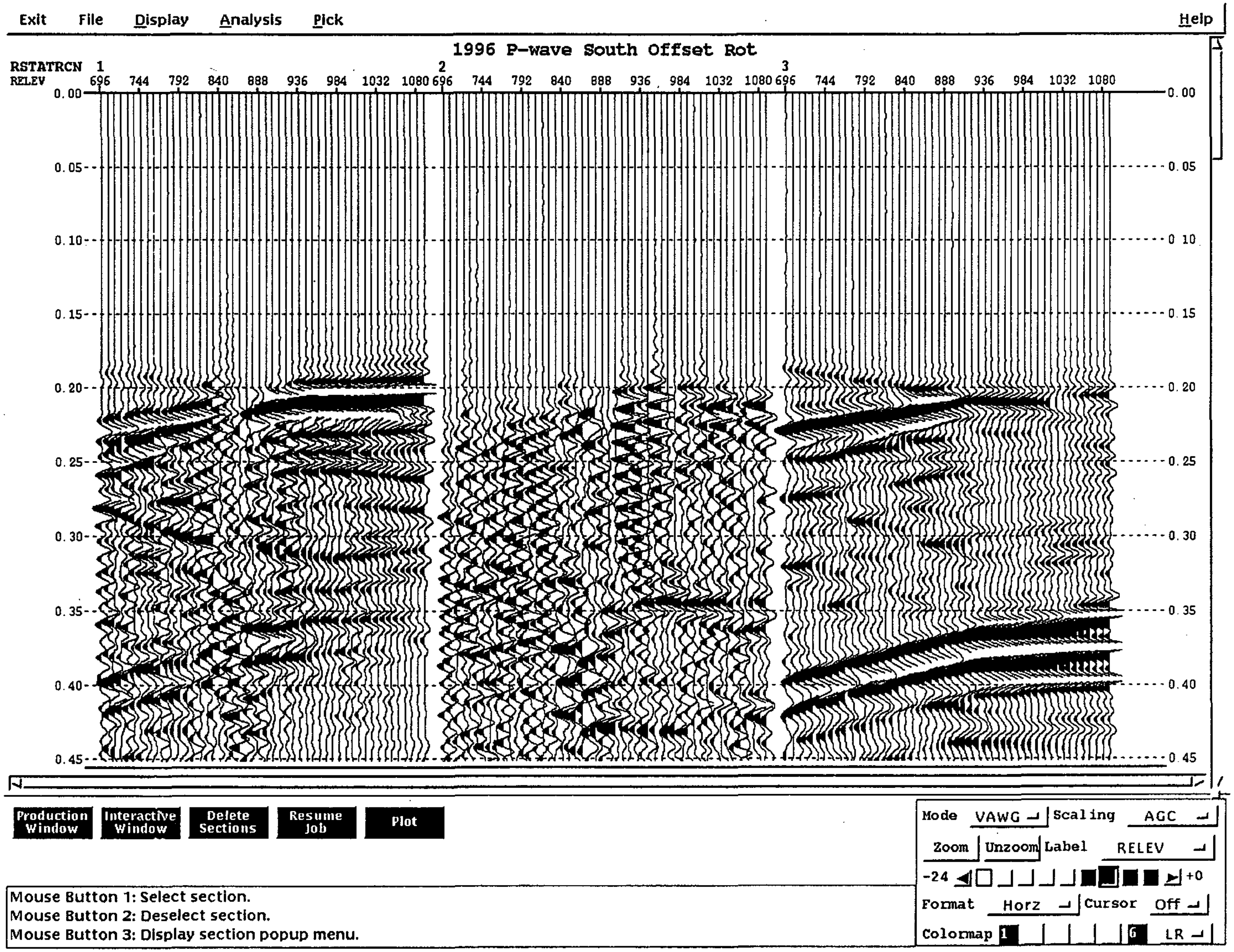

Figure A9. Seismograms from Well 157, site 6 P-wave source, 1996 survey. The three panels are horizontal in-line (left), horizontal cross-line (center) and vertical (right). The traces are normalized to their maximum.

Appendix B: Travel Time, Velocity and Rotation Angle Tables and Plots

LEVEL	1	PHI	83.884	THETA	169.292
LEVEL	2	PHI	83.265	THETA	172.623
LEVEL	3	PHI	82.777	THETA	172.499
LEVEL	4	PHI	81.798	THETA	168.531
LEVEL	5	PHI	77.590	THETA	173.822
LEVEL	6	PHI	82.942	THETA	169.058
LEVEL	7	PHI	79.655	THETA	165.905
LEVEL	8	PHI	79.072	THETA	163.481
LEVEL	9	PHI	76.978	THETA	157.250
LEVEL	10	PHI	72.365	THETA	146.922
LEVEL	11	PHI	74.678	THETA	28.517
LEVEL	12	PHI	74.853	THETA	21.797
LEVEL	13	PHI	74.190	THETA	27.291
LEVEL	14	PHI	67.339	THETA	47.266
LEVEL	15	PHI	67.297	THETA	51.254
LEVEL	16	PHI	80.439	THETA	-67.956
LEVEL	17	PHI	74.928	THETA	-67.035
LEVEL	18	PHI	85.230	THETA	-67.000
LEVEL	19	PHI	74.424	THETA	-65.187
LEVEL	20	PHI	77.410	THETA	-73.702
LEVEL	21	PHI	65.710	THETA	-81.124
LEVEL	22	PHI	70.224	THETA	-82.805
LEVEL	23	PHI	86.530	THETA	-77.368
LEVEL	24	PHI	75.132	THETA	-79.120
LEVEL	25	PHI	66.012	THETA	-81.626
LEVEL	26	PHI	60.459	THETA	-111.368
LEVEL	27	PHI	59.882	THETA	-105.702
LEVEL	28	PHI	54.477	THETA	-114.478
LEVEL	29	PHI	61.152	THETA	-100.904
LEVEL	30	PHI	56.655	THETA	-98.785
LEVEL	31	PHI	69.461	THETA	176.836
LEVEL	32	PHI	68.111	THETA	172.297
LEVEL	33	PHI	72.983	THETA	177.090
LEVEL	34	PHI	73.785	THETA	177.216
LEVEL	35	PHI	58.397	THETA	172.369
LEVEL	36	PHI	55.983	THETA	66.212
LEVEL	37	PHI	56.727	THETA	55.347
LEVEL	38	PHI	58.642	THETA	66.521
LEVEL	39	PHI	60.148	THETA	70.368
LEVEL	40	PHI	59.720	THETA	72.167
LEVEL	41	PHI	64.879	THETA	37.847
LEVEL	42	PHI	60.419	THETA	34.877
LEVEL	43	PHI	61.334	THETA	35.225
LEVEL	44	PHI	49.218	THETA	40.349
LEVEL	45	PHI	31.994	THETA	66.314
LEVEL	46	PHI	49.478	THETA	-63.847
LEVEL	47	PHI	40.938	THETA	-66.519
LEVEL	48	PHI	17.909	THETA	-45.047
LEVEL	49	PHI	43.670	THETA	-68.992
LEVEL	50	PHI	41.448	THETA	-74.853
LEVEL	51	PHI	49.579	THETA	-73.171
LEVEL	52	PHI	50.835	THETA	-75.725
LEVEL	53	PHI	25.643	THETA	-63.492
LEVEL	54	PHI	29.813	THETA	-65.981
LEVEL	55	PHI	41.117	THETA	-75.999
LEVEL	56	PHI	41.406	THETA	-80.176
LEVEL	57	PHI	42.233	THETA	-84.044
LEVEL	58	PHI	22.115	THETA	-85.868
LEVEL	59	PHI	43.642	THETA	-81.016
LEVEL	60	PHI	42.868	THETA	-84.038
LEVEL	61	PHI	45.915	THETA	-87.946
LEVEL	62	PHI	42.864	THETA	-91.760
LEVEL	63	PHI	35.384	THETA	-92.476
LEVEL	64	PHI	52.489	THETA	-86.485
LEVEL	65	PHI	45.308	THETA	-88.702
LEVEL	66	PHI	50.614	THETA	-84.830
LEVEL	67	PHI	45.674	THETA	-90.606
LEVEL	68	PHI	28.827	THETA	-97.617
LEVEL	69	PHI	42.415	THETA	-91.058
LEVEL	70	PHI	38.164	THETA	-91.034
LEVEL	71	PHI	49.189	THETA	-65.012
LEVEL	72	PHI	47.222	THETA	-68.429
LEVEL	73	PHI	28.458	THETA	-57.748
LEVEL	74	PHI	35.525	THETA	-67.851
LEVEL	75	PHI	28.476	THETA	-70.822
LEVEL	76	PHI	34.920	THETA	-56.124
LEVEL	77	PHI	48.162	THETA	-61.198
LEVEL	78	PHI	41.032	THETA	-46.299
LEVEL	79	PHI	61.576	THETA	-62.192
LEVEL	80	PHI	49.926	THETA	-68.968
LEVEL	81	PHI	35.800	THETA	-73.234
LEVEL	82	PHI	36.149	THETA	-76.490
LEVEL	83	PHI	26.167	THETA	-69.704
LEVEL	84	PHI	44.041	THETA	-74.052
LEVEL	85	PHI	26.613	THETA	-74.397
LEVEL	86	PHI	56.263	THETA	167.182
LEVEL	87	PHI	47.593	THETA	168.232
LEVEL	88	PHI	61.034	THETA	168.472
LEVEL	89	PHI	45.664	THETA	168.012
LEVEL	90	PHI	34.217	THETA	152.798
LEVEL	91	PHI	41.975	THETA	-43.757
LEVEL	92	PHI	46.847	THETA	-50.513
LEVEL	93	PHI	37.994	THETA	-22.750
LEVEL	94	PHI	46.063	THETA	-39.024
LEVEL	95	PHI	54.377	THETA	-62.079
LEVEL	96	PHI	51.934	THETA	-39.343
LEVEL	97	PHI	56.058	THETA	-47.406
LEVEL	98	PHI	47.659	THETA	-18.103
LEVEL	99	PHI	53.478	THETA	-32.279
LEVEL	100	PHI	54.463	THETA	-52.078

Figure B1. Rotation angles for 1996 site 1.

Depth(ft)	P	S1	S2	S2tim1
296	34.243530	119.006233	110.734299	100.201057
304	34.712791	119.705803	111.634079	100.079041
312	35.392941	120.115822	112.364594	101.962952
320	35.864471	120.431213	112.937149	103.455040
328	36.360809	121.735313	113.968613	103.086304
336	37.016701	123.708450	115.141823	103.500000
344	37.351009	124.654533	116.197197	104.500000
352	37.809921	124.415680	116.196777	105.500000
360	38.278141	124.889603	116.774208	106.000000
368	38.704559	124.667084	118.048241	105.963997
376	39.195580	124.384041	118.072067	107.500000
384	39.456600	124.641800	118.758469	109.620331
392	39.944859	125.799263	119.658127	109.931519
400	40.410782	126.613228	120.147186	110.778831
408	40.854019	127.923843	122.279739	112.024773
416	41.373211	127.856323	121.875092	112.842690
424	41.548771	128.622787	122.667236	113.492050
432	41.845779	129.050201	123.162331	114.551941
440	42.122330	129.138046	123.821877	114.853668
448	42.686779	130.044891	124.625664	115.953011
456	43.341370	132.435593	125.799057	116.389511
464	43.879440	134.140961	126.772858	117.427856
472	44.363621	135.843216	127.760223	118.302353
480	44.712940	136.861145	128.428177	119.095032
488	45.066570	136.758743	129.124176	119.770851
496	45.626499	138.775925	130.034393	121.601677
504	46.072121	138.662354	130.361145	121.986504
512	46.491501	140.742157	130.901505	123.662079
520	46.975842	140.611252	132.168198	123.223328
528	47.316231	142.172043	133.227264	124.297737
536	47.790260	141.417038	133.345718	123.529861
544	48.186111	143.242020	134.208099	124.521812
552	48.789230	143.410843	134.934921	125.759399
560	49.321819	143.943802	135.635345	126.578133
568	50.047230	144.539337	136.747864	127.339233
576	50.782471	143.913849	138.683762	129.977219
584	51.088551	145.690582	140.153366	131.189270
592	51.511452	145.559204	140.425079	131.531784
600	52.012821	146.821411	141.364487	132.232330
608	52.733559	149.521179	144.652786	134.817276
616	53.474548	149.434769	145.030945	133.778107
624	54.074749	151.787323	146.037262	136.527954
632	54.800690	151.526062	147.101776	137.510208
640	55.480610	153.354584	148.354507	139.115570
648	56.238220	156.234222	150.375275	140.475266
656	57.087490	156.694977	150.183350	141.444824
664	57.727089	159.355362	152.024979	142.572113
672	58.240028	160.740021	152.876190	144.022476
680	59.110809	161.590775	154.934799	145.709915
688	59.958099	162.757965	156.669952	147.547470
696	60.779610	165.748611	158.755936	149.406921
704	61.439129	168.165131	160.574753	151.119705
712	62.176399	168.978714	162.532288	152.968903
720	63.038029	170.644745	164.465271	154.906418
728	63.984081	172.808609	166.136551	156.806076
736	65.034142	174.288605	168.860397	158.697830
744	65.834061	178.160095	170.308121	160.734955
752	66.543823	179.368607	171.868851	162.177063
760	67.367828	181.359207	173.327957	163.758469
768	68.182159	182.256851	175.022888	165.501999
776	69.117889	184.711273	176.272934	166.800659
784	69.966713	185.725952	177.975876	168.823685
792	70.683823	188.229416	180.315216	170.627991
800	71.433563	190.076126	181.698883	171.987549
808	72.119133	190.598618	183.255035	173.470078
816	73.271698	193.050446	184.856918	175.196411
824	74.084908	194.171326	186.394379	177.246231
832	74.920418	196.026321	189.149445	179.044022
840	75.626907	198.643845	190.317581	180.444946
848	76.214813	199.087051	191.702072	181.883011
856	76.783684	199.225723	193.264847	183.896057
864	77.625107	200.785355	194.978699	185.191544
872	78.597267	202.344559	195.884476	186.570892
880	79.619743	202.973602	197.856216	188.166016
888	80.430779	204.184006	199.442673	189.691040
896	81.141747	206.464981	201.088577	190.886093
904	81.548927	207.796143	203.202164	192.238251
912	81.976883	208.949661	203.752411	193.768997
920	82.619438	209.547440	204.709106	195.435379
928	83.653877	211.561096	205.734756	196.578659
936	84.989647	212.976318	207.559860	198.690689
944	85.519402	215.752808	209.619675	199.332474
952	85.831291	216.725861	210.167404	200.044296
960	86.135567	216.947433	211.186493	200.809113
968	86.390182	216.510696	211.647995	201.301727
976	86.562363	219.220596	212.209579	201.277817
984	87.575020	221.052475	213.117416	201.704742
992	88.002419	220.601669	213.830414	203.355240
1000	88.333023	221.692474	214.808517	203.552963
1008	88.863724	220.904404	215.837204	204.951935
1016	89.363647	220.815872	216.172653	206.287842
1024	89.901817	221.637817	217.297150	207.293793
1032	90.316208	223.783768	218.279297	207.699112
1040	90.713150	223.362854	219.208893	208.801514
1048	91.141541	222.818573	220.496109	209.551941
1056	91.649277	224.958038	220.551468	210.218033
1064	91.960243	225.545212	221.738800	211.239578
1072	92.350548	227.763336	222.410065	211.674271
1080	92.776909	227.457886	223.231033	212.900558
1088	93.314301	226.911484	224.042007	213.590195

Figure B2. Travel times for 1996 site 1 without low pass filter.

296	34.992741
304	35.342640
312	35.836800
320	36.219971
328	36.542309
336	37.009010
344	37.278412
352	37.529041
360	37.786831
368	38.047371
376	38.181679
384	38.349899
392	38.590069
400	38.865990
408	39.192390
416	39.679642
424	39.798672
432	40.049541
440	40.326698
448	40.884819
456	41.509621
464	41.995701
472	42.513741
480	42.861118
488	43.316010
496	44.099991
504	44.391060
512	44.899910
520	45.363079
528	45.760811
536	46.246101
544	46.455650
552	46.867500
560	47.207150
568	47.775108
576	48.534580
584	48.836510
592	49.276340
600	49.830730
608	50.724812
616	51.335751
624	52.135429
632	52.848919
640	53.469849
648	54.157631
656	55.072739
664	55.524940
672	56.031361
680	56.775970
688	57.610630
696	58.316761
704	59.084301
712	59.895309
720	60.780392
728	61.736511
736	62.934090
744	63.609890
752	64.345123
760	65.131233
768	65.893997
776	66.968063
784	67.482758
792	68.243408
800	69.054764
808	69.851631
816	70.925110
824	71.857681
832	72.788422
840	73.631210
848	74.451897
856	74.942802
864	75.580254
872	76.167969
880	76.708191
888	77.325256
896	78.071518
904	78.542900
912	79.221809
920	80.178543
928	81.469543
936	82.785439
944	83.164330
952	83.472641
960	83.751060
968	84.047432
976	84.116219
984	85.121834
992	85.525513
1000	85.848137
1008	86.374161
1016	87.068222
1024	87.580963
1032	88.039948
1040	88.483467
1048	88.942459
1056	89.645889
1064	89.806953
1072	90.187431
1080	90.606918
1088	91.109512

Figure B3. Travel times for 1996 site 1 with low pass filter.

DEPTH	P_VELOCITY	SV_VELOCITY	SH_VELOCITY
296.	9115.	2819.	2623.
304.	9210.	2864.	2671.
312.	9248.	2913.	2725.
320.	9340.	2966.	2781.
328.	9423.	3006.	2814.
336.	9463.	3042.	2832.
344.	9584.	3081.	2872.
352.	9671.	3147.	2939.
360.	9754.	3197.	2990.
368.	9846.	3228.	3057.
376.	9920.	3293.	3126.
384.	10050.	3339.	3182.
392.	10122.	3379.	3214.
400.	10197.	3430.	3255.
408.	10277.	3433.	3282.
416.	10336.	3509.	3345.
424.	10479.	3549.	3385.
432.	10591.	3598.	3434.
440.	10707.	3642.	3492.
448.	10748.	3681.	3528.
456.	10766.	3709.	3523.
464.	10812.	3742.	3537.
472.	10871.	3775.	3550.
480.	10961.	3816.	3581.
488.	11049.	3856.	3641.
496.	11085.	3890.	3645.
504.	11148.	3940.	3704.
512.	11217.	3984.	3705.
520.	11268.	4005.	3765.
528.	11353.	4032.	3779.
536.	11405.	4088.	3854.
544.	11475.	4120.	3860.
552.	11494.	4156.	3910.
560.	11530.	4193.	3951.
568.	11520.	4216.	3989.
576.	11509.	4214.	4061.
584.	11594.	4226.	4066.
592.	11652.	4274.	4124.
600.	11692.	4302.	4142.
608.	11682.	4259.	4120.
616.	11667.	4302.	4175.
624.	11684.	4326.	4162.
632.	11673.	4349.	4222.
640.	11673.	4365.	4223.
648.	11656.	4359.	4196.
656.	11621.	4417.	4234.
664.	11630.	4416.	4213.
672.	11663.	4443.	4226.
680.	11625.	4435.	4253.
688.	11593.	4437.	4271.
696.	11566.	4428.	4241.
704.	11571.	4427.	4228.
712.	11561.	4423.	4254.
720.	11529.	4419.	4259.
728.	11483.	4422.	4252.
736.	11419.	4398.	4261.
744.	11401.	4407.	4213.
752.	11398.	4413.	4229.
760.	11377.	4422.	4226.
768.	11357.	4424.	4249.
776.	11318.	4438.	4235.
784.	11294.	4440.	4255.
792.	11292.	4426.	4240.
800.	11285.	4436.	4241.
808.	11287.	4442.	4271.
816.	11218.	4447.	4258.
824.	11202.	4453.	4274.
832.	11183.	4430.	4274.
840.	11184.	4444.	4258.
848.	11202.	4454.	4288.
856.	11223.	4459.	4325.
864.	11203.	4460.	4331.
872.	11166.	4480.	4337.
880.	11122.	4476.	4363.
888.	11109.	4480.	4376.
896.	11110.	4483.	4366.
904.	11152.	4475.	4376.
912.	11190.	4502.	4390.
920.	11200.	4520.	4416.
928.	11156.	4536.	4411.
936.	11075.	4535.	4419.
944.	11099.	4528.	4399.
952.	11151.	4554.	4416.
960.	11204.	4570.	4449.
968.	11263.	4597.	4494.
976.	11333.	4623.	4475.
984.	11293.	4640.	4474.
992.	11328.	4662.	4519.
1000.	11376.	4678.	4533.
1008.	11398.	4693.	4585.
1016.	11423.	4722.	4623.
1024.	11443.	4734.	4642.
1032.	11479.	4750.	4633.
1040.	11517.	4766.	4677.
1048.	11550.	4774.	4724.
1056.	11573.	4809.	4715.
1064.	11620.	4819.	4738.
1072.	11657.	4840.	4727.
1080.	11690.	4858.	4768.
1088.	11708.	4876.	4815.

Figure B4. Average velocities for 1996 site 1.

DEPTH	P_VELOCITY	Deth_sv	SV_VELOCITY	Depth_sh	SH_VELOCITY
336.	15488.	336.	10452.	336.	14262.
344.	16198.	344.	10786.	344.	15568.
352.	16911.	352.	10554.	352.	13544.
360.	16960.	360.	10694.	360.	12472.
368.	17187.	368.	9292.	368.	12479.
376.	17752.	376.	11486.	376.	18645.
384.	18448.	384.	11969.	384.	19515.
392.	19213.	392.	11132.	392.	16731.
400.	20196.	400.	11016.	400.	18274.
408.	19518.	408.	11817.	408.	14453.
416.	18768.	416.	10070.	416.	9664.
424.	17610.	424.	9718.	424.	8199.
432.	17644.	432.	9623.	432.	7762.
440.	18138.	440.	9423.	440.	7615.
448.	18540.	448.	11411.	448.	8840.
456.	18378.	456.	9580.	456.	7158.
464.	17294.	464.	10167.	464.	7792.
472.	16851.	472.	10115.	472.	6696.
480.	16141.	480.	9386.	480.	6828.
488.	16933.	488.	9114.	488.	6464.
496.	17632.	496.	10394.	496.	8734.
504.	18225.	504.	10557.	504.	8624.
512.	17746.	512.	10946.	512.	10378.
520.	17050.	520.	10903.	520.	11095.
528.	15786.	528.	10313.	528.	10105.
536.	15257.	536.	9095.	536.	15310.
544.	15689.	544.	8037.	544.	11198.
552.	15685.	552.	8268.	552.	16346.
560.	15639.	560.	8566.	560.	12684.
568.	14547.	568.	6897.	568.	10723.
576.	13870.	576.	6747.	576.	9833.
584.	13394.	584.	6667.	584.	9230.
592.	13125.	592.	6485.	592.	9722.
600.	12816.	600.	6205.	600.	8387.
608.	12753.	608.	5794.	608.	6751.
616.	12527.	616.	6868.	616.	6180.
624.	11901.	624.	6655.	624.	5782.
632.	11746.	632.	6347.	632.	5206.
640.	11138.	640.	5826.	640.	5353.
648.	10946.	648.	6580.	648.	5974.
656.	10828.	656.	5763.	656.	4849.
664.	10744.	664.	5443.	664.	4831.
672.	10730.	672.	5129.	672.	4535.
680.	10475.	680.	4914.	680.	4578.
688.	10222.	688.	5024.	688.	4777.
696.	9966.	696.	4240.	696.	4502.
704.	9772.	704.	4333.	704.	4213.
712.	9542.	712.	4172.	712.	4253.
720.	9598.	720.	4309.	720.	4009.
728.	9639.	728.	4319.	728.	4065.
736.	9508.	736.	4526.	736.	4181.
744.	9299.	744.	4557.	744.	4516.
752.	9323.	752.	4460.	752.	4120.
760.	9449.	760.	4603.	760.	4082.
768.	9753.	768.	4635.	768.	4460.
776.	9633.	776.	4961.	776.	4230.
784.	9619.	784.	4934.	784.	4957.
792.	9476.	792.	4594.	792.	4765.
800.	9613.	800.	4673.	800.	4593.
808.	9885.	808.	4761.	808.	4718.
816.	10360.	816.	4674.	816.	5472.
824.	10371.	824.	4671.	824.	5274.
832.	10038.	832.	5102.	832.	5628.
840.	9705.	840.	4917.	840.	6160.
848.	9560.	848.	4909.	848.	5849.
856.	10098.	856.	4896.	856.	5924.
864.	10648.	864.	4729.	864.	5833.
872.	11265.	872.	5443.	872.	6151.
880.	11369.	880.	5524.	880.	7291.
888.	10688.	888.	5666.	888.	6374.
896.	9690.	896.	5562.	896.	5783.
904.	10073.	904.	5432.	904.	5313.
912.	10994.	912.	5568.	912.	5530.
920.	12207.	920.	5967.	920.	5692.
928.	13348.	928.	6517.	928.	6453.
936.	14676.	936.	7154.	936.	6237.
944.	13203.	944.	8024.	944.	6002.
952.	13205.	952.	7895.	952.	6829.
960.	13928.	960.	7879.	960.	6552.
968.	15276.	968.	7878.	968.	8518.
976.	18196.	976.	9241.	976.	10152.
984.	18163.	984.	10368.	984.	13525.
992.	17749.	992.	9813.	992.	11279.
1000.	17391.	1000.	9924.	1000.	12409.
1008.	16757.	1008.	8998.	1008.	12622.
1016.	15653.	1016.	9545.	1016.	13878.
1024.	18158.	1024.	9236.	1024.	17724.
1032.	18315.	1032.	9282.	1032.	11120.
1040.	17921.	1040.	9456.	1040.	13813.
1048.	17895.	1048.	9707.	1048.	13259.

Figure B5. Interval velocities for 1996 site 1, with an 80 interval.

696	121.190102	260.186615	250.693207
704	121.942596	261.262604	252.228195
712	122.021103	262.622498	252.487503
720	122.365196	264.026215	255.160706
728	123.443497	265.504211	255.687698
736	125.073196	267.656586	256.663086
744	125.326599	268.981812	258.250397
752	127.288300	270.222809	259.698608
760	126.844498	271.482788	260.596497
768	127.102303	273.109314	261.828613
776	128.488007	274.963104	263.054504
784	128.913101	276.145905	264.336914
792	130.580704	276.555115	265.503693
800	130.206406	277.008789	266.779388
808	131.142197	277.655396	267.948914
816	132.052994	278.202698	268.823090
824	132.644897	279.421112	269.994385
832	133.968994	281.281189	271.263702
840	133.964798	282.550903	272.569489
848	134.072006	284.728302	273.634094
856	134.792297	285.901215	274.943298
864	135.108398	287.457489	275.866089
872	136.671295	288.004303	277.098785
880	136.162094	288.520111	278.080200
888	137.374100	288.863403	279.253601
896	136.760605	289.195709	280.033813
904	137.298096	289.525085	281.380096
912	137.631500	290.774200	282.698700
920	138.342697	294.761993	285.381897
928	138.426102	295.265503	286.153900
936	139.609100	295.453705	285.633911
944	140.429794	295.311615	285.668213
952	139.533005	295.349701	285.933105
960	139.665298	295.289612	286.174988
968	140.105301	295.306702	286.410004
976	138.373703	295.158112	286.709412
984	139.913300	295.245300	287.206512
992	141.134796	295.248505	287.450287
1000	140.499603	295.193115	287.684814
1008	139.479401	295.315399	288.115295
1016	139.379807	295.601501	289.019501
1024	139.646194	295.538910	289.968811
1032	139.862106	295.606293	290.248413
1040	140.029800	295.683990	290.547913
1048	140.287704	295.799286	290.385712
1056	140.178604	295.973511	291.311401
1064	140.561096	296.133698	291.346588
1072	140.430801	296.177002	291.812592
1080	140.750504	296.282898	292.083099
1088	141.123901	296.391510	292.456787

Figure B6. Travel times for 1996 site 3. The columns are depth (ft.), P time, S1 (in-line) time and S2 (cross-line) time.

696	105.702904	230.274399	223.496002
704	106.180199	231.616302	224.936096
712	106.839401	232.699402	225.323303
720	107.529297	233.883301	226.788406
728	108.329300	235.238495	228.916794
736	109.363098	236.337708	230.800598
744	109.931702	237.198105	232.413101
752	110.614403	237.797501	234.058807
760	111.382301	238.522903	235.232803
768	111.928497	240.124802	235.631302
776	112.629097	242.376099	235.869202
784	112.872002	243.908005	237.239197
792	113.719803	244.603897	238.762695
800	114.433296	245.717300	240.072800
808	115.031303	246.948807	241.092697
816	115.736099	248.411499	242.537994
824	116.174301	249.360703	243.828293
832	116.665604	250.310806	244.881607
840	117.240799	251.461899	246.737900
848	118.028801	252.782898	248.128799
856	118.958603	253.700699	248.637207
864	119.775200	254.377197	249.633408
872	120.203300	255.017197	251.218597
880	120.717499	256.052795	251.790604
888	121.223999	257.721588	252.775497
896	121.876297	258.765991	254.180496
904	122.350403	259.432404	254.968506
912	122.818001	260.082214	255.261902
920	123.334000	261.183289	256.419800
928	124.367500	262.934113	258.222900
936	125.856201	264.302612	259.302795
944	125.965599	264.450592	259.827698
952	126.087303	264.577087	260.783600
960	126.259102	264.661591	259.219788
968	126.354301	264.819397	259.497986
976	126.196404	264.799805	259.640594
984	126.568703	265.001312	260.027191
992	126.632301	265.264313	260.589203
1000	126.590103	265.465698	260.882202
1008	126.817200	265.714508	261.624298
1016	126.830200	266.033295	262.257507
1024	126.615402	266.200104	263.025208
1032	126.620201	266.461609	262.955597
1040	126.569000	266.720703	263.600006
1048	126.790604	267.038788	264.213013
1056	127.366600	267.392395	264.502899
1064	127.185600	267.444092	264.876709
1072	127.474403	267.633514	265.012207
1080	127.689697	267.825806	265.420898
1088	128.060806	268.104401	266.004913

Figure B7. Travel times for 1996 site 4. The columns are depth (ft.), P time, S1 (in-line) time and S2 (cross-line) time.

Depth96	P96
696	187.000000
704	188.000000
712	189.000000
720	189.000000
728	191.000000
736	191.333328
744	191.666656
752	192.000000
760	193.500000
768	193.500000
776	195.000000
784	195.500000
792	196.000000
800	196.000000
808	196.000000
816	197.000000
824	197.000000
832	199.000000
840	200.500000
848	201.000000
856	201.000000
864	201.000000
872	201.500000
880	201.500000
888	201.000000
896	200.500000
904	200.666656
912	200.833328
920	201.000000
928	202.000000
936	201.500000
944	201.750000
952	202.000000
960	202.250000
968	202.500000
976	203.000000
984	202.000000
992	202.500000
1000	202.166672
1008	201.833344
1016	201.500000
1024	200.000000
1032	199.500000
1040	200.500000
1048	200.000000
1056	199.750000
1064	199.500000
1072	199.500000
1080	199.500000
1088	199.000000

Figure B8. Travel times for 1996 site 6. The columns are depth (ft.), P time.

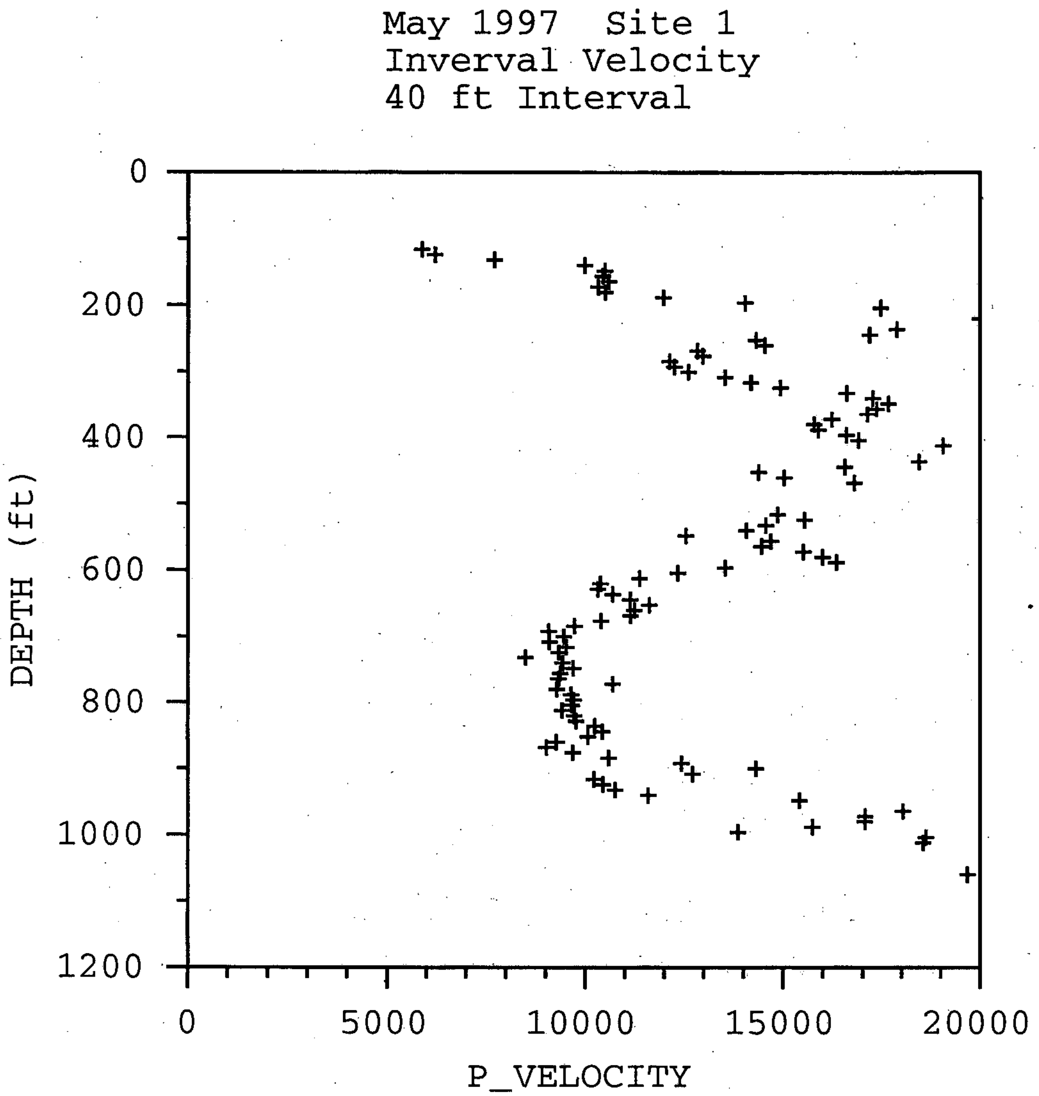

Figure B9. Plot of P-wave interval velocities for 1996 site 1 using a 40 ft. interval.

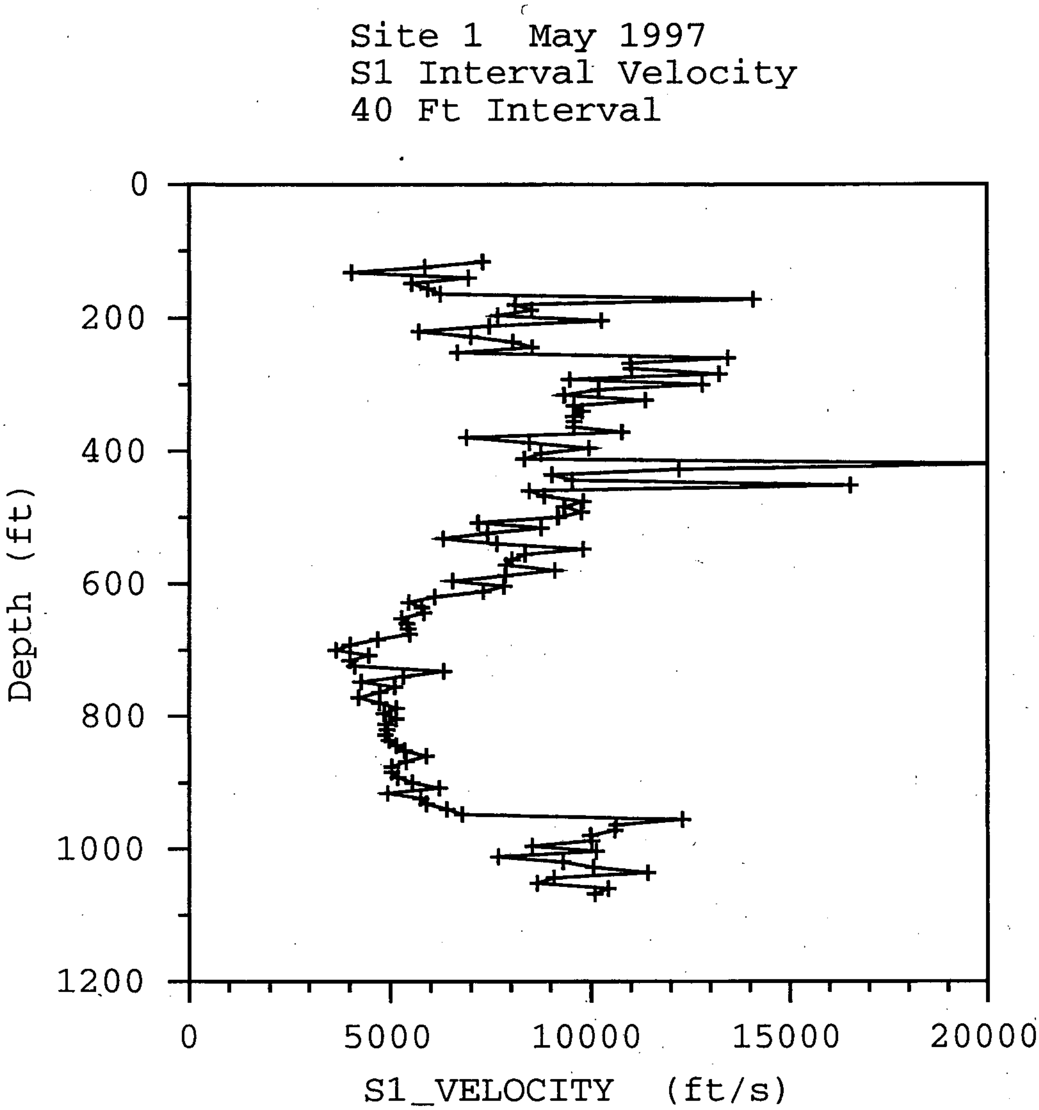

Figure B10. Plot of S-wave (in-line source) interval velocities for 1996 site 1 using a 40 ft. interval.

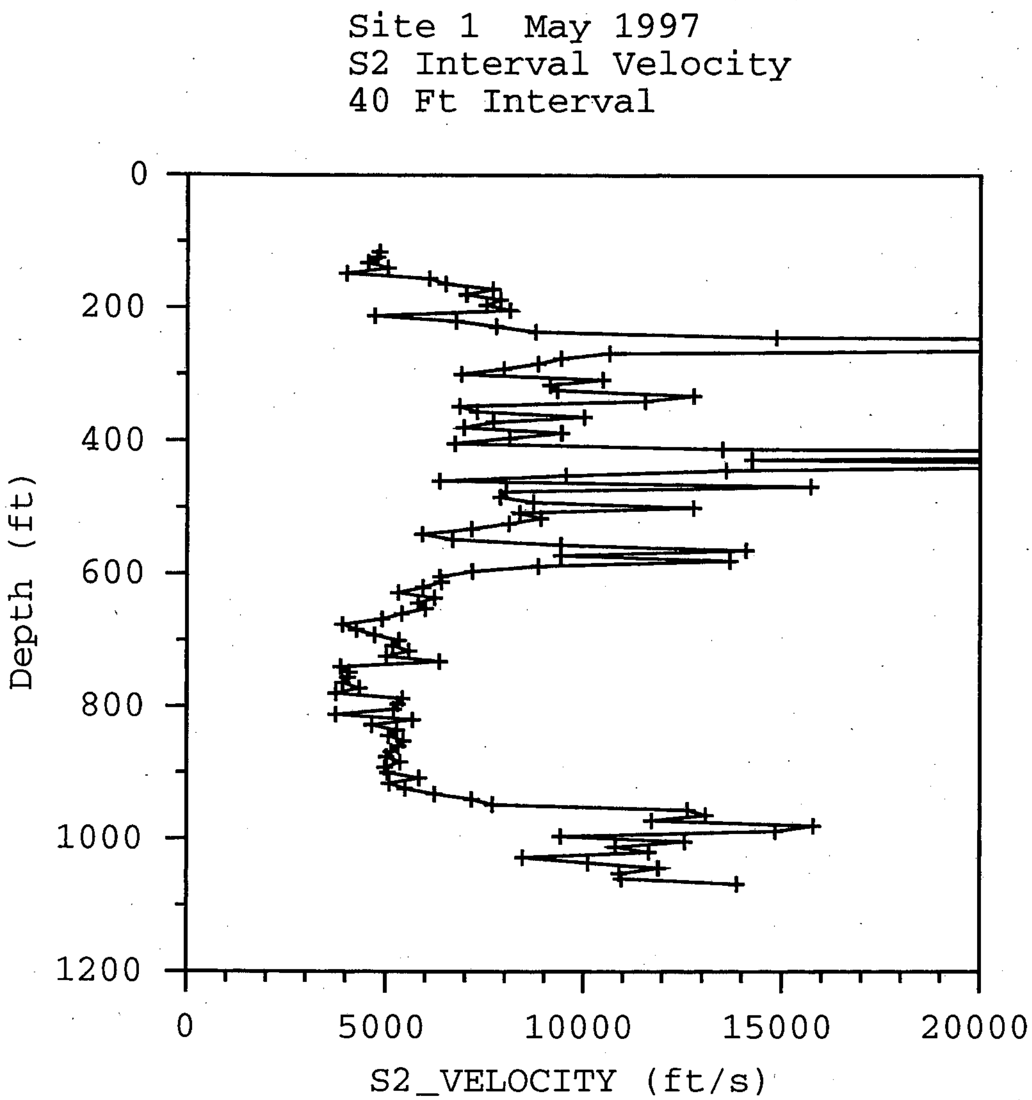

Figure B11. Plot of S-wave (cross-line source) interval velocities for 1996 site 1 using a 40 ft. interval.

Appendix C: Time Lapse and Travel Time Difference Plots

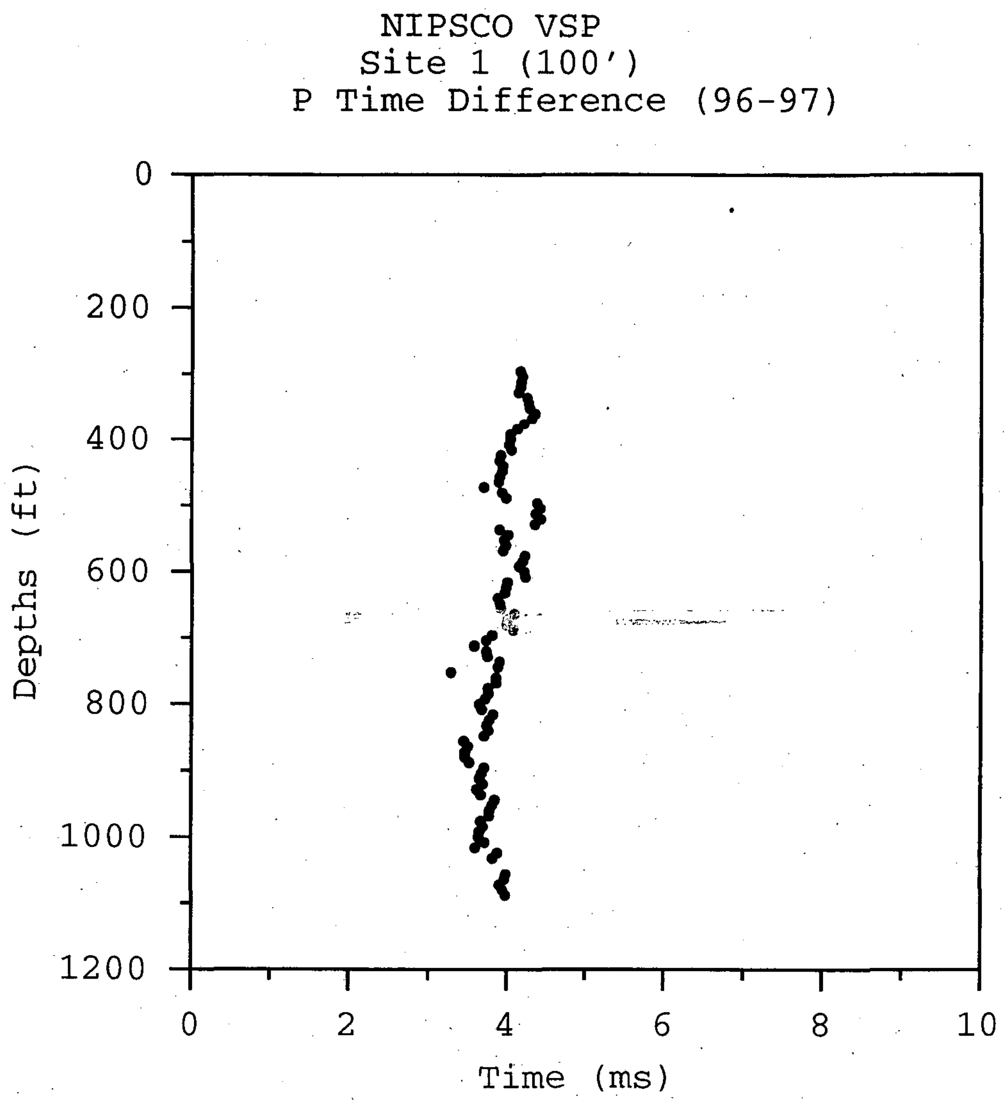

Figure C1a. Time-lapse change in P-wave travel time at site 1.

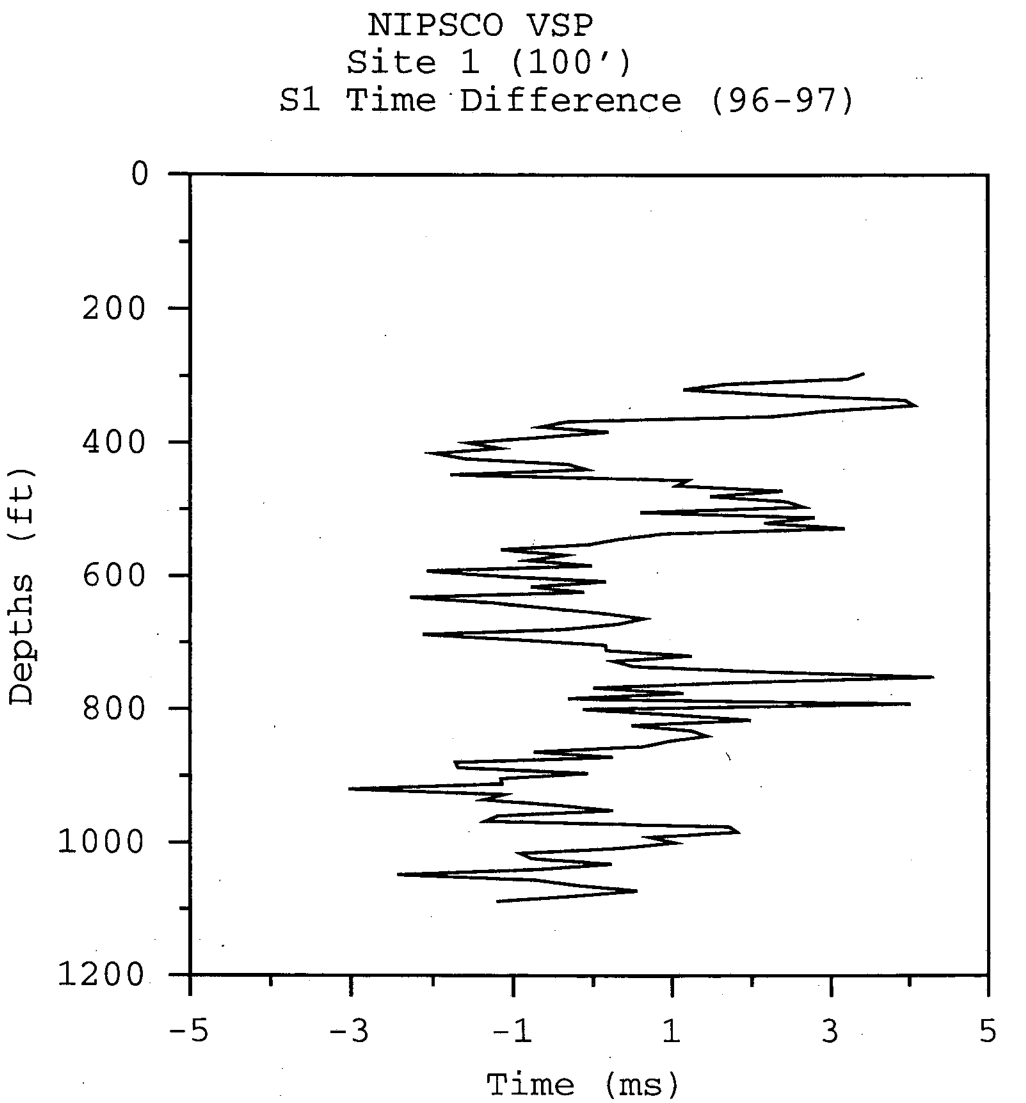

Figure C1b. Time-lapse change in S-wave (in-line source) travel time at site 1.

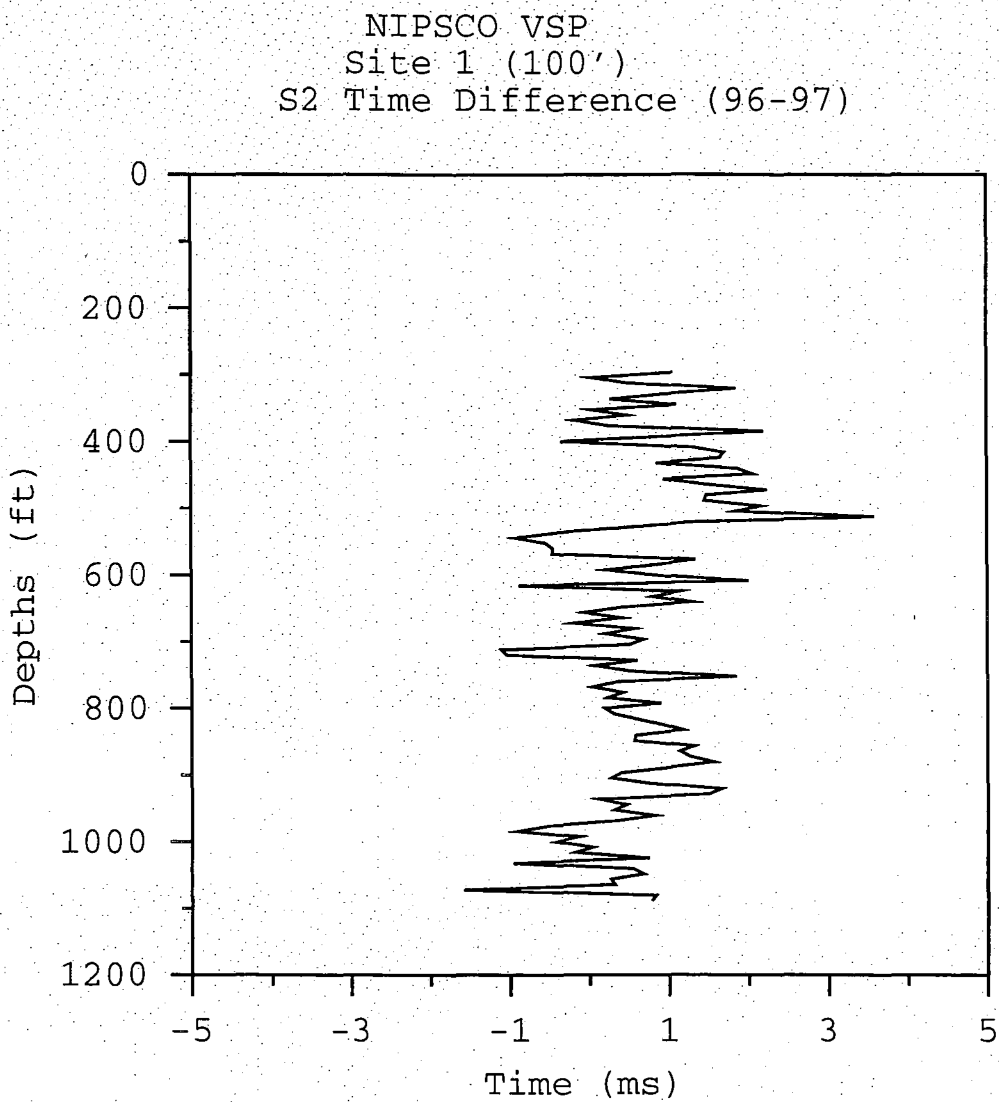

Figure C1c. Time-lapse change in S-wave (cross-line source) travel time at site 1.

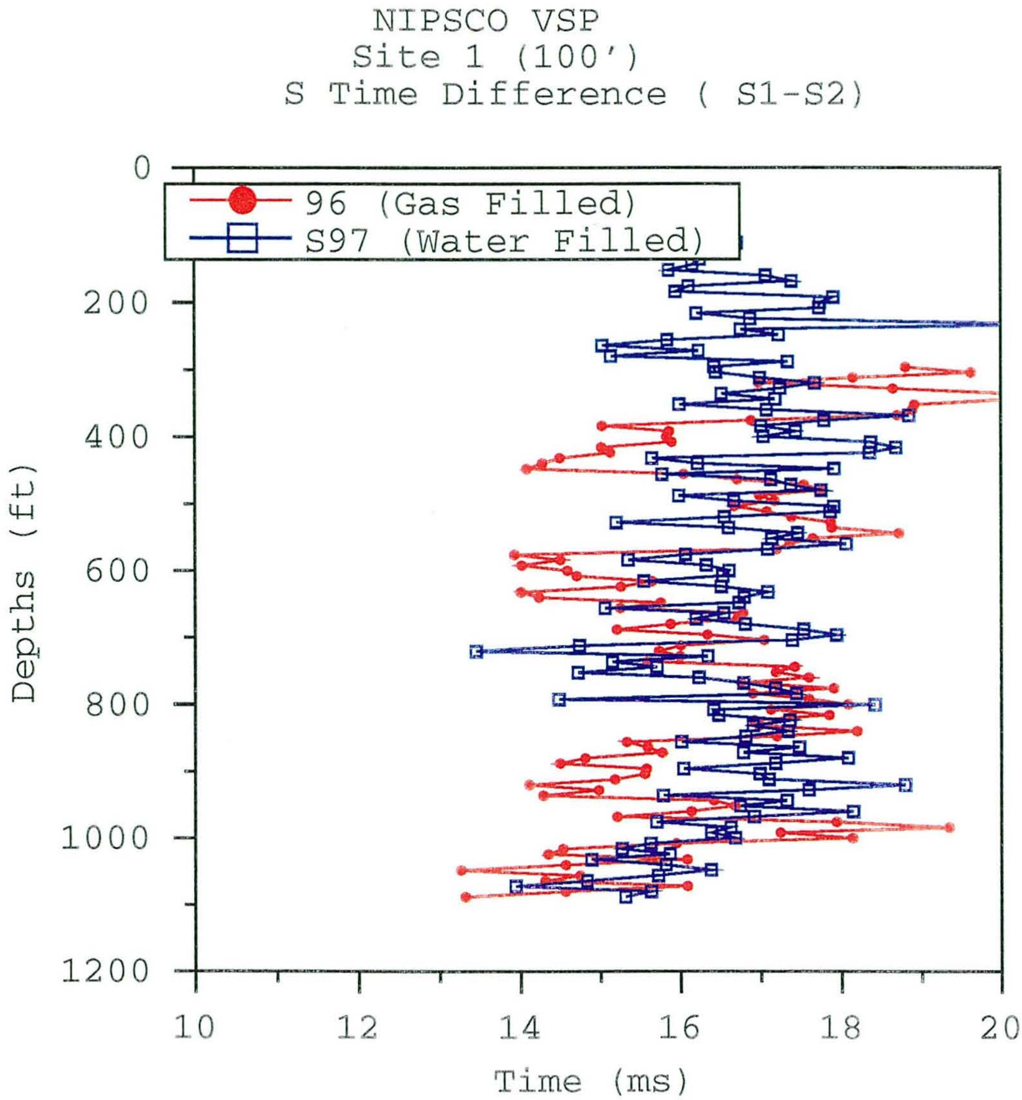

Figure C1d. Travel time difference between S1 (in-line, E-W) and S2 (cross-line, N-S) at site 1 for 1996 and 1997 surveys.

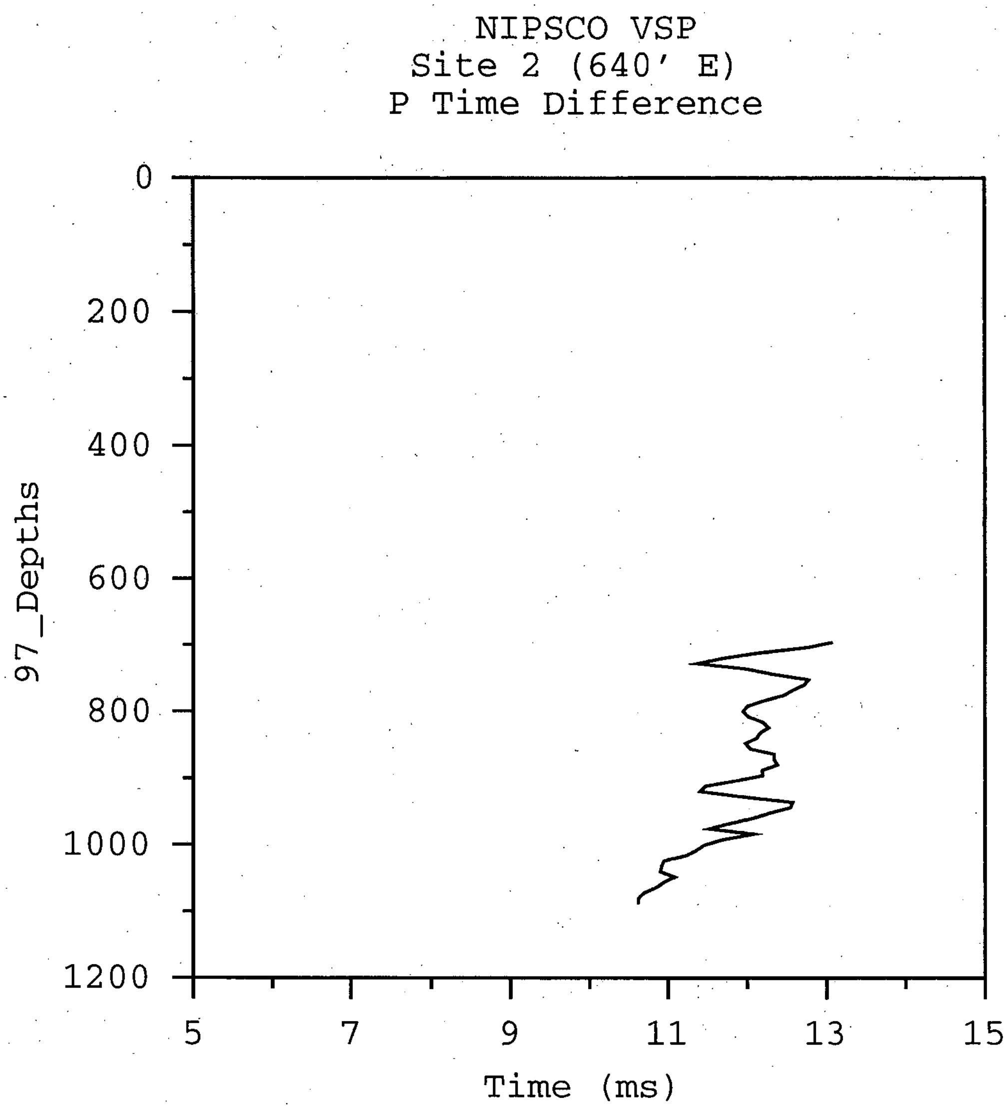

Figure C2a. Time-lapse change in P-wave travel time at site 2.

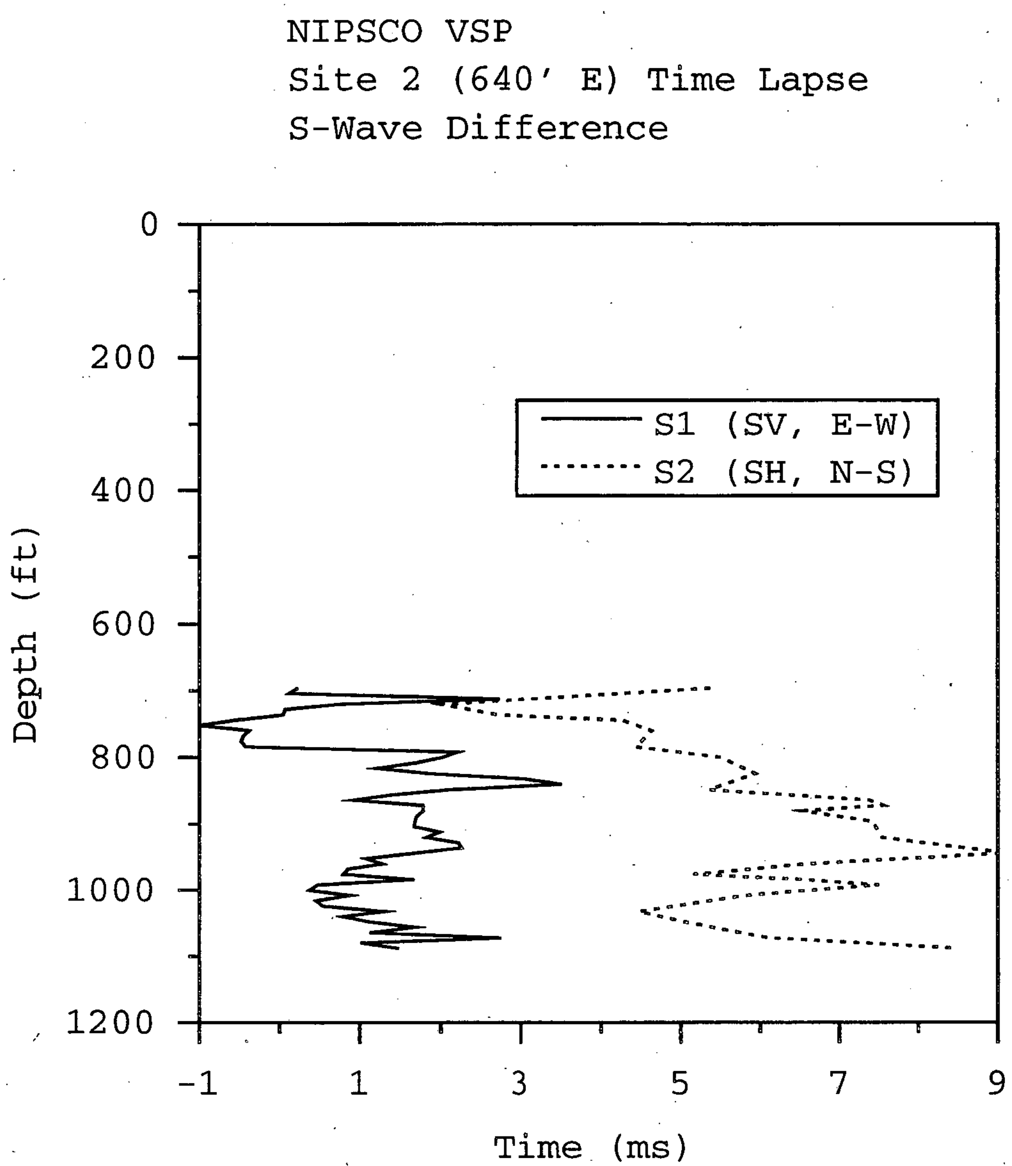

Figure C2b. Time-lapse change in S-wave travel time at site 2 for S1 (in-line, E-W) and S2 (cross-line, N-S) for 1996 minus 1997.

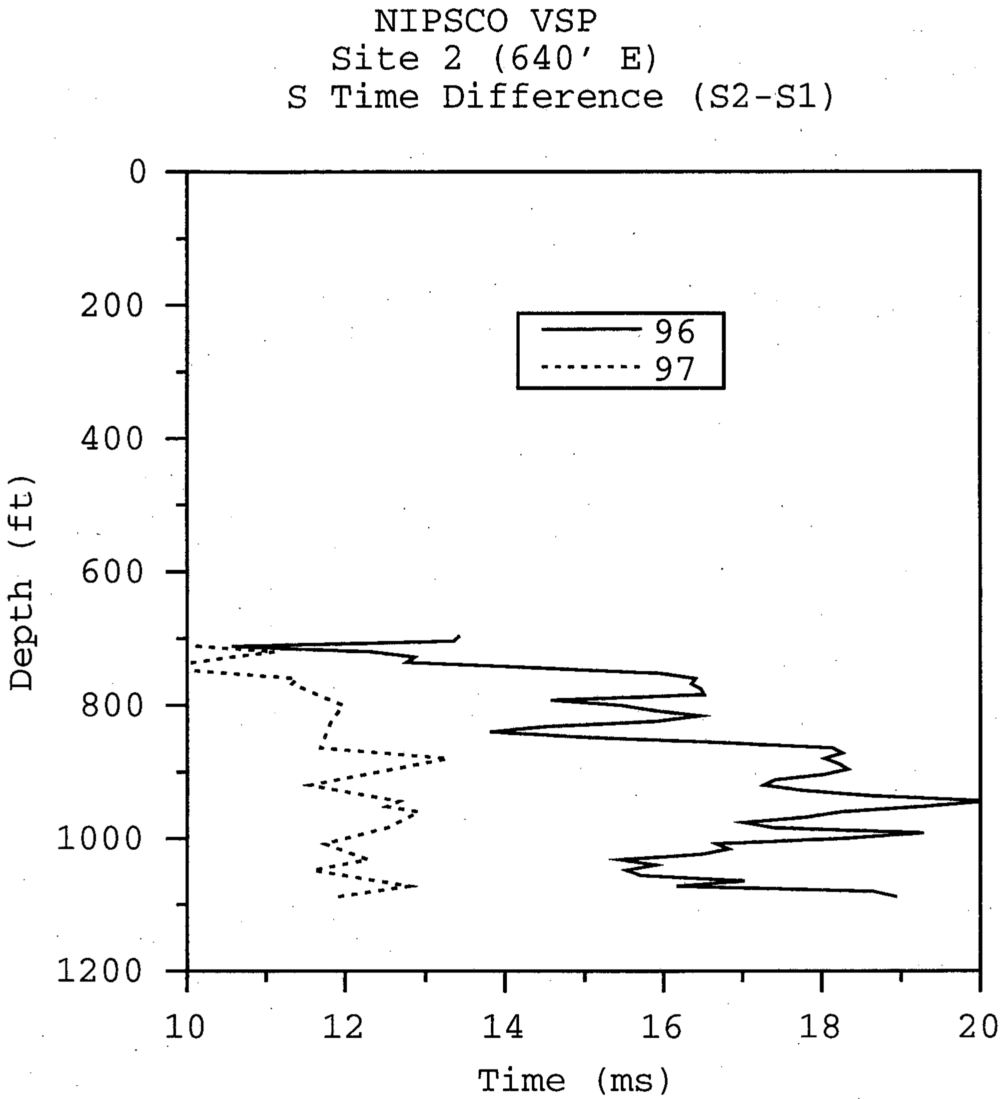

Figure C2c. Travel time difference between S1 (in-line, E-W) and S2 (cross-line, N-S) at site 2 for 1996 and 1997 surveys.

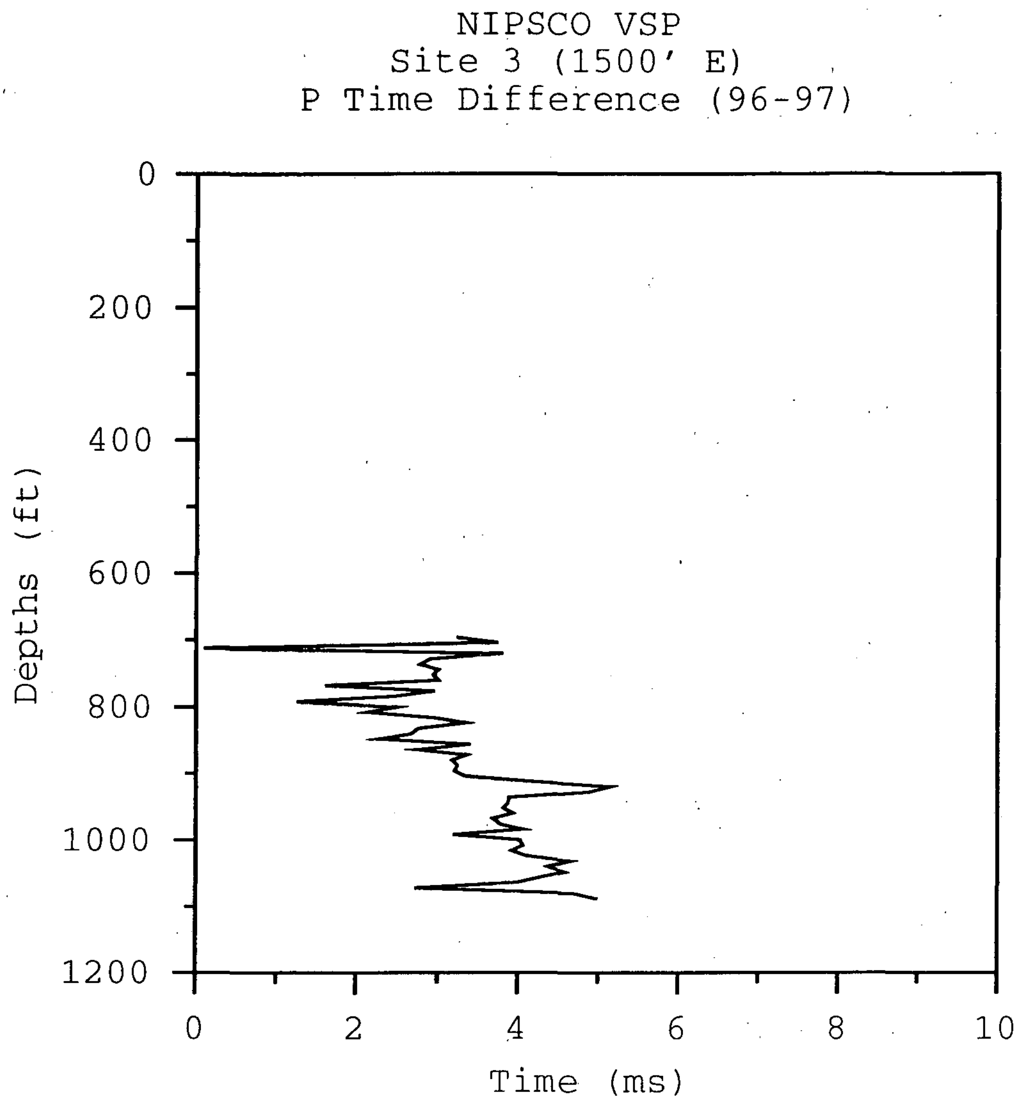

Figure C3a. Time-lapse change in P-wave travel time at site 3.

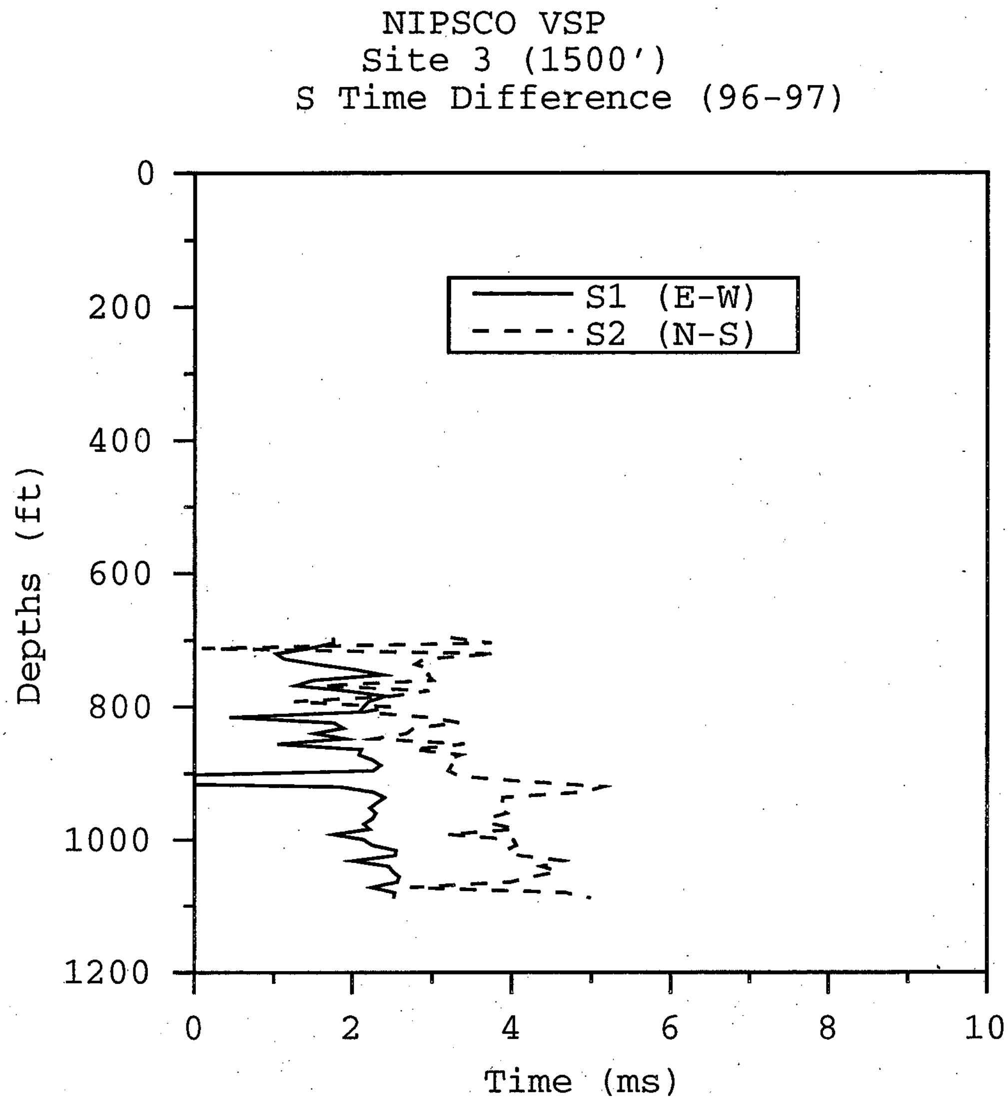

Figure C3b. Time-lapse change in travel time at site 3 for S1 (in-line, E-W) and S2 (cross-line, N-S).

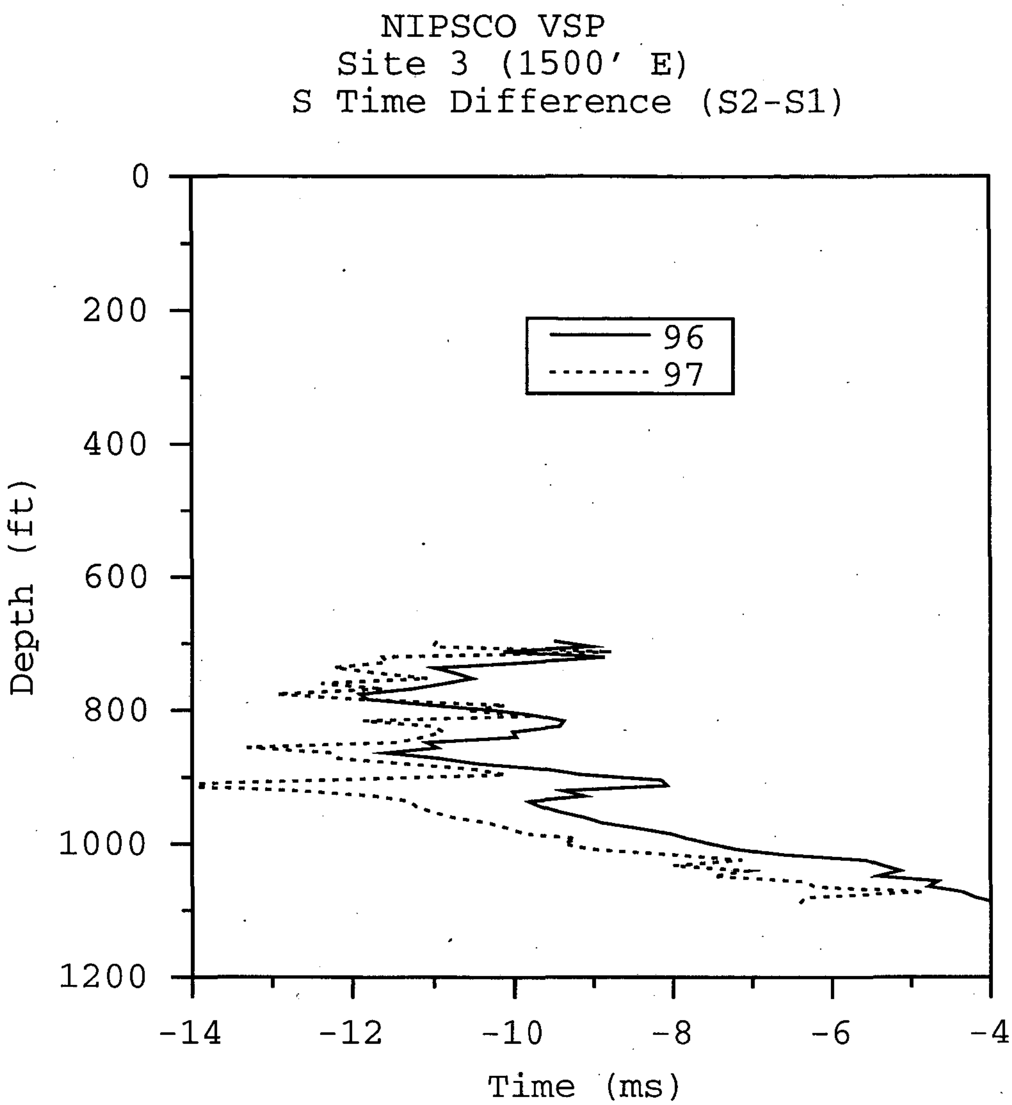

Figure C3c. Travel time difference between S2 (cross-line) and S1(in-line) for 1996 and 1997 surveys.

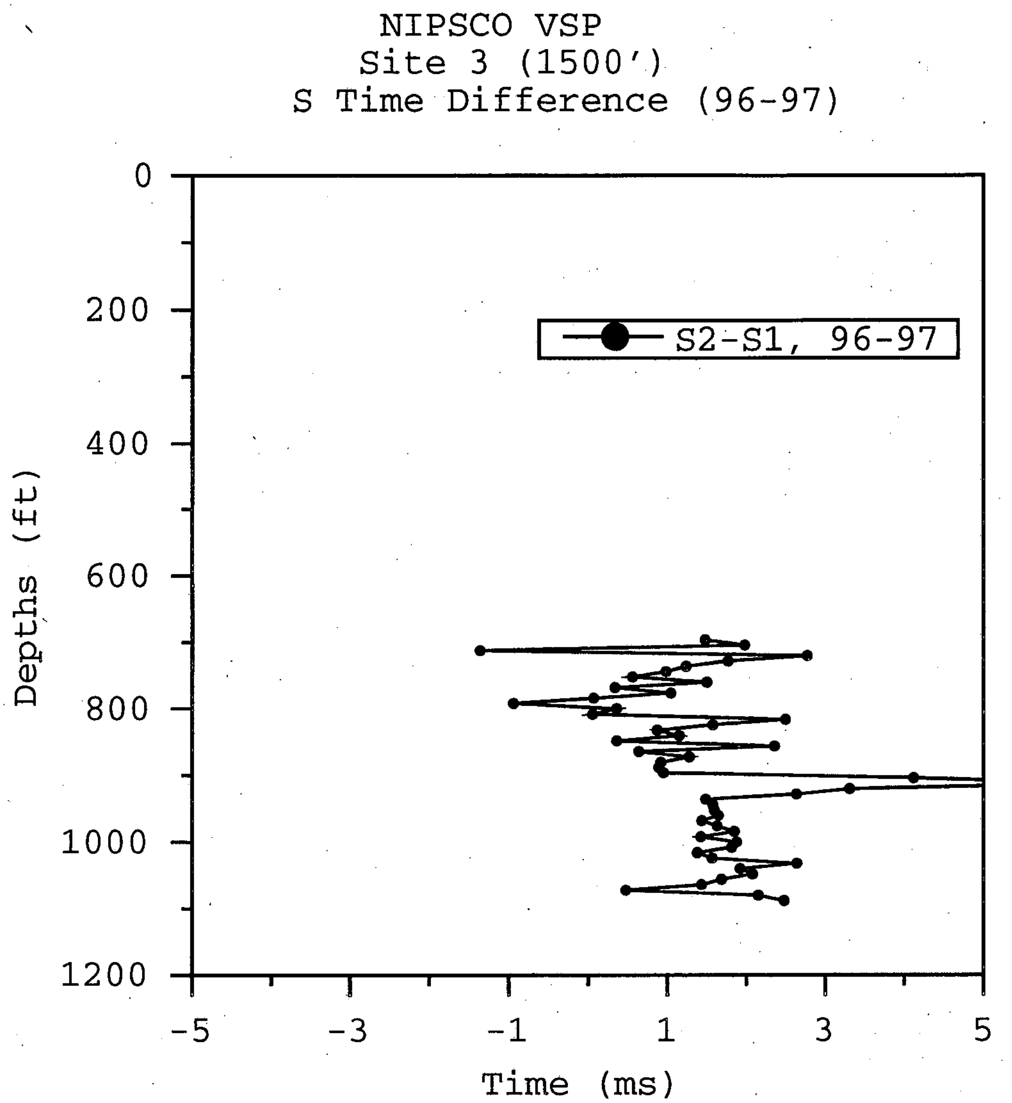

Figure C3d. Time-lapse travel time difference for site 3, S2 minus S1 and 1996 minus 1997.

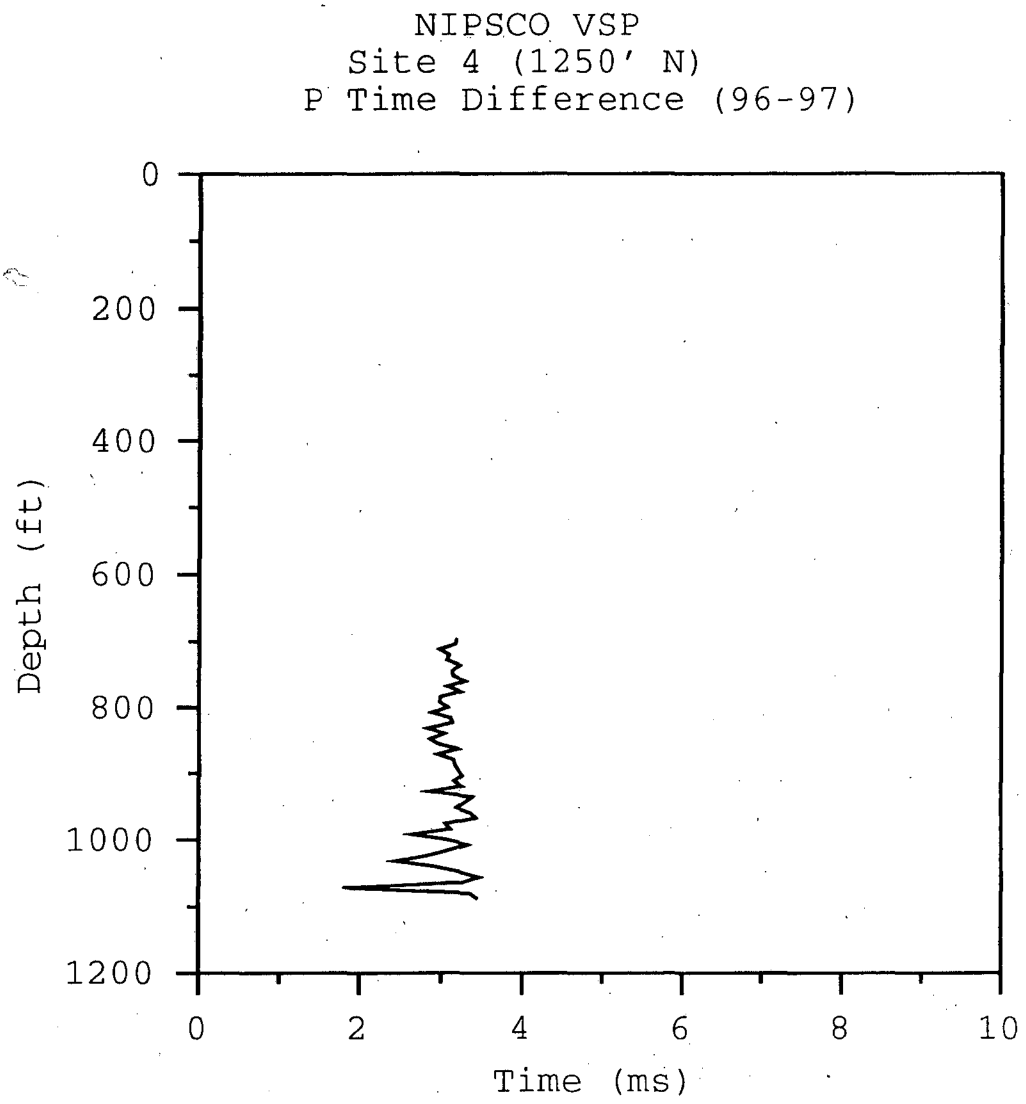

Figure C4a. Time-lapse change in P-wave travel time at site 4.

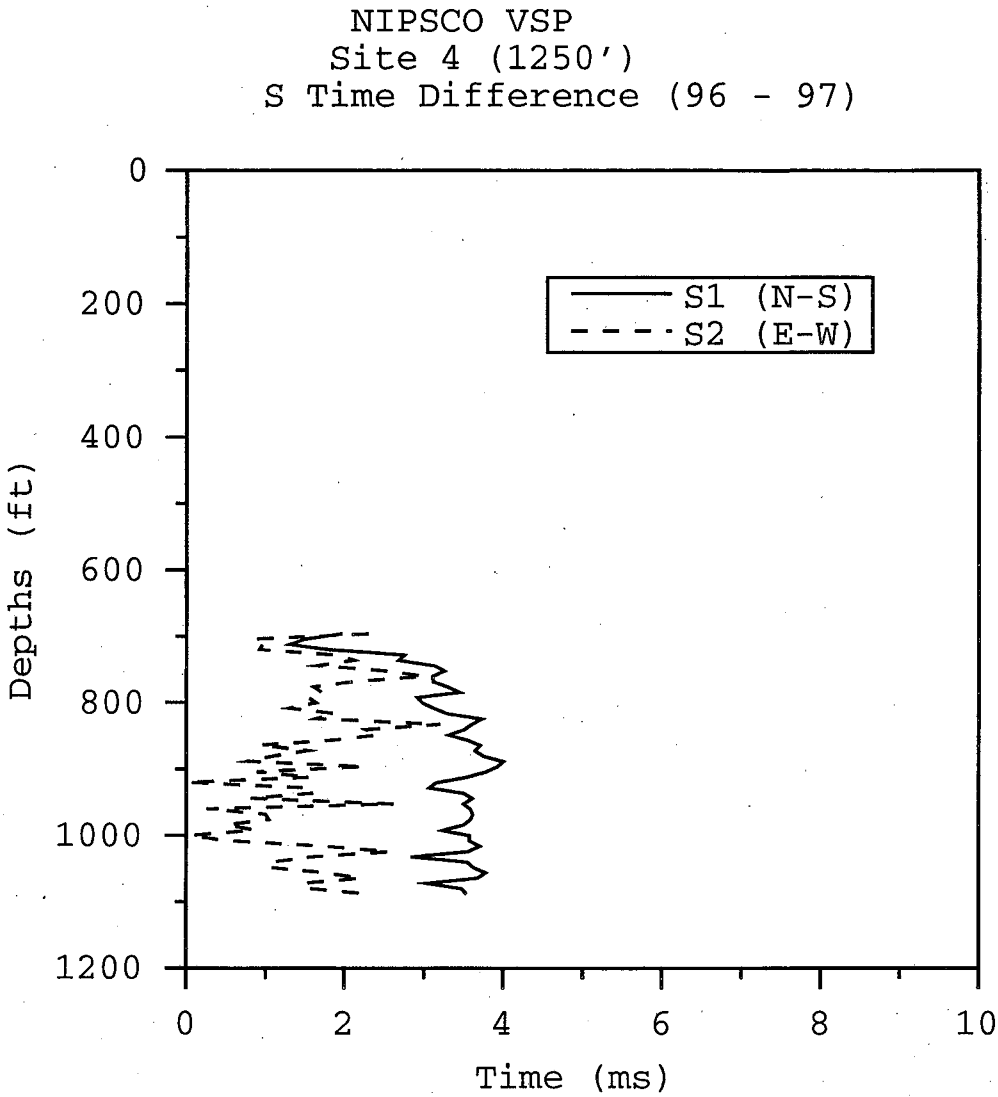

Figure C4b. Time-lapse change in travel time at site 4 for S1 (in-line, E-W) and S2 (cross-line, N-S).

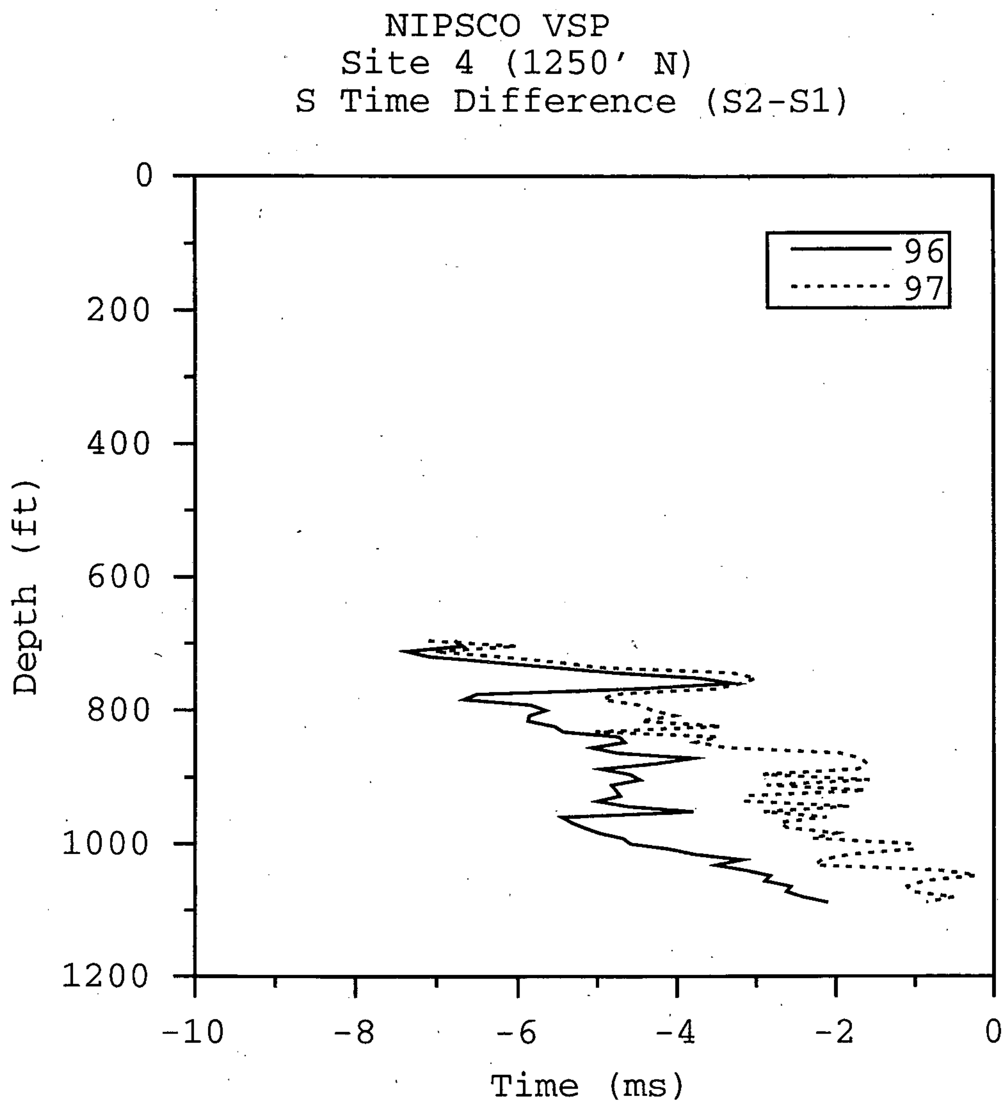

Figure C4c. Travel time difference between S2 (cross-line) and S1(in-line) for 1996 and 1997 surveys at site 4.

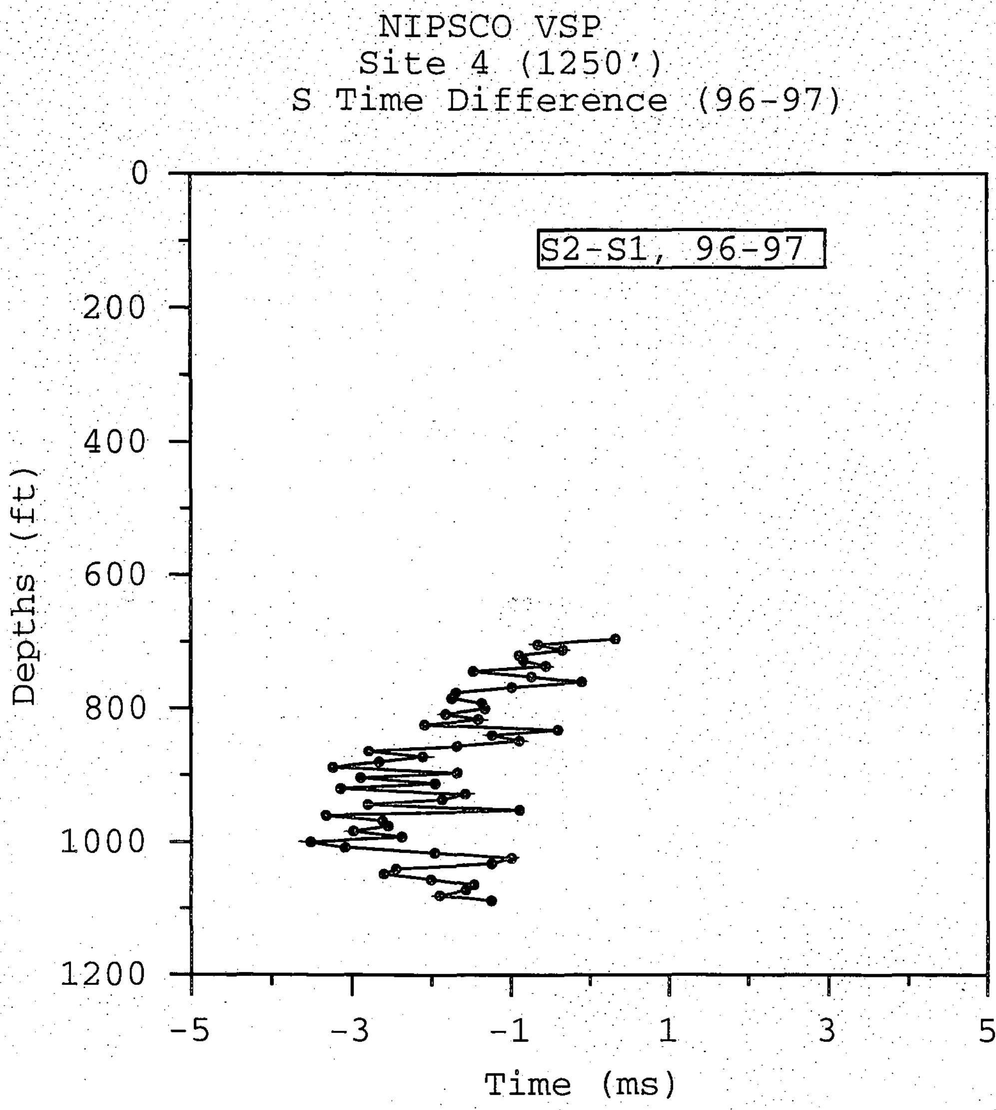

Figure C4d. Time-lapse travel time difference for site 4, S2 minus S1 and 1996 minus 1997.

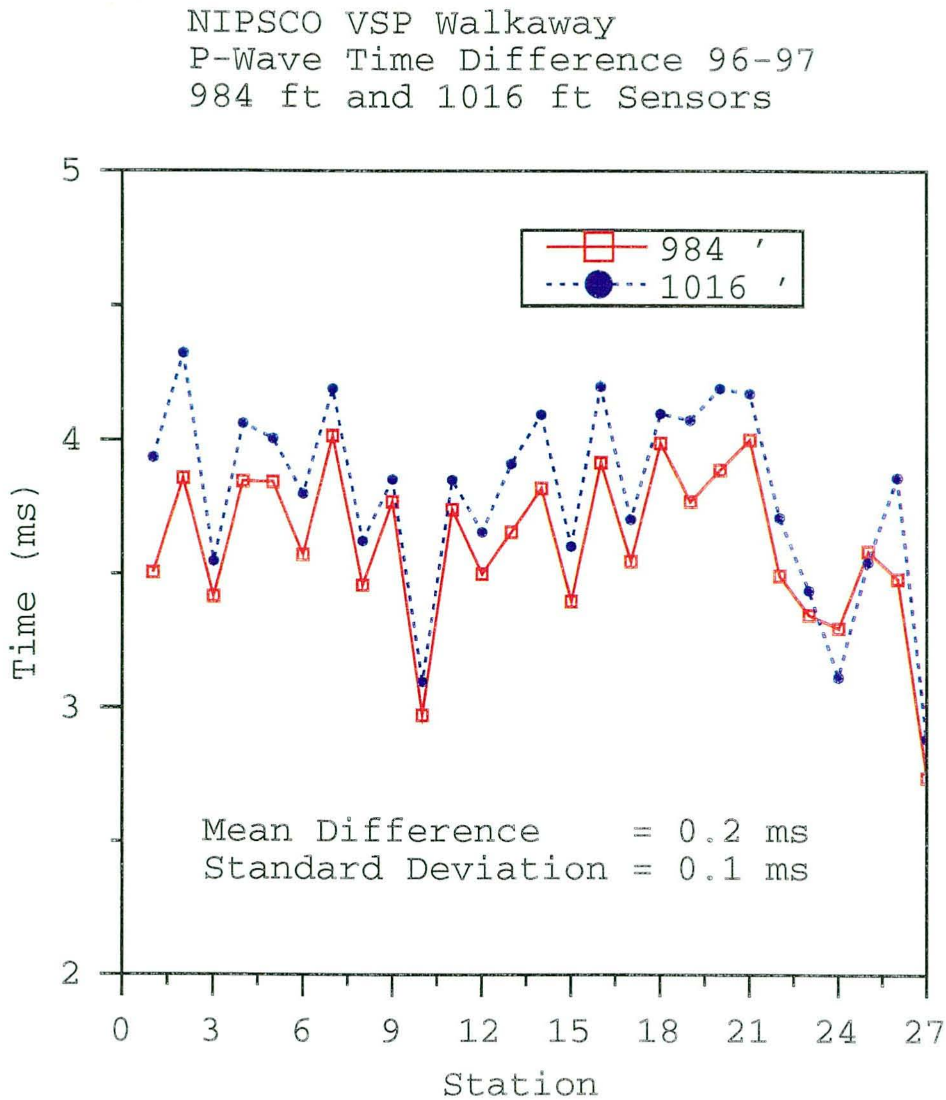

Figure C5a. Time lapse P-wave time change for walkaway survey for two sensors (984 and 1016').

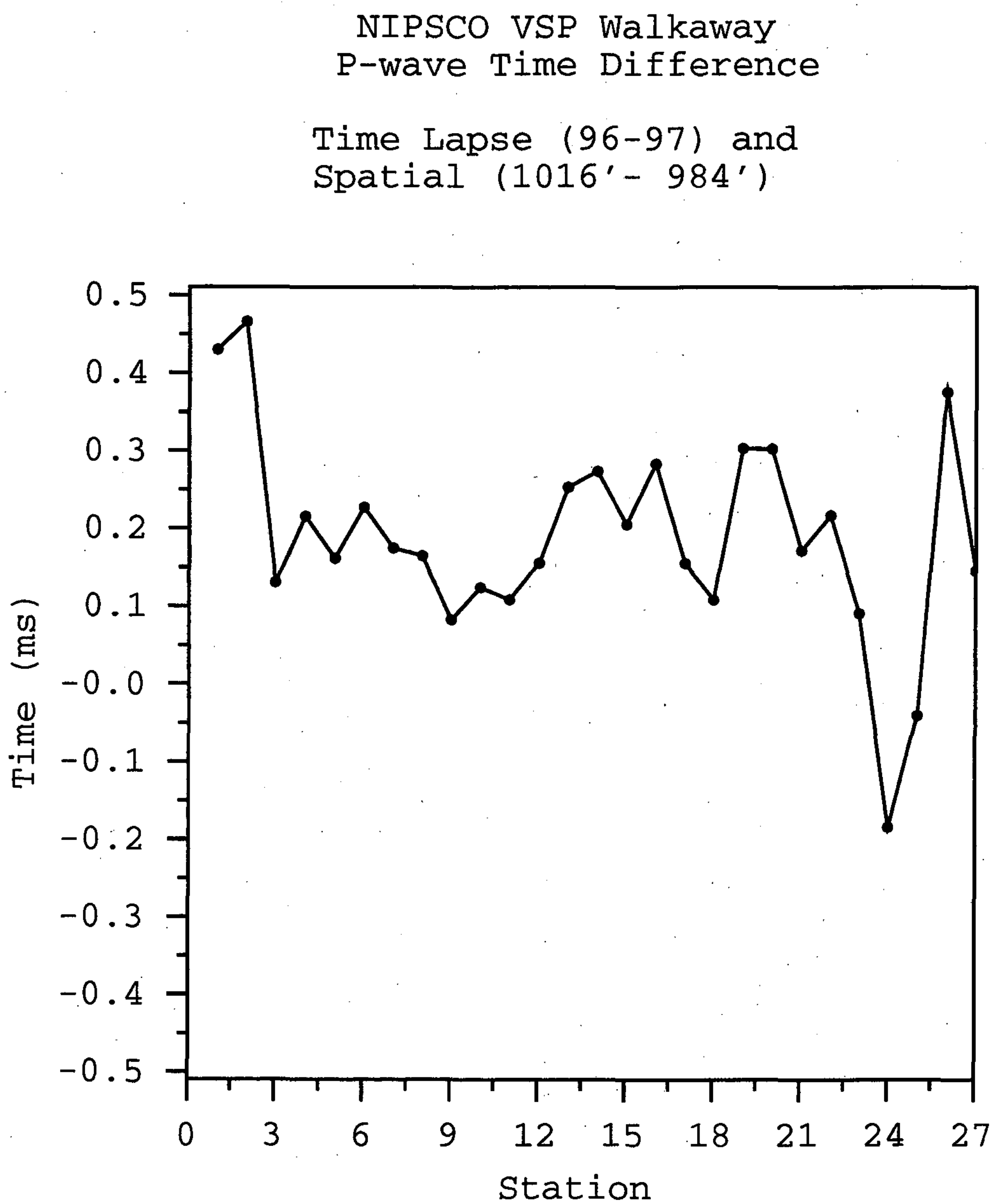

Figure C5b. Time lapse and spatial change for P-wave walkaway.

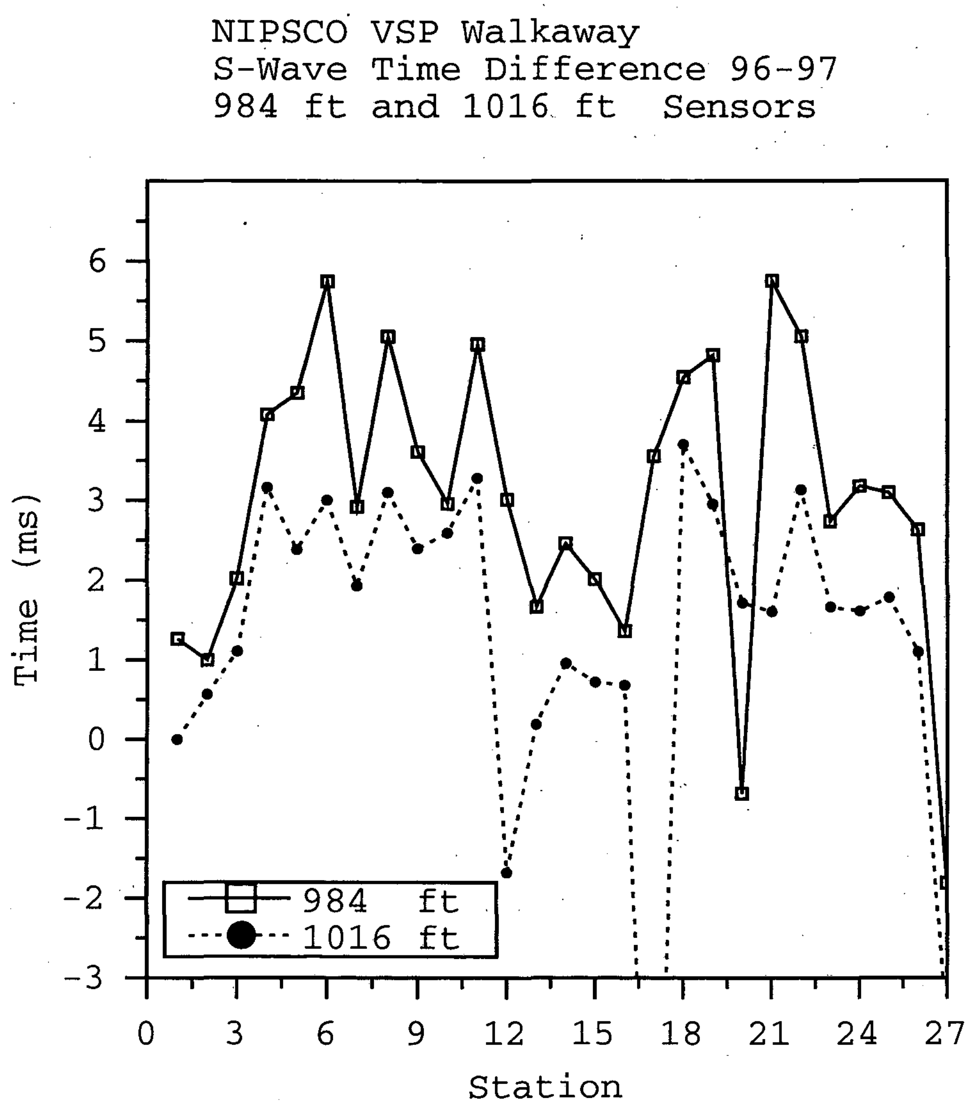

Figure C5c. Time lapse S-wave (cross-line source) time change for walkaway survey for two sensors (984 and 1016').

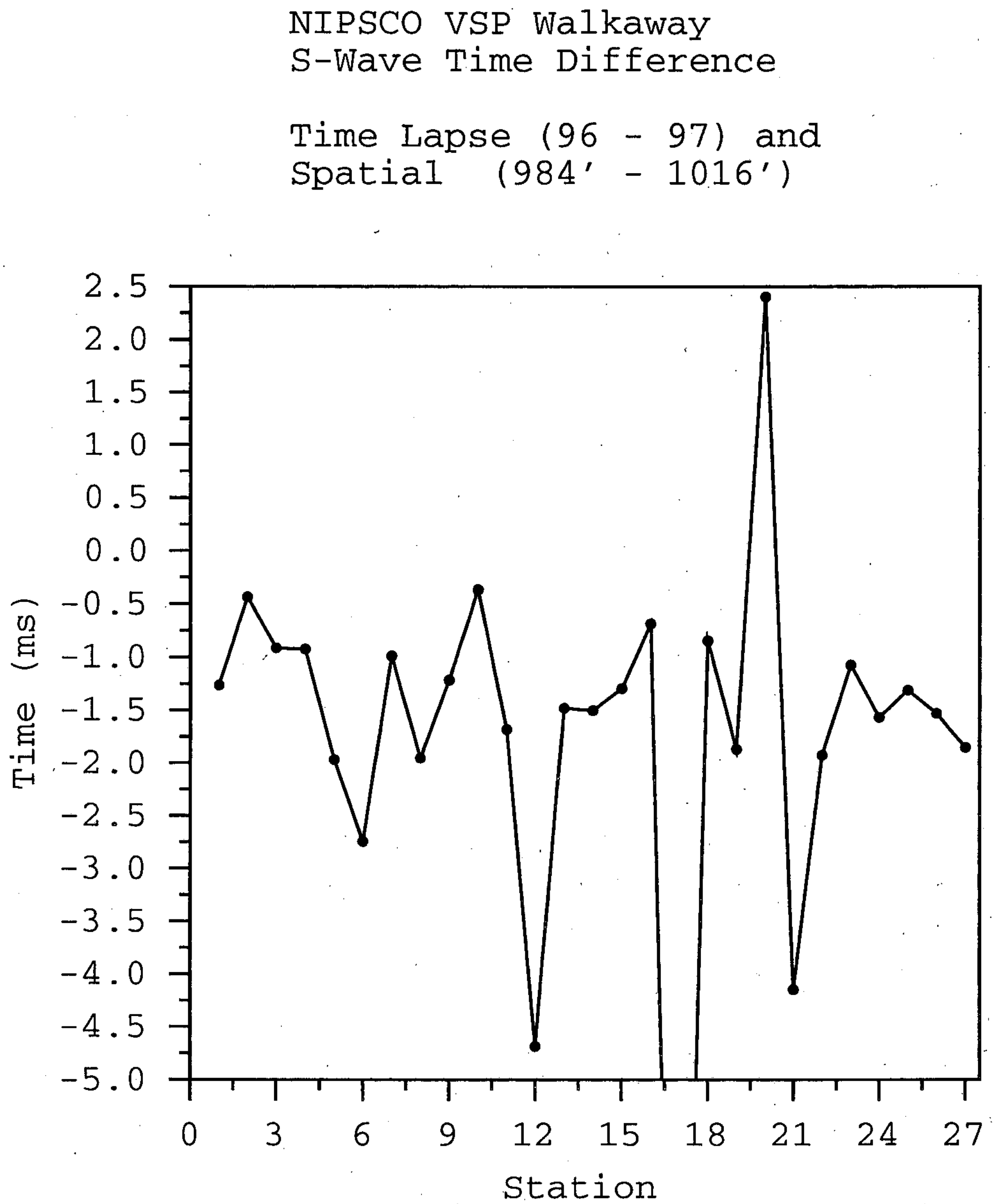

Figure C5d. Time lapse and spatial change for S-wave (cross-line source) time change for walkaway survey for two sensors (984 and 1016').

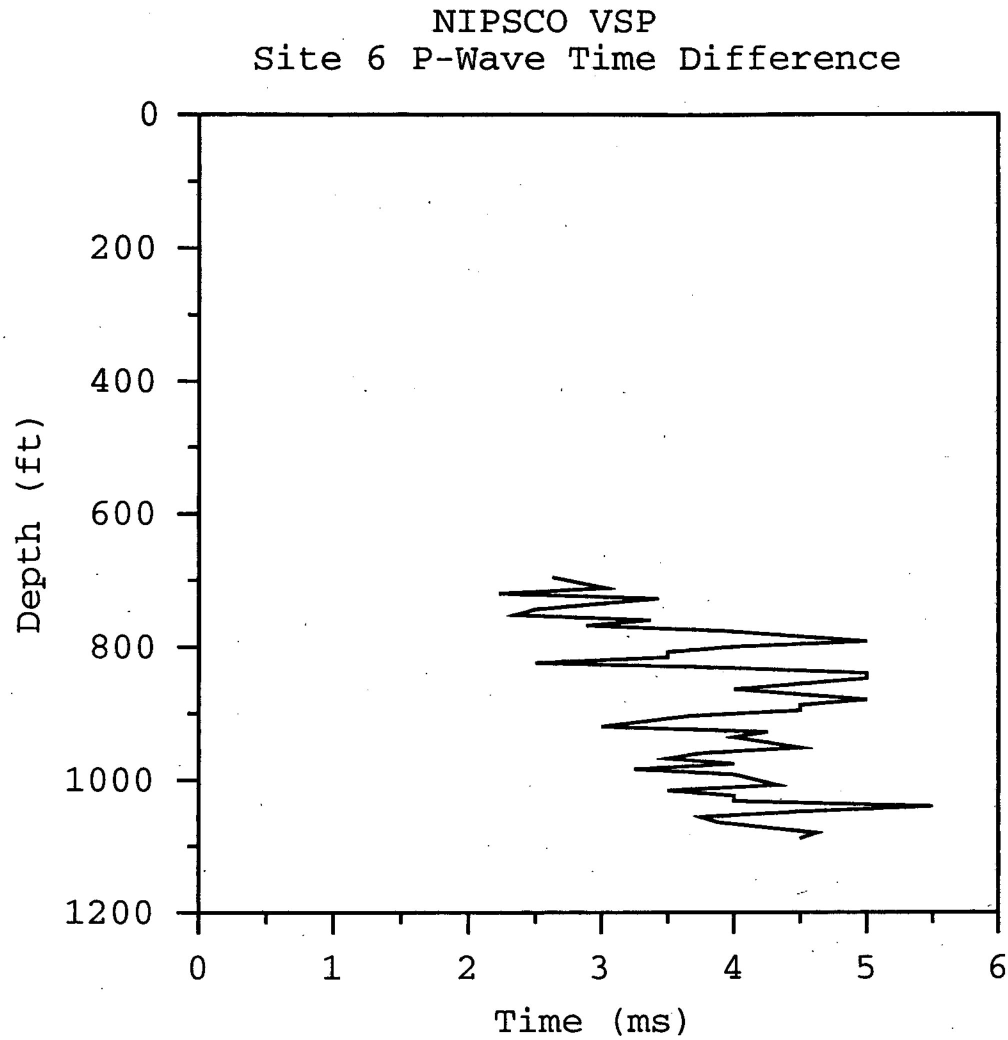

Figure C6. Time lapse P-wave time change for site 6 (1996 - 1997).

Appendix D: Other Studies and Analysis

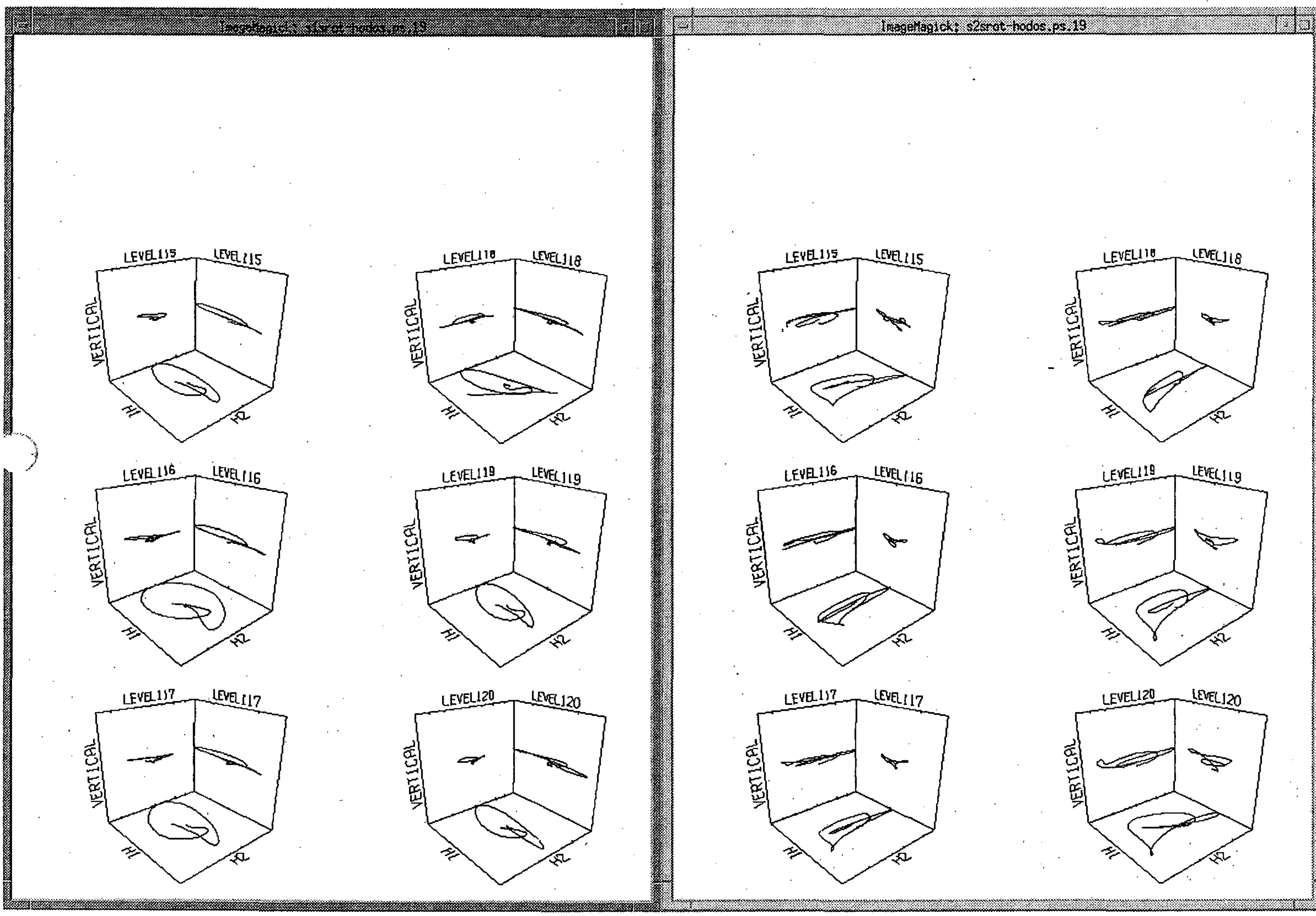

Figure D1a. Particle motion for comparison for 1997 site 1 S-waves. S1 (in-line, E-W) source (left side) and S2 (cross-line, N-S) source (right side). Level number is sequential from shallowest (96 ft.).

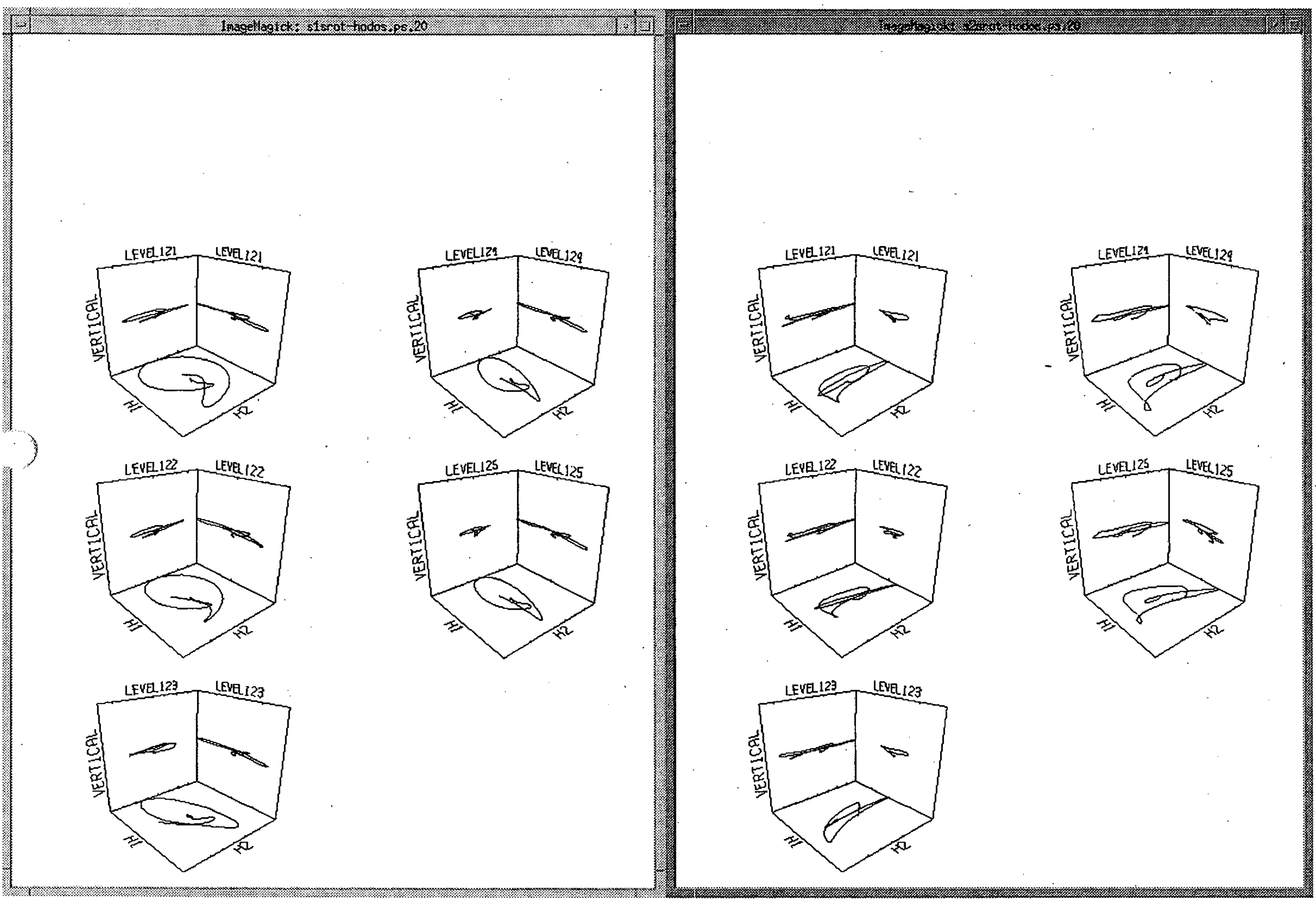

Figure D1b. Particle motion for comparison for 1997 site 1 S-waves. S1 (in-line, E-W) source (left side) and S2 (cross-line, N-S) source (right side). Level number is sequential from shallowest (96 ft.).

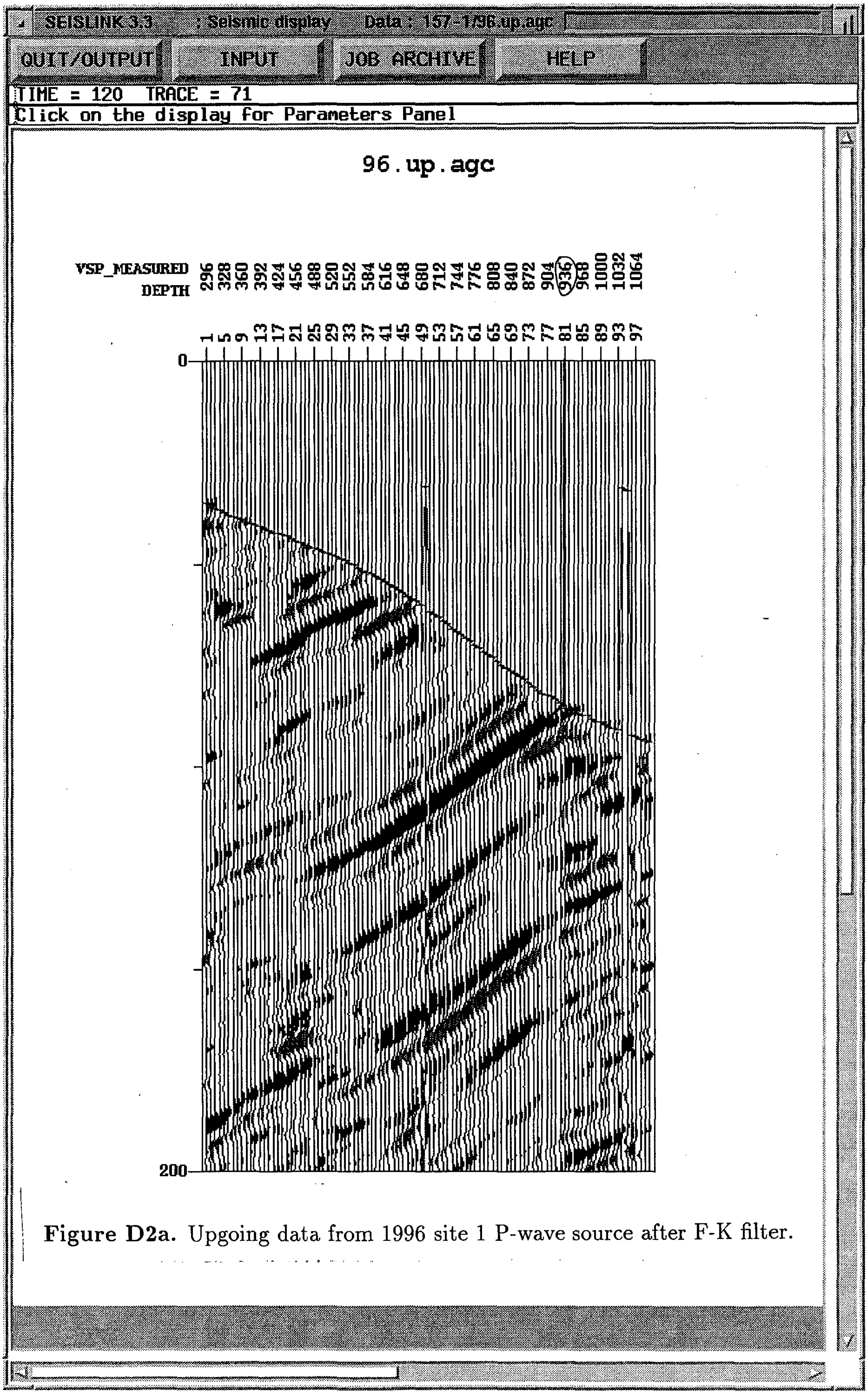

Figure D2a. Upgoing data from 1996 site 1 P-wave source after F-K filter.

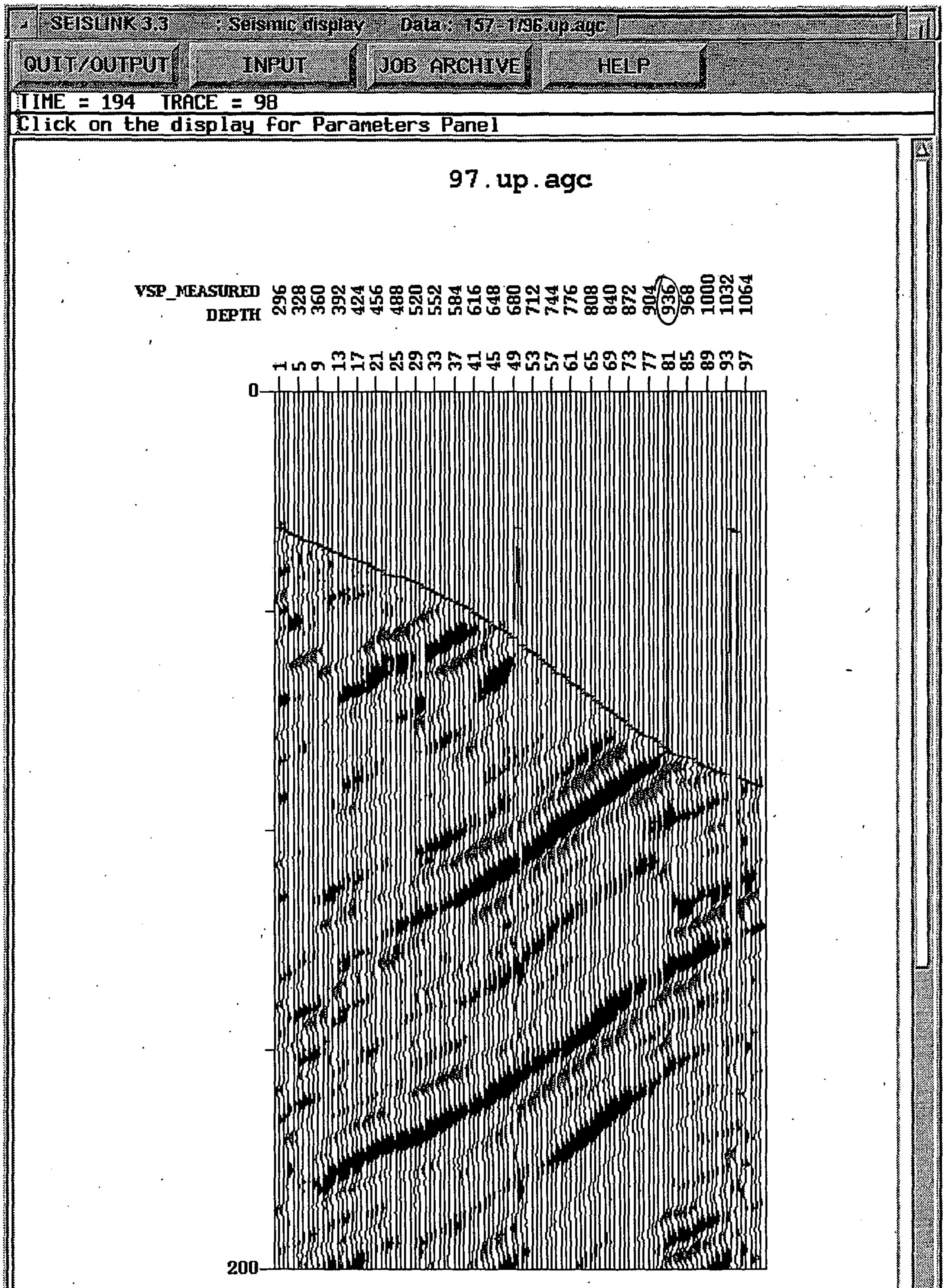

Figure D2b. Upgoing data from 1997 site 1 P-wave source after F-K filter.

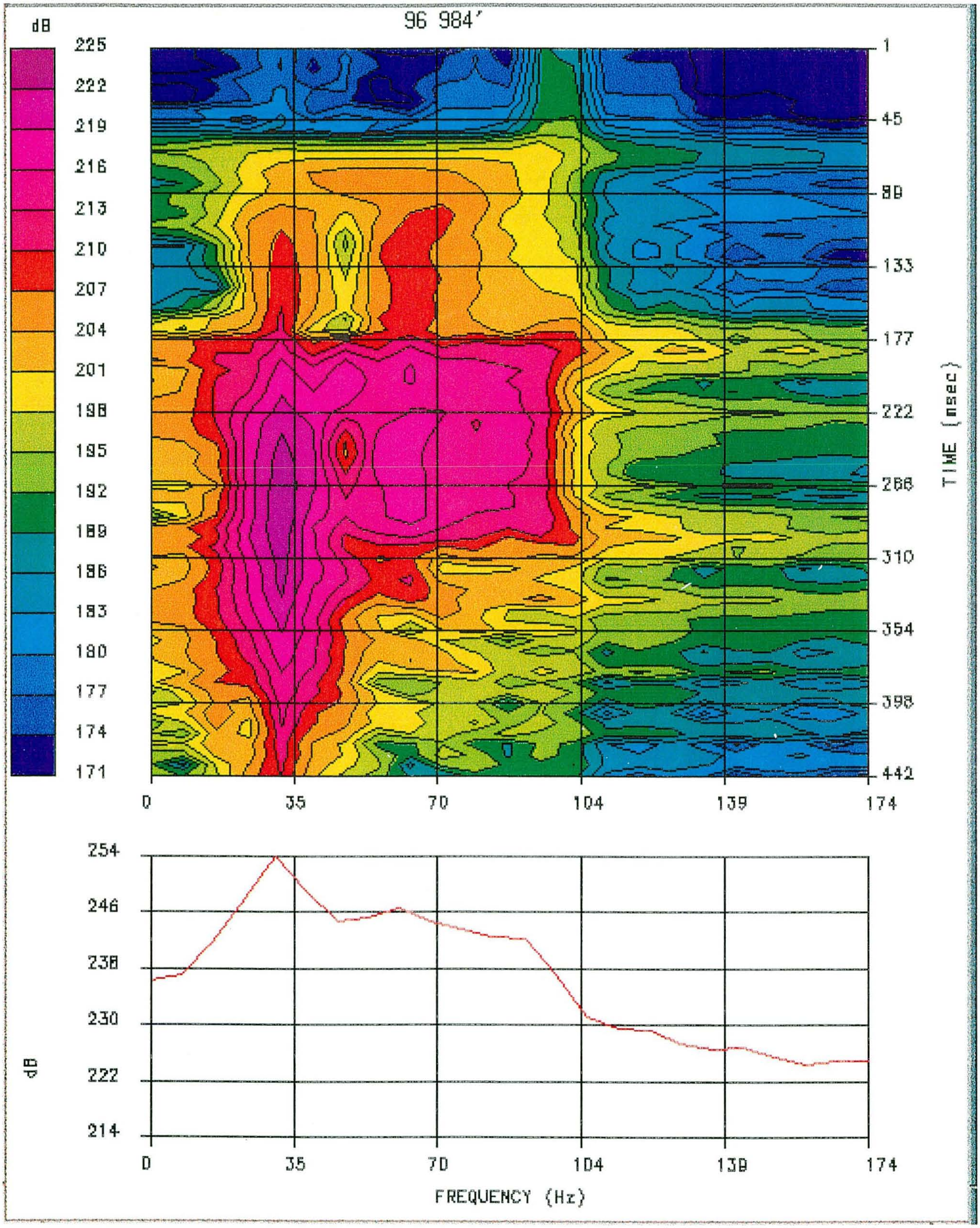

Figure D3a. Frequency vs time (top) and spectra (bottom) plot for average of two farthest 1996 walkaway P-wave sites for sensor at 984 ft.

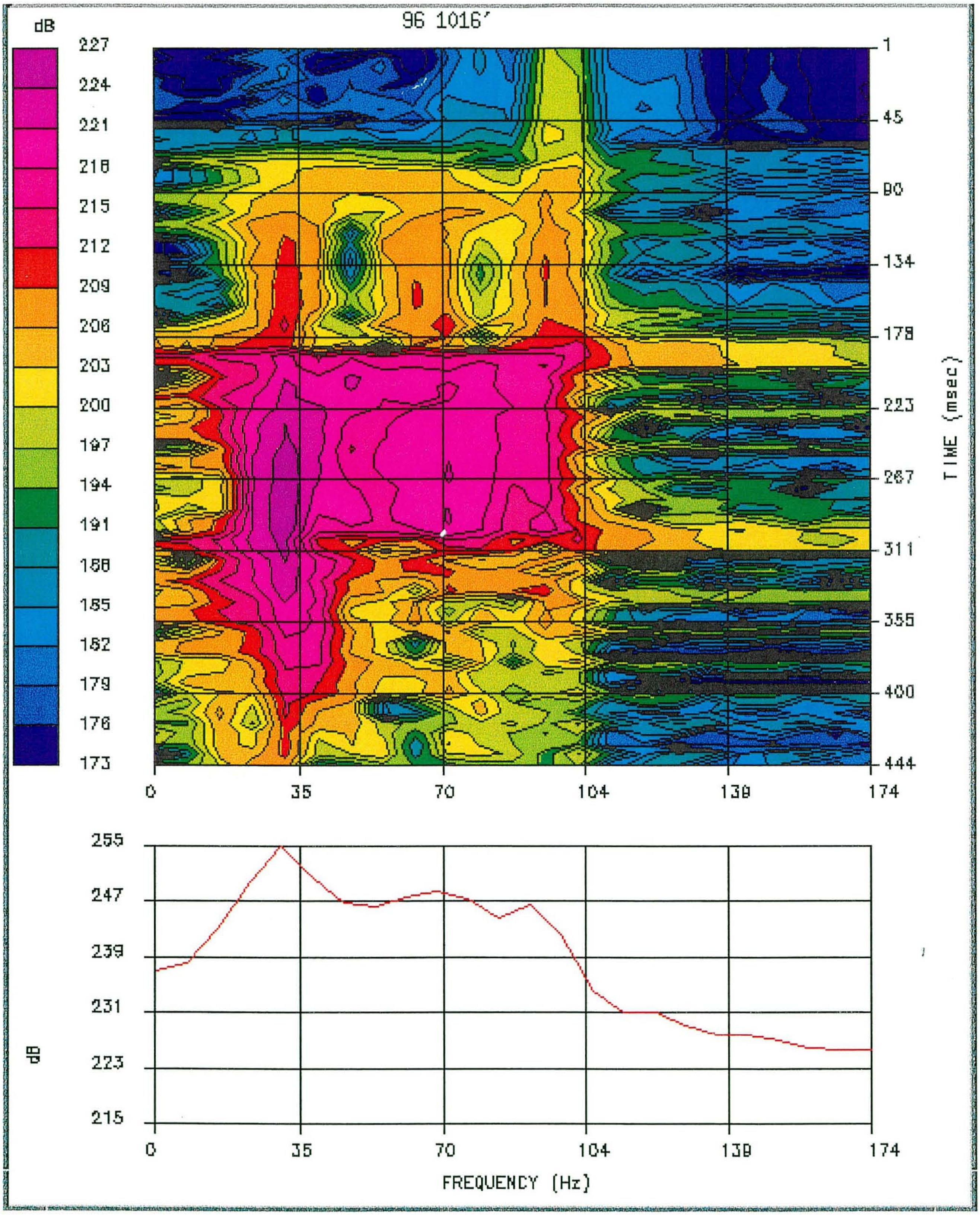

Figure D3b. Frequency vs time (top) and spectra (bottom) plot for average of two farthest 1996 walkaway P-wave sites for sensor at 1016 ft.

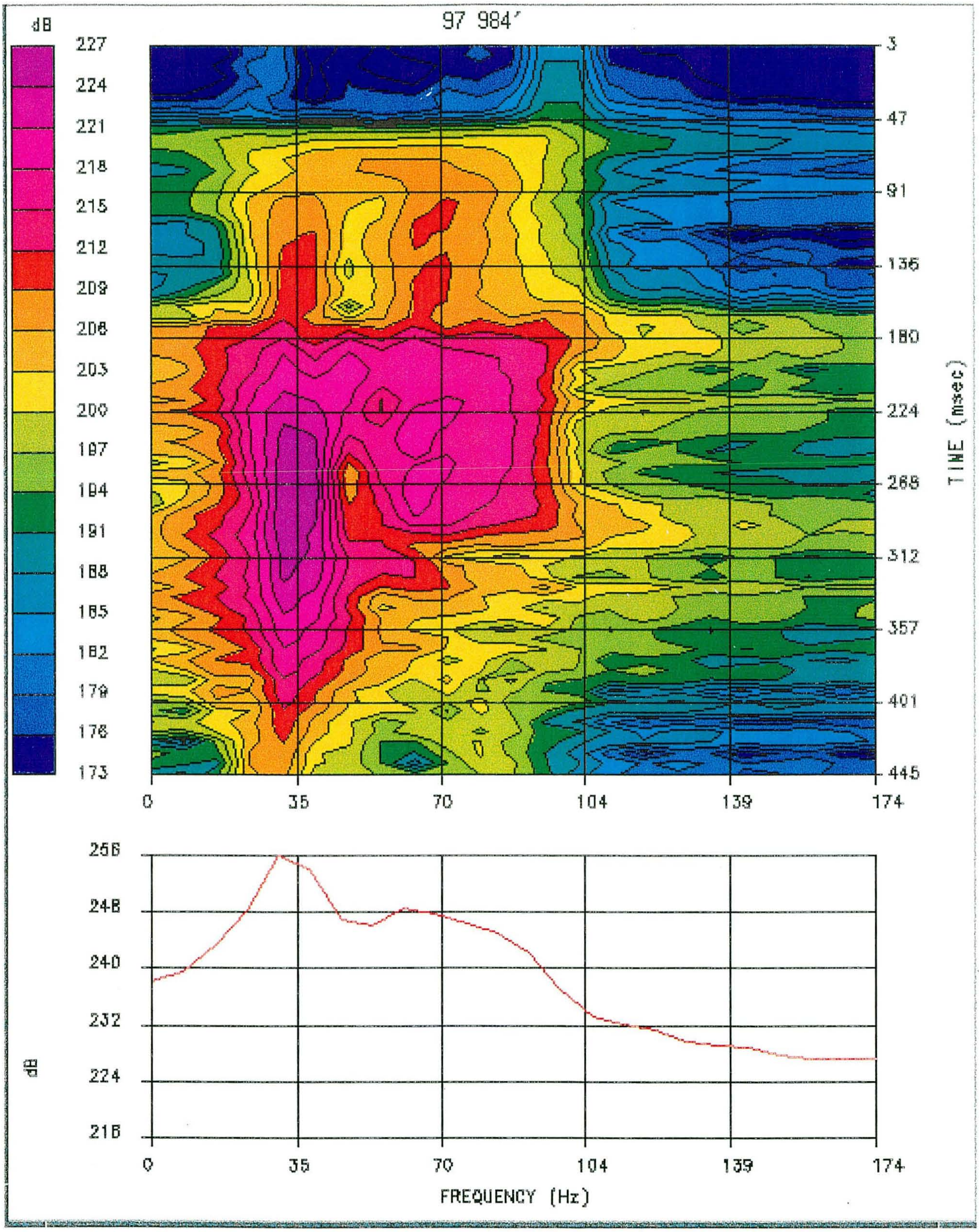

Figure D3c. Frequency vs time (top) and spectra (bottom) plot for average of two farthest 1997 walkaway P-wave sites for sensor at 984 ft.

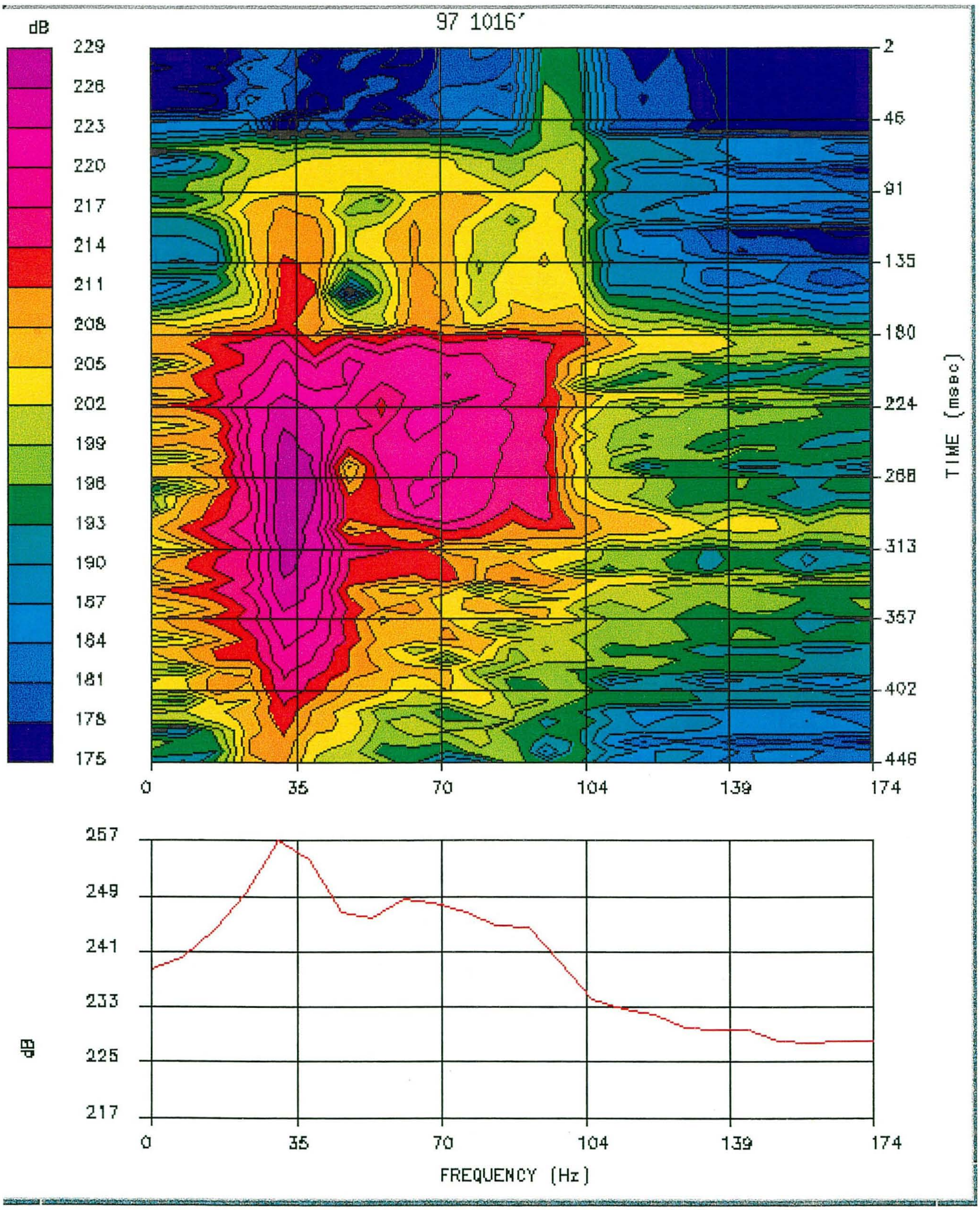

Figure D3d. Frequency vs time (top) and spectra (bottom) plot for average of two farthest 1997 walkaway P-wave sites for sensor at 1016 ft.

Appendix E - Surface Seismic Analysis

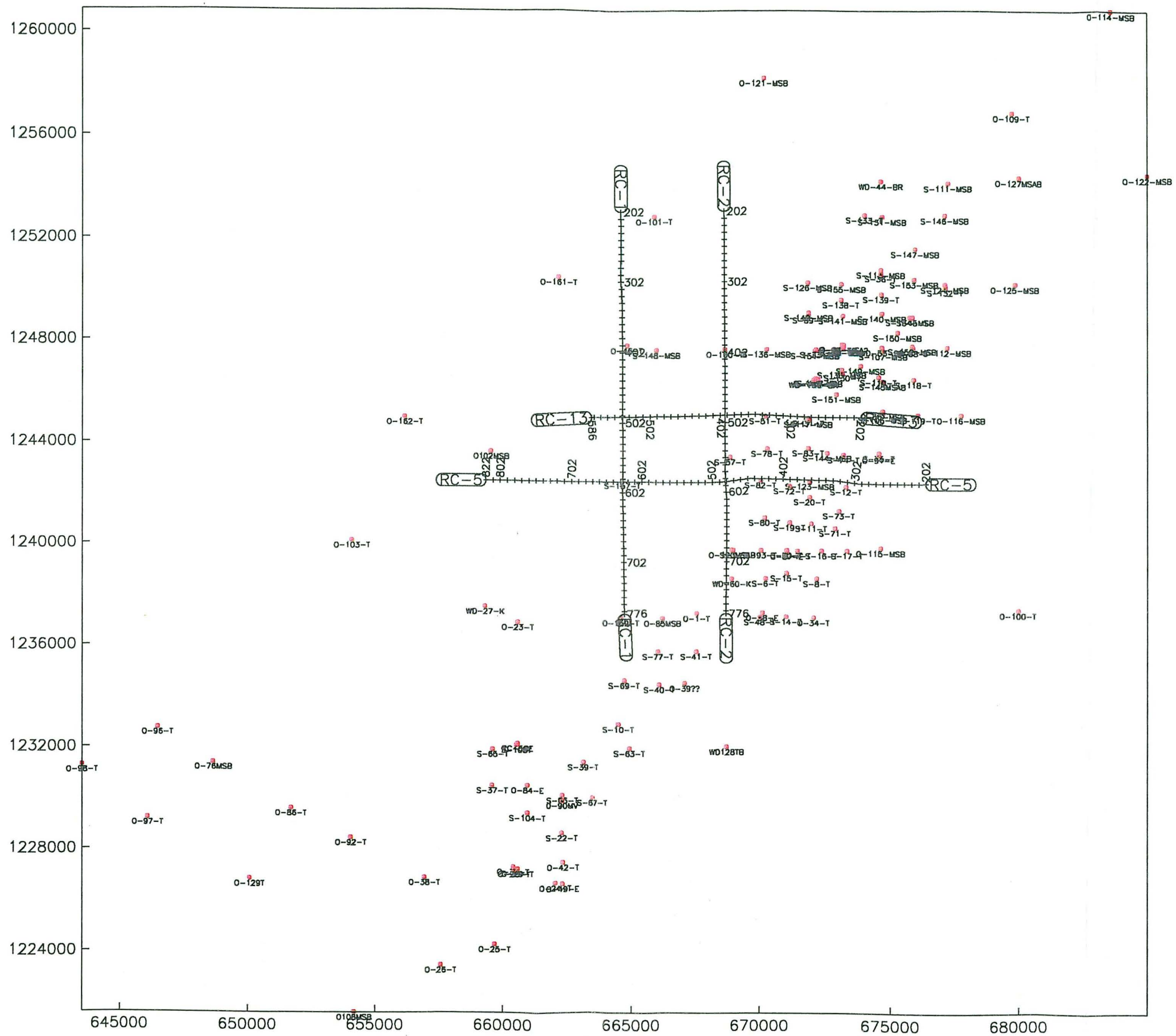
1260000
1256000
1252000
1248000
1244000
1240000
1236000
1232000
1228000
1224000
645000
650000
655000
660000
665000
670000
675000
680000
RC-1
RC-2
RC-13
RC-5
O-114-MSB
O-121-MSB
O-109-T
O-122-MSB
O-127MSAB
WD-44-BR
S-111-MSB
O-101-T
O-161-T
O-125-MSB
S-147-MSB
O-162-T
O-103-T
WD-27-K
O-23-T
O-100-T
O-95-T
O-76MSB
O-97-T
O-86-T
O-92-T
O-129T
O-38-T
O-25-T
O-26-T
S-69-T
S-10-T
S-63-T
S-39-T
S-104-T
S-22-T
O-42-T
WD128TB
S-77-T
S-41-T

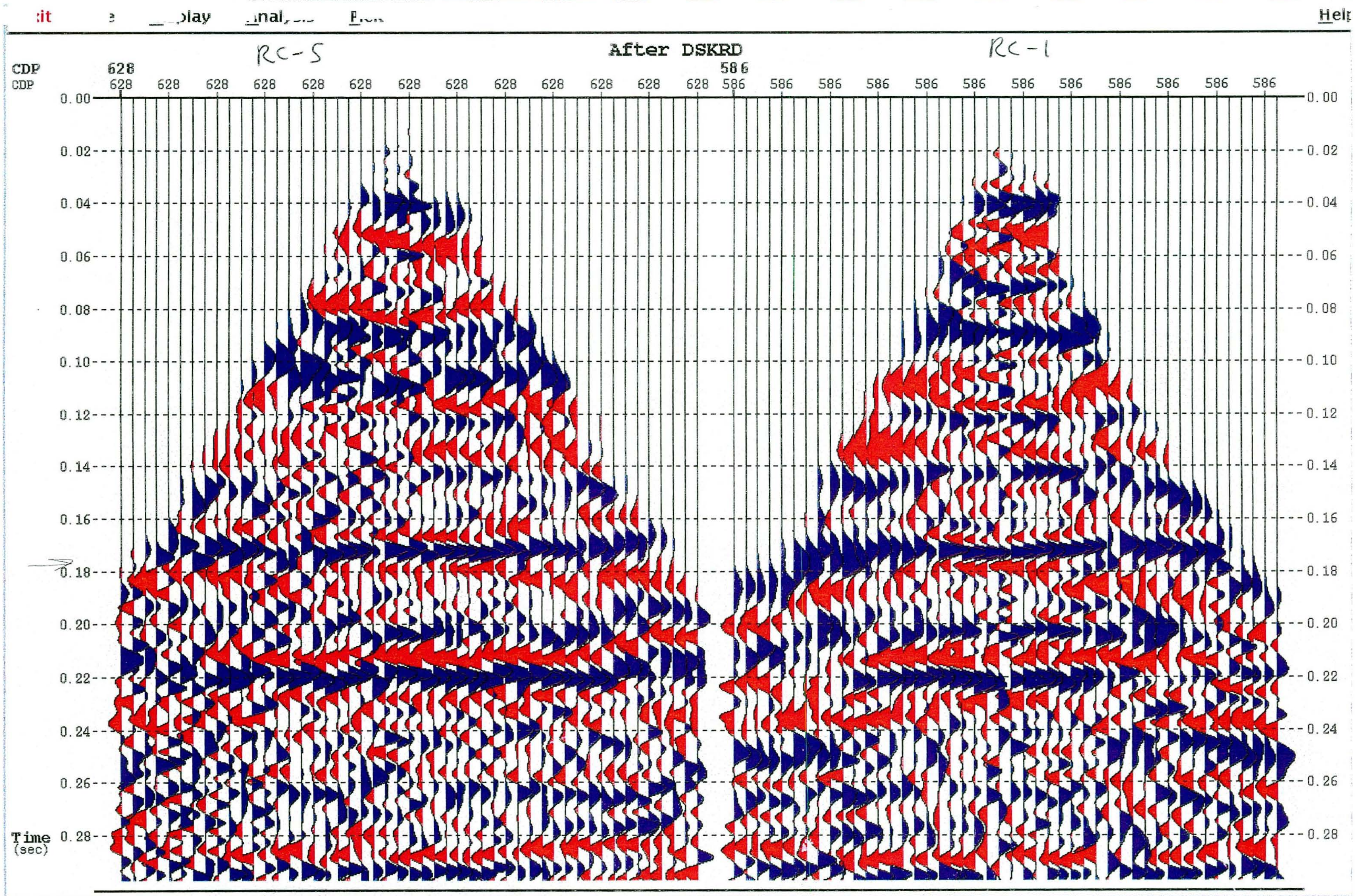

Figure E-2. Example CDP gathers from surface line RC-5 (left) and RC-1 (right) near the intersection of the lines. The reflector at about 0.17 s is the top of the Trenton reservoir formation.

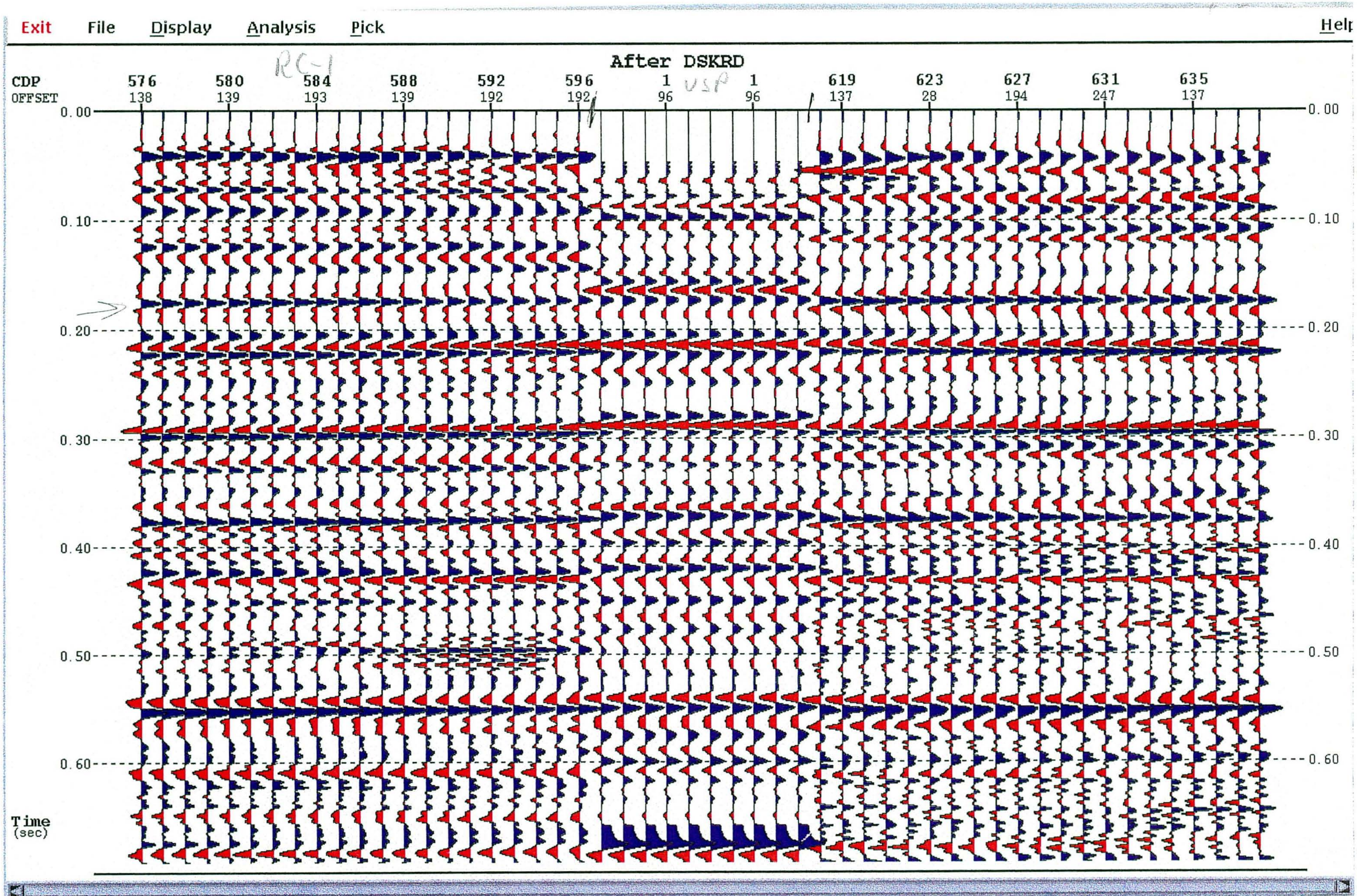

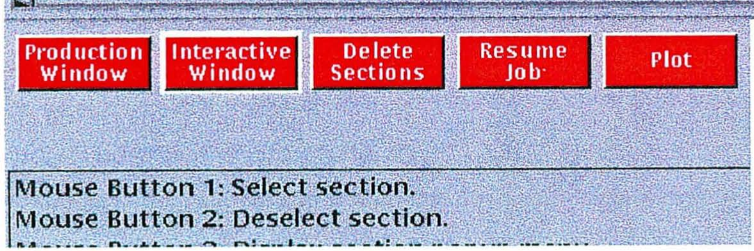

Figure E-3. CDP stacked sections for surface lines RC-1 (left, CDPs 576 - 596) and RD-5 (right, CDPs 618- 638) with the well 157 site 1 VSP P-wave upgoing stack displayed in the middle (labeled as CDP 1). The top of the Trenton reservoir formation is at about 0.18 s.

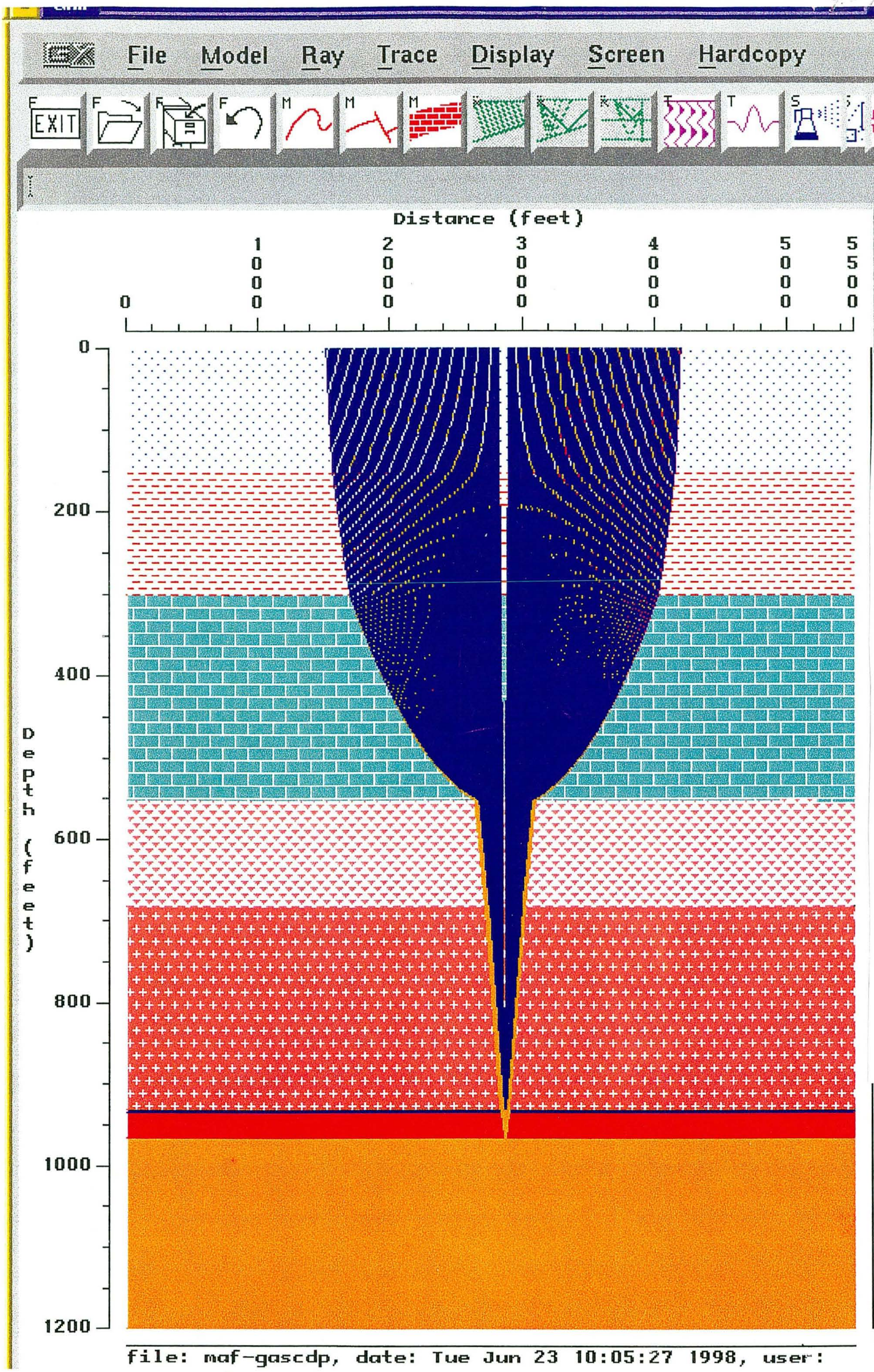

Figure E-4. Ray trace modeling of surface seismic CDP gather at Royal Center field using the velocity model derived from the well 157 VSP. The lack of variation in reflection angle of incidence at the Trenton reservoir formation (about 970 ft.) shows the limitations on any AVO analysis.

Prepared for the U.S. Department of Energy under Contract No. DE-AC03-76SF00098